© Copyright 2015
Hyun-Boo Lee

Study on dielectrophoretic behavior of a cell with sampling-based analysis for antimicrobial susceptibility test

Hyun-Boo Lee

A dissertation

submitted in partial fulfillment of the

requirements for the degree of

Doctor of Philosophy

University of Washington

2015

Reading Committee:

Jae-Hyun Chung, Chair

Nicholas Boechler

Kyong-Hoon Lee

Program Authorized to Offer Degree:

Mechanical Engineering

Nanotechnology

University of Washington

Abstract

Study on dielectrophoretic behavior of a cell with sampling-based analysis for antimicrobial susceptibility test

Hyun-Boo Lee

Chair of the Supervisory Committee:
Associate Professor Jae-Hyun Chung
Department of Mechanical Engineering

Antimicrobial susceptibility tests are used to evaluate antibiotics effectiveness for treating bacterial infection. These infections may contain drug resistant cells which can render certain antibiotics powerless. For effective patient treatment, a rapid, simple, and reliable susceptiblity test is critically needed. These susceptibility tests can be catagorized into either phenotypic or genotypic methods. Genotypic methods search for specific sequences known to cause the resistances. This method can be very rapid with high sensitivity and specificity, but requires skilled personnel and expensive equipment. Also, for many antibiotics, the genetic bases of resistance are highly complex or poorly understood. Phenotypic tests are based on detection of bacterial growth in the presence of antibiotics. Although very reliable and relatively cheap, standard methods require trained personnel and can be relatively slow, taking weeks for certain strains to culture for results. A rapid and simple method is needed to monitor the effective treatement of bacterial infections.

Dielectrophoresis (DEP) has been previsouly used to separate live and dead cells due to having different electric properties, and can be an approach to shorten and simplify the phenotypic method. DEP behavior of a cell is associated with the electric field-induced polarization of a cell. The cell polarization is dependent on cell characteristics such as size, shape and electrical properties, as well as enviromental parameters including electric field frequency, electrode geometry, and medium properties. Therefore, to differentiate cells according to viability, one must understand the complex relationship between cell polarization and cell property change. However, current DEP studies are insufficient to provide a comprehensive evaluation of the multiple cell characteristic parameters.

In this study, a novel sampling approach is presented to understand the DEP behavior of drug-treated cells. An algorithm using a sampling method is proposed to approximate diverse cell properties. With the algorithm, the cell properties are efficiently estimated from DEP experimental data. The estimation algorithm is evaluated in comparison to conventional approaches. The adavantages of the algorithm are shown by estimating various combinations of cell properties, which cannot be accomplished with conventional approaches.

A sensitivity analysis using a sampling method is conducted to investigate the relation between the electric field-induced polarization of a cell and the variation of cell properties. For the experimental parameters of applied frequency and medium conductivity, the sensitive properties determining cell polarization are specified. Through the analysis, 4 transition

condistions reversing cell polarization are found. By exploring the transition condition, the changes of each cell property are estimated.

Based on the estimation algorithm and the sensitivity analysis, dielectrophoretic behavior of *Mycobacterium bovis* bacillus Calmette-Guérin (BCG) cells is studied in response to heat-killing and drug treatment of rifampin (RIF) and isoniazid (INH). As a surrogate marker of *Mycobacterium tuberculosis*, the BCG cell is chosen for a drug-susceptibility test. The experimental parameters are designed on the basis of the sensitivity analysis. The medium conductivity (σ_m) and the frequency (f) for a crossover frequency (f_{xo1}) test are decided to detect the change of σ_m-f_{xo1} in conjunction with the drug mechanism. Statistical modeling is conducted to estimate the distributions of viable- and nonviable cells from the discrete measurement of f_{xo1}. Finally, the parameters of the electrophysiology of BCG cells, $C_{envelope}$ and σ_{cyto}, are extracted through the sampling algorithm. The estimated change of the electrophysiological parameters due to heat- and drug treatment is supported by the SEM images of BCG cells. The proposed experimental method and the corresponding algorithm can be beneficial for a drug-susceptibility test for tuberculosis.

By further developing the DEP characterization approach, the electrokinetic separation of viable and nonviable cells is studied. The cell behavior observed in an experiment is analyzed through a numerical simulation. In consideration of frequency-dependent DEP and AC electroosmosis (ACEO), the capturing and trapping behavior of cells are successfully analyzed. The optimal condition for separating viable- and nonviable BCG cells is found by understanding the electrokinetics of cells.

Table of Contents

List of Figures

Page

List of Tables

Page

Acknowledgements

I would like to express my sincere appreciation to my advisor Professor Jae-Hyun Chung for his advice, encouragement, and support in all stages of my research. I would like to also thank Dr. Kyong-Hoon Lee for his continuous support and advice. To my dissertation committee members, Professor Nicholas Boechler and Professor Nathan Sniadecki, I would like to thank for their suggestions and comments.

I would like to acknowledge the funding from Catalysis Foundation for Health, NSF Career Award (ECCS-0846454), and National Institute of Allergy and Infectious Disease (R01 AI093418).

Chapter 1: Introduction

This research investigates dielectrophoretic characterization of a cell to develop a rapid, simple, and reliable antimicrobial susceptibility testing method. In this chapter, current methods for antimicrobial susceptibility testing are introduced to understand their working mechanism to determine antimicrobial and drug resistances in a cell. Then, the potential of using dielectrophoresis for antimicrobial susceptibility testing is discussed through a literature review on dielectrophoretic separation of live- and dead cells. Lastly, the challenge of connecting the drug action mechanism and the change in dielectrophoretic behavior of a cell due to drug-treatment is discussed for application to antimicrobial susceptibility test.

1.1 Antimicrobial susceptibility test

Drug-resistant bacteria are serious threats to public health. According to CDC (Centers for Disease Control and Prevention) report in 2013, there are more than 2 million people infected and at least 23,000 people died from drug-resistant bacteria each year [1]. Treatment for drug-resistant bacterium requires an empirical therapy with various drugs, which is a painful process for patients. Antimicrobial susceptibility tests (AST) can reduce the treatment time needed to find working drugs to treat the infections.

AST are categorized into two approaches of genotypic- and phenotypic approaches [2, 3]. The genotypic approach is based on molecular detection, and is known as a reliable method for AST. Figure 1A shows the equipment used for testing drug-resistance in *mycobacterium tuberculosis* (MTB) [4]. The device can

detect the resistance gene to a specific drug called rifampin (RIF) in MTB by detecting gene mutation in the *rpoB* sequence. The detection can be done within 2 hours, which is a distinct advantage over the phenotypic approach which can take days. However, the limited detection of known drug resistances (i.e. gene sequences) is a big drawback of using the genotypic approach. In addition, the number of genetic sequences for drug resistance is always increasing, which is a huge burden in the genotypic approach.

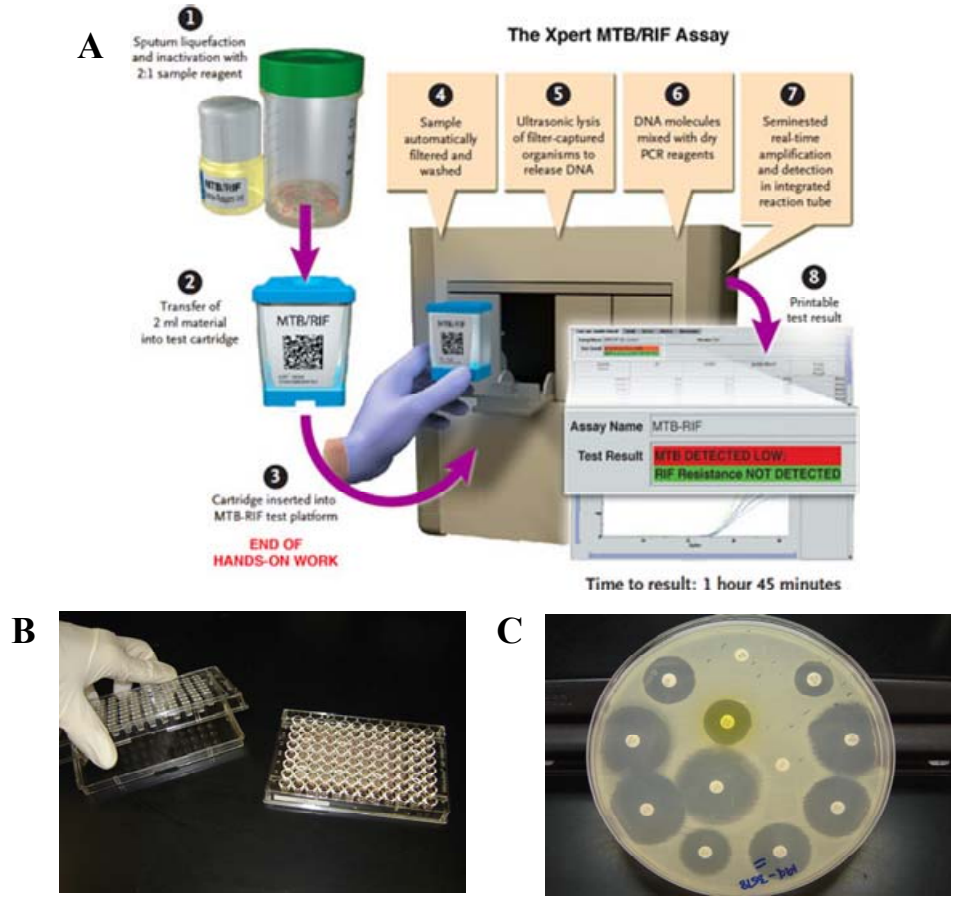

Figure 1 Approaches for an antimicrobial susceptibility test. A: Device based on genotypic method (GeneXpert). B: Broth dilution test. C: Disk diffusion test. Reproduced from [2].

The phenotypic approach is based on the detection of bacterial growth in the presence of antimicrobial drugs. Phenotypic approaches are capable of detecting the emergence of unknown resistances in a cell. Therefore, it is more widely used than the genotypic approach. There are several methods based on the phenotypic approach. Among them, the two methods frequently used, broth dilution- and disk diffusion tests, are introduced with working mechanisms.

Broth dilution test is one of the earliest AST methods (Fig. 1B) [2]. The process is to inoculate diluted antibiotics to bacterial suspension. After incubation of the sample, the turbidity of the suspension is examined to evaluate the bacterial growth. From broth dilution test, the minimum inhibitory concentration (MIC) is generated for quantitative evaluation.

Disk diffusion method uses the antimicrobial concentration gradient in an agar medium to determine the drug susceptibility of bacteria (Fig. 1C) [2, 3]. Bacteria cells with the concentration of $1\sim2\times10^8$ CFU/mL are prepared on the surface of agar plate. Subsequently, paper antibiotic disks are placed on the top of plate. After the incubation for 16-24 hours, the zones of growth inhibition around the disks are measured. The size of the inhibition zones depends on the diffusion rate of the antibiotic in the agar medium and the cell's susceptibility to the antibiotic [2, 5].

Both broth dilution- and disk diffusion methods are simple and cheap without need of special equipment. However, it is not appropriate to test slow growing bacteria such as MTB. Because the detection is based on the optical observation of bacterial growth, the testing time depends on the time required for cells to culture, which for slow growing bacteria, can take 6-12 weeks [6].

Therefore, an alternative method to evaluate some immediate change in bacteria from drug-treatment is needed to rapidly detect drug-susceptibility without waiting for cells to culture.

1.2 Dielectrophoresis (DEP)

Since Pohl discovered dielectrophoresis (DEP) in 1951 [7], DEP has been employed in various applications for micro/nano particle manipulation, enrichment, separation, and characterization.

With increasing demands for the development of high performance nanodevices, DEP-based fabrication has gained attention as an alternative approach to overcome the limitation of conventional top-down fabrication methods [8, 9]. Recently, the precise assembly and orientation of individual nanowires has been achieved with a deposition yield of 98.5% by using DEP combined with fluid flow (Fig. 2A) [10]. Figure 2B and 2C show the DEP assembly of latex particles and gold nanoparticles, respectively. A nanotube-based gas sensor has been developed with DEP concentraiton of carbon nanotubes (CNT) (Fig. 2D) [11].

DEP has also been employed to separate particles based on their sizes or electric properties. Figure 2E shows the separation of latex particles of different sizes by using DEP combined with electrohydrodynamic forces [12]. DEP separation of metalic- and semiconducting CNT has been conducted for the development of CNT-based transistors [13]. The electric characteristics of a nanowire has been investigated after the assembly with DEP [14].

.

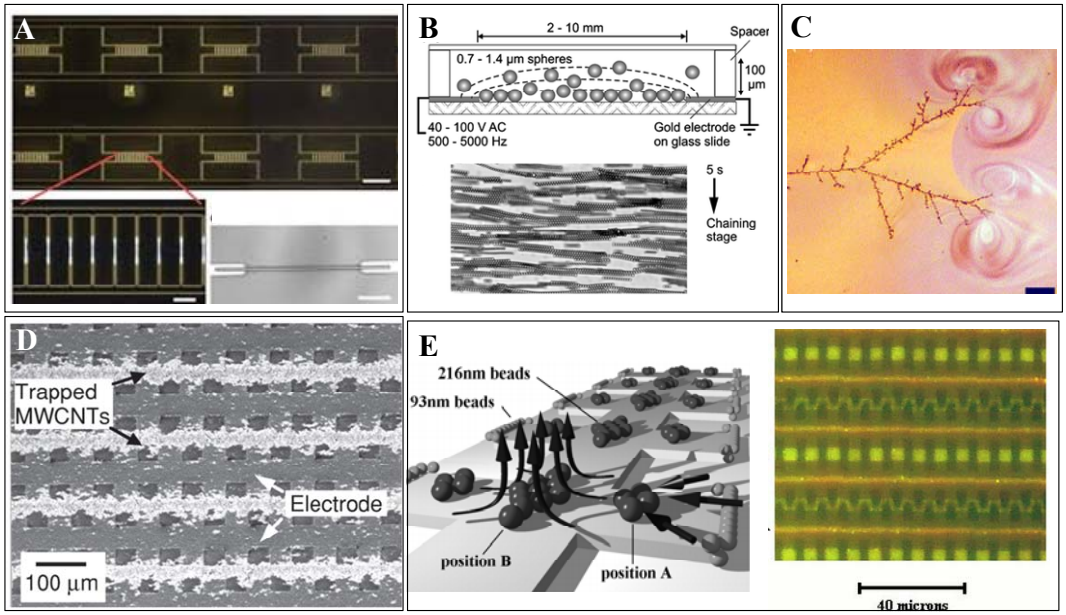

Figure 2 DEP applications for micro/nano particle manipulation. A: Nanowire assembly on finger-shaped electrodes. Reproduced from [10]. B: Chaining of latex spheres. Reproduced from [15]. C: Branch formation with gold nanoparticles. Reproduced from [15]. D: Enrichment of multi-walled carbon nanotubes (MWCNT). Reproduced from [11]. E: Separation of latex particles of different sizes. Reproduced from [12].

With the development of DEP techniques from nonbiological particles, DEP studies have been directed towards application for biological particles such as cells, viruses, DNA, and protein [16, 17]. For viruses, DNA, and protein, DEP studies are mainly conducted to develop biosensors for disease diagnosis [18, 19]. In the biosensor development, the investigation of effective concentration mechanisms using DEP is one of the main interests with the fuctionalization for capturing of specific targets [20, 21].

For a rapid AST, subtle variations in a cell resulting from drug-treatment should be detected. DEP has shown a potential for AST by separating cells having different electric properties [22-30]. DEP separation of two cells with the same dimensions can be acheieved by difference in the cell

polarization. Polarization factor (or Clausius-Mossotti factor), K_{CM}, tells the polarization of a cell in a medium. K_{CM} for a sphere model is defined as:

$$K_{CM} = \frac{\varepsilon^*_{cell} - \varepsilon^*_{medium}}{\varepsilon^*_{cell} + 2\varepsilon^*_{medium}} \tag{1.1}$$

$$\varepsilon^*_{cell} = \varepsilon^*_{mem} \frac{\left(\frac{r}{r - t_{mem}}\right)^3 + 2\left(\frac{\varepsilon^*_{cyto} - \varepsilon^*_{mem}}{\varepsilon^*_{cyto} + 2\varepsilon^*_{mem}}\right)}{\left(\frac{r}{r - t_{mem}}\right)^3 - \left(\frac{\varepsilon^*_{cyto} - \varepsilon^*_{mem}}{\varepsilon^*_{cyto} + 2\varepsilon^*_{mem}}\right)} \tag{1.2}$$

where ε^* is the complex permittivity ($\varepsilon^* = \varepsilon - i\sigma/\omega$), which is a combined property of the conductivity (σ) and the permittivity (ε). ω is the angular frequency of an applied electric field ($\omega = 2\pi f$). The cell is assumed to be composed of two compartments, the membrane (mem) and the cytoplasm (cyto) [31]. r and t_{mem} are the cell radius and the membrane thickness, respectively.

As shown in equations (1.1) and (1.2), cell polarization changes with changes in the frequency (f) of the applied electric field and the medium properties (σ_{medium} and ε_{medium}). By using the frequency spectra of K_{CM} at several medium conditions, separation of two cells having different electric properties can be obtained due to the differences in K_{CM}. In the following sections, DEP characterization approaches are introduced followed by DEP studies for two cell groups of eukaryotic cells (e.g. mammalian, yeast) and prokaryotic cells (e.g. bacteria).

1.3 DEP characterization of cell

For DEP characterization, two methods are used. One is the cell counting method which counts the number of cells attracted on electrodes at various frequencies [26, 32, 33]. This method assumes that the number of cells captured on electrodes is proportional to K_{CM} of the cell. However, the cell counting method can be confounded by electrohydrodynamic effects. In addition, a negative DEP repelling a cell from electrodes may not be considered for a counting method, a major drawback for estimation of cell properties.

The other method uses a crossover frequency (f_{xo}) to detect the frequency at which attraction of a cell switches to repulsion or vice versa [18, 34]. At f_{xo}, the sign of K_{CM} is reversed between negative and positive, meaning that the polarizability of the cell matches that of the surrounding medium. Upon known electric properties of the medium, the electric properties of the target cell can be extracted from f_{xo} with a cell model. The property dependency of f_{xo} varies with the change of σ_{medium}. Therefore, σ_{medium} and the corresponding frequency (f) need to be estimated for the DEP characterization of a cell. In other words, specific DEP experimental conditions of σ_m and f are required to detect a property change in a cell.

1.4 DEP study for cell

1.4.1 DEP for eukaryotic cells

Eukaryotic cells are commonly used in DEP experiments due to their relatively large dimesion among biological particles. For larger particles, DEP force with the proportionality to r^3 (r: particle radius) can be more dominant than other forces such as Brownian- ($F_B \sim r^{0.5}$) and electrohydrodynamic forces ($F_{EHD} \sim r$) [35]. Therfore, the change in DEP behavior of eukaryotic cells is more noticeable than other biological particles. Also, DEP behavior of a single eukaryotic cell can be observed by conventional optical systems without labeling for the amplication of a signal.

Among eukaryotic cells, red blood- [36-38], leukemia- [24-27, 36], breast cancer- [23, 39], and yeast cells [30, 37, 40, 41] have been of great attention in DEP study. Figure 3 shows some examples of DEP separation for leukemia-, breast cancer-, and yeast cells. Shafiee et al. isoltated live leukemia cells from dead leukemia cells using contactless dielectrophoresis (Fig. 3A) [27]. Sun et al. has characterized DC dielectrophoreic separation of breast cancer cells from bone marrow cells (Fig. 3B) [39]. Figure 3C shows the separation- and the concentration of live- and dead yeast cells [30].

With a relatively thin membrane layer compared to their size, eukaryotic cells have shown their suitablity for DEP study. It was proven that the change in cell's surface morphology, membrane barrier functions, and intercellular reactions can be detected from monitoring the DEP behavioral change, which is affected due to the alterations of the specific capacentance-

and conductance of the cell's membrane [17, 18]. Therefore, the viability or abnormality of eukaryotic cells caused by drug-treatments can be evaluated through DEP experiments.

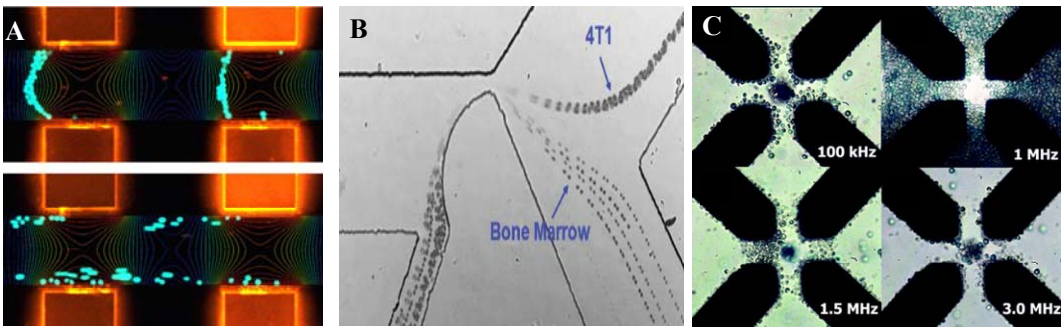

Figure 3 DEP separation of cells. A: selective capture of live human leukemia cells. Reproduced from [27]. B: DC dielectrophoretic separation of breast cancer cells from bone marrow cells. Reproduced from [39]. C: Frequency dependent separation of viable and nonviable yeast cells. Reproduced from [30].

1.4.2 DEP for prokaryotic cells

Bacteria are the most common types of prokaryotic cells. *Escherichia coli* (*E.coli*), *Staphylococcus epidermidis* (*S.epi*), *Staphylococcus aureus* (*S.aureus*), *Bacillus subtilis* (*B.subtilis*), and *Listeria* are bacteria that have been routinly chosen for DEP experiments [17].

Castellarnau et al. has characterized wild type- and mutant *E.coli* by using the crossover frequency method [34]. Crossover frequencies were measured in the restricted range of σ_{medium} from 10^{-3} S/m to 0.13 S/m. The upper limit of σ_{medium} was determined due to low DEP force in high conductivity media. The difference in dielectric properties between the wild type- and the mutant *E.coli* was estimated from the crossover frequency measurment. Due to multiple cell parameters, the estimation was conducted through a least square approximation by fixing some parameters. The fixed parameters were chosen based on a sensitivity analysis. Therefore, the change in the *E.coli* mutant was represented with change of the nonfixed parameters.

Joari et al. has used DEP to determine the antibiotic resistance of *S.epi* [42]. The K_{CM} spectra of antibiotic-sensitive and antibiotic-resistant strains of *S.epi* were compared based on the cell counting method. In the experiment, a low σ_{medium} of 10^{-3} S/m was used to reduce the electrohydrodynamic interference. The significant difference in dielectric properties was estimated for the sensitive strain before and 24 hours after the treatment of antibiotic streptomycin. The dielectric properties of the *S.epi* was determined by fitting the K_{CM} spectra to the number of bateria collected. The fitting was performed by visual inspection and reported parameters in the literature.

Chung et al. has shown DEP-based AST with *E.coli* and determined the minimum inhibitory concentration of drugs [22]. The crossover frequencies for wildtype- and cephalosporin-resistant *E.coli* were measured by varying the antibiotic dose. The drug-resistant *E.coli* was discriminated with the change in crossover frequency and the length of bacteria. The DEP-based discrimination was possible at the antibiotic dose of 1 μg/mL after 120 minutes of incubation. With the increase of antibiotic dose to 2 μg/mL, the detection time decreased to 90 minutes. The DEP-based AST was validated by comparison with the broth dilution test.

Most bacteria cells are much smaller than eukaryotic cells. The smaller dimensions of bacteria cells leads to less DEP studies due to a small DEP force; interpretation of DEP behavior is challenging with the interference of electrohydrodynamic effects and Brownian motion [43-51]. Also, the high surface-to-volume ratio of prokaryotic cells makes it difficult to distigusigh the changes in the cell envelope and cytoplasm in low conductive media. With the challenges caused by the small size of bacteria as well as a difficulty in growing *Mycobacterium Tuberculosis* (MTB) complex cells, DEP study for MTB cells has not been conducted.

1.5 Challenges of DEP for AST

There are three main challenges to using DEP for AST. The first challenge is the lack of a standard to determine the drug susceptibility of a cell in terms of DEP parameters. DEP-based AST assumes that the cell viability is connected to the cell property change, which is detectable by observing DEP behavior of a cell. However, there are no guidelines to determine the death of a cell with corresponding change of cell properties. To employ DEP for AST, understanding of the relation between the cell viability and the change of cell properties is required.

Second is the challenge in handling bacteria for DEP experiment. Compared to eukaryotic cells, the change of DEP behavior for bacterial cells are less detectable due to the small dimension of bacterial cells. To improve the detection of DEP behavior of bacterial cells with the change of their cell properties, the DEP experimental conditions should be carefully designed.

The third challenge is the DEP characterization of drug effect due to limited data obtained from DEP experiments. Due to the limited data, the estimation of cell property relies on the characteristics of an approximation approach. Current approximation approaches are based on fitting experimental data with a best-fitting line. Therefore, estimation is limited to only one possible set of cell properties while various sets can exist. To consider all possibilities, a multi-dimensional analysis is required but the increase of computational cost with the increase of number of parameters is a big obstacle.

1.6 Objectives

The main objective of this dissertation is to study the DEP characterization of a cell for an antimicrobial susceptibility test. A sampling-based approach is newly proposed to address the three challenges of DEP for AST.

With the proposed approach, the change of a polarization factor representing DEP behavior of cell is investigated with various combinations of cell property. Effective DEP parameters dominating the polarization of cell are specified through a sensitivity analysis. Using the effective parameters, DEP experimental condition for *Mycobacterium tuberculosis* complex cell is designed. The properties of drug-treated cell are estimated with a sampling-based algorithm. Then, the relationship between the drug mechanism and the change of DEP behavior of cell is investigated. By further developing the DEP characterization approach, the electrokinetic separation of viable- and nonviable cells is studied in consideration of DEP with AC electroosmosis. To this end, a novel sampling-based approach is proposed to potentially use DEP for drug susceptibility testing by in-depth understanding about DEP-induced cell behavior. The whole research results are illustrated by a flow chart in Fig. 4.

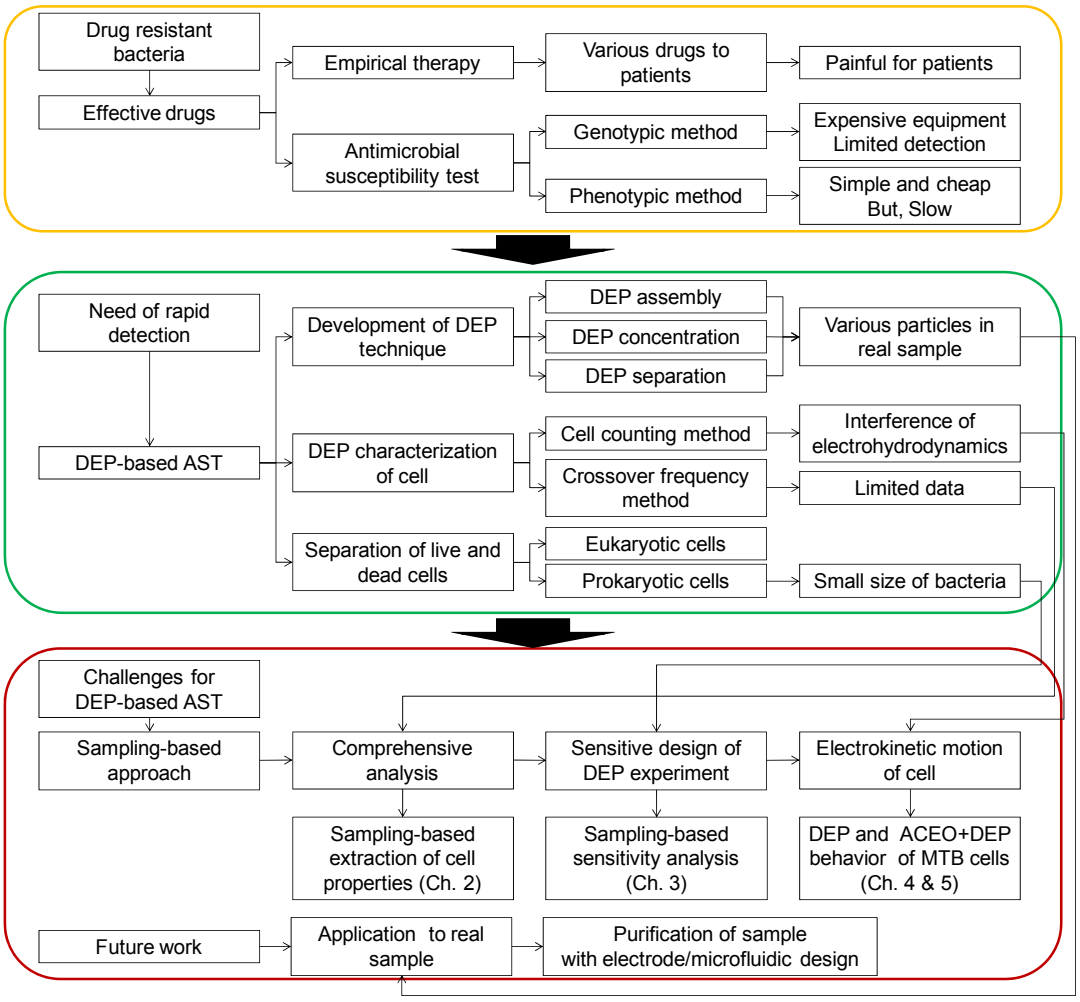

Figure 4 Diagram of logic development for the need of a rapid AST method (yellow), the challenges in DEP-based AST (green), and the research objectives of the dissertation (red).

Chapter 2: Sampling-based extraction of cell properties from DEP transition conditions

2.1 Background

The electric field-induced dipole moment in a particle has been measured to characterize the properties of the particle. The induced dipole moment on a particle generates a force on the particle under a non-uniform electric field. Motion of the particle due to the force is dielectrophoresis (DEP). Depending on the eletric properties and the geometry of particle, DEP force is determined once the parameters for a medium and a frequency (f) are given. Using the property dependency on DEP, the frequency response of DEP for a single- or multiple medum conditions has been studied to characterize micro- and nanoscale particles including biological particles such as cells [17, 25, 26, 52-56].

To extract the properties of a cell, the crossover frequency reversing the polarity of DEP between positive (pDEP) and negative (nDEP) is investigated. The sign of DEP on a cell is determined by the relative polarizability between a cell and a medium. The relative polarizability is a function of the electric properties of cell and medium and the frequency. At the crossover frequency, the polarizability of cell and medium becomes the same. By using the known medium properties, the cell properties can be estimated at the crossover frequency. Depending on the medium condtion, 0~2 crossover frequencies can exist. When 2 crossover frequencies are present, the first- and the second crossover frequencies are f_{xo1} and f_{xo2}, respectively. For estimation of cell

properties, the medium showing f_{xo1} and f_{xo2} has been used [18, 34].

There are two main challenges to use crossover frequencies for cell characterization. One is the non-linearity of f_{xo1} on the cell properties. In a proper range of medium conductivity (σ_m), a linear relationship between σ_m and f_{xo1} is shown, and the slope and the intercept of the line is determined by the membrane properties of a cell (σ_{mem} and ε_{mem}). In the low frequency approximation [57], the linear relationship is used to characterize the cell membrane properties. However, when σ_m is not properly chosen, the linearity is not obtained, which increases an error. To overcome the non-linearity, the 5-level approximation has been suggested by Lei et al. [58]. The approximation still has a limitation in that a specific range of f and σ_m and a specific geometry of a cell should be identified. In addition, the estimation of cytoplasm properties using f_{xo2} shows a dependency on both the conductivity and the permitivity of cytoplasm (σ_{cyto} and ε_{cyto}). The potential problem is that the two properties of σ_{cyto} and ε_{cyto} are estimated from one parameter of f_{xo2} due to the small variation of f_{xo2} in the wide range of σ_m.

In this study, we present a sampling-based method to extract cell properties from the σ_m-f_{xo1} line obtained from the reference [57]. In section 2.2, current theories, the low frequency- and the 5-level approximation, for the extraction of cell properties from f_{xo1} are reviewed. In section 2.3, a sampling-based estimation is introduced. The validation analysis is conducted in comparison with the low frequency- and the 5-level approximation for the property estimation in section 2.4.

2.2 Theory

The properties of a cell are estimated by using the relationship between f_{xo} and the cell properties. f_{xo} is derived in terms of cell properties from the Clausius-Mossotti factor, K_{CM}, which explains the polarizability of a particle in a medium. K_{CM} is defined as:

$$K_{CM} = \frac{\varepsilon_p^* - \varepsilon_m^*}{\varepsilon_p^* + 2\varepsilon_m^*} \tag{2.1}$$

where ε^* is the complex permittivity ($\varepsilon^*=\varepsilon-i\sigma/\omega$), which is a combined property of the conductivity (σ) and the permittivity (ε). ω is the angular frequency of an applied electric field ($\omega=2\pi f$).The property of particle and medium is indicated with the subscript of p and m, respectively.

For a cell consisting of the membrane and the cytoplasm (interior material), the complex permittivity of particle is represented as the effective complex permittivity [31]:

$$\varepsilon_{p\_eff}^* = \varepsilon_{mem}^* \frac{\left(\frac{r}{r - t_{mem}}\right)^3 + 2\left(\frac{\varepsilon_{cyto}^* - \varepsilon_{mem}^*}{\varepsilon_{cyto}^* + 2\varepsilon_{mem}^*}\right)}{\left(\frac{r}{r - t_{mem}}\right)^3 - \left(\frac{\varepsilon_{cyto}^* - \varepsilon_{mem}^*}{\varepsilon_{cyto}^* + 2\varepsilon_{mem}^*}\right)} \tag{2.2}$$

where r and t_{mem} are the cell radius and the membrane thickness, respectively. The cytoplasm and the membrane are denoted by cyto and mem, respectively.

The relationship between f_{xo} and cell properties can be derived by solving the equation of real[K_{CM} (ω)] = 0, then $\omega=2\pi f_{xo}$. However, the equation is nonlinear, which may not be solved. To address the challenge, the approximation equation of f_{xo} is derived from the Maxwell-Wagner interfacial polarization constant (τ_{MW}) under the low frequency assumption [57]:

$$f_{\mathrm{xo}} = f_{\mathrm{xo1}} = \frac{\sqrt{2}t_{\mathrm{mem}}}{2\pi R\varepsilon_{\mathrm{mem}}}\sigma_{\mathrm{m}} - \frac{\sqrt{2}\sigma_{\mathrm{mem}}}{8\pi\varepsilon_{\mathrm{mem}}} \tag{2.3}$$

Because the low frequency assumption is used, f_{xo} in Eq. (2.3) is the 1st crossover frequency (f_{xo1}). Equation (2.3) explains the relation between the membrane properties (σ_{mem} and $\varepsilon_{\mathrm{mem}}$) and f_{xo1}. The linear dependency of f_{xo1} on σ_{m} is shown such that the σ_{m}-f_{xo} line can be expressed in terms of the slope and the intercept of the line. Both $\varepsilon_{\mathrm{mem}}$ and σ_{mem} are extracted from the slope and the intercept, respectively. However, the approximation is valid only in the limited range of σ_{m} and f. Also, the cytoplasm properties cannot be estimated with the equation.

Lei et al. studied the validity of the low frequency approximation with 5-levels of approximation by considering scaling parameters of cell properties with σ_{m} and f [58]. The effective complex property of a cell in Eq. (2.2) is divided into the effective conductivity ($\sigma_{\mathrm{p\_eff}}$) and the effective permittivity ($\varepsilon_{\mathrm{p\_eff}}$) with the condition of $t_{\mathrm{mem}} << r$:

$$\sigma_{\mathrm{p\_eff}} = \frac{-\left(\varepsilon_{\mathrm{mem}}\varepsilon_{\mathrm{cyto}} - \sigma_{\mathrm{mem}}\sigma_{\mathrm{cyto}}\right)\left(\sigma_{\mathrm{mem}} + \frac{t_{\mathrm{mem}}}{r}\sigma_{\mathrm{cyto}}\right) + \left(\sigma_{\mathrm{mem}}\varepsilon_{\mathrm{cyto}} + \varepsilon_{\mathrm{mem}}\sigma_{\mathrm{cyto}}\right)\left(\varepsilon_{\mathrm{mem}} + \frac{t_{\mathrm{mem}}}{r}\varepsilon_{\mathrm{cyto}}\right)}{\left(\varepsilon_{\mathrm{mem}} + \frac{t_{\mathrm{mem}}}{r}\varepsilon_{\mathrm{cyto}}\right)^2 + \frac{1}{\omega^2}\left(\sigma_{\mathrm{mem}} + \frac{t_{\mathrm{mem}}}{r}\sigma_{\mathrm{cyto}}\right)^2} \tag{2.4}$$

$$\varepsilon_{\mathrm{p\_eff}} = \frac{\left(\varepsilon_{\mathrm{mem}}\varepsilon_{\mathrm{cyto}} - \sigma_{\mathrm{mem}}\sigma_{\mathrm{cyto}}\right)\left(\varepsilon_{\mathrm{mem}} + \frac{t_{\mathrm{mem}}}{r}\varepsilon_{\mathrm{cyto}}\right) + \frac{1}{\omega^2}\left(\sigma_{\mathrm{mem}}\varepsilon_{\mathrm{cyto}} + \varepsilon_{\mathrm{mem}}\sigma_{\mathrm{cyto}}\right)\left(\sigma_{\mathrm{mem}} + \frac{t_{\mathrm{mem}}}{r}\sigma_{\mathrm{cyto}}\right)}{\left(\varepsilon_{\mathrm{mem}} + \frac{t_{\mathrm{mem}}}{r}\varepsilon_{\mathrm{cyto}}\right)^2 + \frac{1}{\omega^2}\left(\sigma_{\mathrm{mem}} + \frac{t_{\mathrm{mem}}}{r}\sigma_{\mathrm{cyto}}\right)^2} \tag{2.5}$$

Equations (2.4) and (2.5) are used for the level 5 approximation. For the level 4 approximation, equations (2.4) and (2.5) are simplified with the following restrictions on cell properties:

$$\varepsilon_{\mathrm{mem}} \approx 10\varepsilon_0,\ \sigma_{\mathrm{mem}} \approx 10^{-6}\ \mathrm{S/m},\ \varepsilon_{\mathrm{cyto}} \approx 100\varepsilon_0,\ \text{and}\ \sigma_{\mathrm{cyto}} \approx 1\ \mathrm{S/m} \tag{2.6}$$

where ε_0 is the permittivity of vacuum (8.8542×10^{-12} F/m).

$$\sigma_{\text{p\_eff}} = \frac{\varepsilon_{\text{mem}}^2 \sigma_{\text{cyto}} + \frac{\sigma_{\text{mem}} \sigma_{\text{cyto}}^2}{\omega^2} \frac{t_{\text{mem}}}{r}}{\varepsilon_{\text{mem}}^2 + \frac{\sigma_{\text{cyto}}^2}{\omega^2} \left(\frac{t_{\text{mem}}}{r} \right)^2} \tag{2.7}$$

$$\varepsilon_{\text{p\_eff}} = \frac{\varepsilon_{\text{mem}}^2 \varepsilon_{\text{cyto}} + \frac{\varepsilon_{\text{mem}} \sigma_{\text{cyto}}^2}{\omega^2} \frac{t_{\text{mem}}}{r}}{\varepsilon_{\text{mem}}^2 + \frac{\sigma_{\text{cyto}}^2}{\omega^2} \left(\frac{t_{\text{mem}}}{r} \right)^2} \tag{2.8}$$

For the 1-3 level of approximation, equations (2.7) and (2.8) are further reduced with the limited applicable ranges of σ_{m} and f. The accuracy of approximation was improved and the extraction of σ_{cyto} was obtained, which was not possible in the low frequency approximation.

In the approximation approach, an optimization-based method was employed to solve the problem having more unknowns than the number of equations. The approach can give the best values matched with actual cell properties because the optimization is based on the minimization of the error between the estimation and experiment. However, the approximation can be a local minimum due to the presence of multiple solutions. In addition, the approximation is limited due to the geometrical restriction on the cell model (e.g. shape, size, membrane thickness).

2.3 Sampling-based approximation

In this study, the sampling-based approximation is developed to extract all the possible combinations of cell properties from DEP experimental data regardless of the cell geometry. In experiment, the measurement data of σ_m-f_{xo} could show a variation because of the differences on the size- or the electrophysiological state of a cell in a batch of target cells. Therefore, the estimation of a target cell property with one optimal value using a conventional approach might lack information to represent a group of target cells. The sampling-based estimation proposed in this study can consider the variation of the measurement data. As a result, the distribution of cell properties can be extracted.

Figure 5 shows the procedure for the sampling-based approximation. Firstly, the measurement data of σ_m-f_{xo} for a target cell is provided with a variation. According to the cell type, the cell model is determined as the single-shell sphere or the double-shell ellipsoid. Before sampling, the ranges for cell properties are assigned with a cell dimension (e.g. r, t_{mem}). Sampling is conducted to generate a random set of properties for a cell. For the sampled cell, K_{CM} at the condition across the variation range of the measured σ_m-f_{xo} is computed. By checking if the sign reversal happens across the variation range, the properties of the sampled cell are extracted. The steps from the sampling to the extraction are repeated until the number of cells is enough to see a clear distribution of cell properties (e.g. 1,000 cells). If the number of cells sampled is small, the estimated properties could be case-sensitive without reliability. To generate a sufficient quantity of cells, the sampling was repeated until 1,000 cells of the properties were generated. It was found that 1,000 sampled cells were enough to represent the property of a cell. To

improve the computation efficiency, a random sampling method was used in the algorithm.

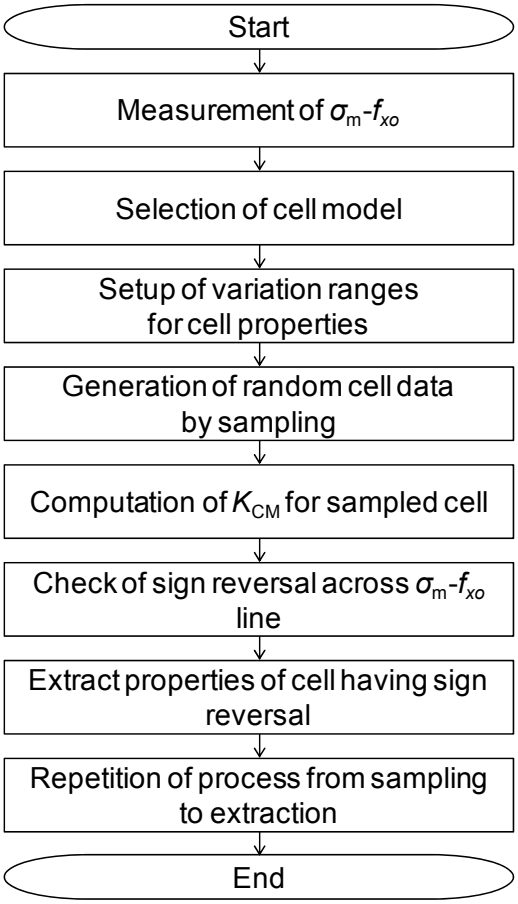

Figure 5 Procedure for the sampling-based approximation of cell properties.

2.4 Validation of approach

For validation of the sampling-based approximation, the estimated values of cell properties from the sampling-based approximation were compared with those from the low frequency approximation [57] and the 5-level approximation by Lei et al. [58]. The experimental data for INS-1 cells in the references [57] was used for the comparison.

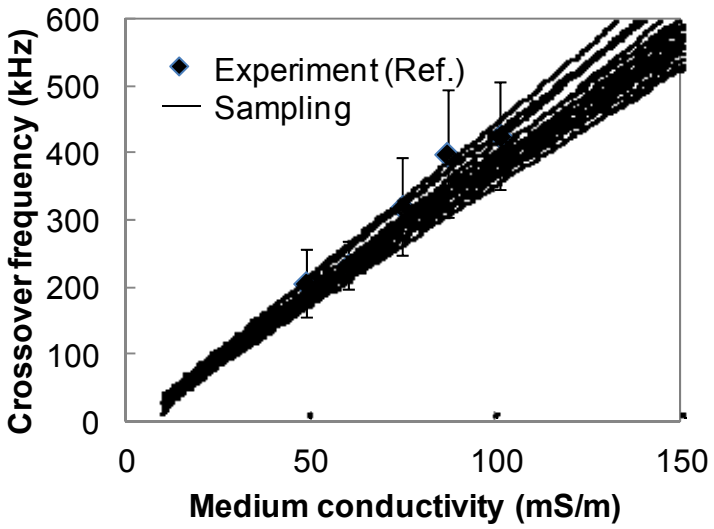

Figure 6 σ_m-f_{xo} data for INS-1 cells. Reproduced from [57]. Estimated σ_m-f_{xo} lines for 20 cells extracted with the sampling algorithm.

Table 1 Sampling ranges for cell properties.

Cell properties	Sampling ranges
Membrane conductivity (σ_{mem})	$10^{-7} \sim 10^{-5}$ S/m
Membrane permittivity (ε_{mem})	$1\varepsilon_0 \sim 50\varepsilon_0$
Cytoplasm conductivity (σ_{cyto})	0.01 ~ 2 S/m
Cytoplasm permittivity (ε_{cyto})	$50\varepsilon_0 \sim 150\varepsilon_0$

Figure 6 shows the experimental data of σ_m-f_{xo} for INS-1 cells, which is reproduced from [57]. Also, the estimated σ_m-f_{xo} lines by the sampling algorithm were plotted as solid lines. The lines correspond to 20 random cells satisfying the experimental data. With the dimension of 5.30 μm-radius and 5 nm-thick membrane, random cells having various cell properties were sampled in the ranges given in Table 1. The average of cell radius was used in the sampling-based approximation for direct comparison with the reference. In the reference, the cell radius showed the variation from 4.96 to 5.72 μm at 5 different medium conductivities, and the average value was used for the low frequency approximation. Among the sampled cells, the cells having a crossover frequency in the ranges of the error bar for the 5 medium conductivities were selected.

Table 2 Comparison of cell parameters extracted by the sampling-based approximation, the low frequency approximation, and 5 level approximations. The value in parentheses shows the relative error compared to that of the sampling-based approximation.

	Sampling	Low freq.	Level 5	Level 4	Level 3	Level 2	Level 1
G_{mem} (S/m^2)	1,041	600 (42.3%)	889 (14.6%)	901 (13.4%)	935 (10.2%)	927 (11.0%)	984 (5.8%)
C_{mem} (mF/m^2)	10.30	9.96 (3.3%)	9.90 (3.9%)	9.82 (4.7%)	10.11 (1.8%)	10.04 (2.5%)	9.91 (3.8%)
σ_{cyto} (S/m)	1.06	N/A	N/A	1.24 (17.0%)	1.23 (16.0%)	1.23 (16.0%)	1.24 (17.0%)
$\varepsilon_{cyto}/\varepsilon_0$	100	N/A	N/A	N/A	N/A	112 (12%)	134 (34%)

Table 2 represents the values for the cell parameters extracted by the sampling-based-, the low frequency-, and the 5-level approximation by Lei et al.. The parameters are the conductance and capacitance of membrane (G_{mem} and C_{mem}) and the conductivity and permittivity of cytoplasm (σ_{cyto} and $\varepsilon_{cyto}/\varepsilon_0$. G_{mem} and C_{mem} were employed for direct comparison with the reference. In the reference, G_{mem} and C_{mem} were extracted by the low frequency approximation. The parameters are defined as below:

$$G_{mem} = \frac{\sigma_{mem}}{t_{mem}} \tag{2.9}$$

$$C_{mem} = \frac{\varepsilon_{mem}}{t_{mem}} \tag{2.10}$$

The average values of 1,041 S/m^2, 10.30 mF/m^2, 1.06 S/m, and 100 were obtained for G_{mem}, C_{mem}, σ_{cyto}, and ε_{cyto} by the sampling-based approximation. For the extracted parameters by the low frequency- and the 5-level approximations, the relative errors (%) compared to the sampling-based approximation are indicated in parentheses under the average value. In the low frequency approximation, the values for G_{mem} and C_{mem} were extracted, and the discrepancies with the sampling-based approximation were 42.3% and 3.3%, respectively. In the 5-level approximation, 2~4 cell parameters were extracted depending on the level from 5 to 1. For the lower levels, the more cell parameters were extracted. For example, only two parameters of G_{mem} and C_{mem} could be approximated in the level 5 approximation while 4 parameters including σ_{cyto} and ε_{cyto} were derived with the level 1 and 2 approximations. In all the levels of approximation, G_{mem} showed less than 15% difference with the sampling-based approximation. For C_{mem}, the discrepancy was less than 5%. The maximum errors for σ_{cyto} and ε_{cyto} were 17 and

34%, respectively.

To investigate the reason of the discrepancy among the approximations, the plot of σ_m-f_{xo} line for the extracted cells by the sampling algorithm was investigated in conjunction with the distribution of the properties.

Figure 7 shows the σ_m-f_{xo} line in the extended region from Fig. 6 with a log scale. The box with a red dashed line in Fig. 7 is matched with the region of Fig. 6. The σ_m-f_{xo} lines are linear in the boxed region while a non-linear relation between σ_m and f_{xo} is shown in the other regions. The problem of the low frequency approximation can be explained by the non-linear region of σ_m-f_{xo} line. In the low frequency approximation, a best fitting line was approximated with a linear equation. Therefore, the low frequency approximation is valid only in the limited region.

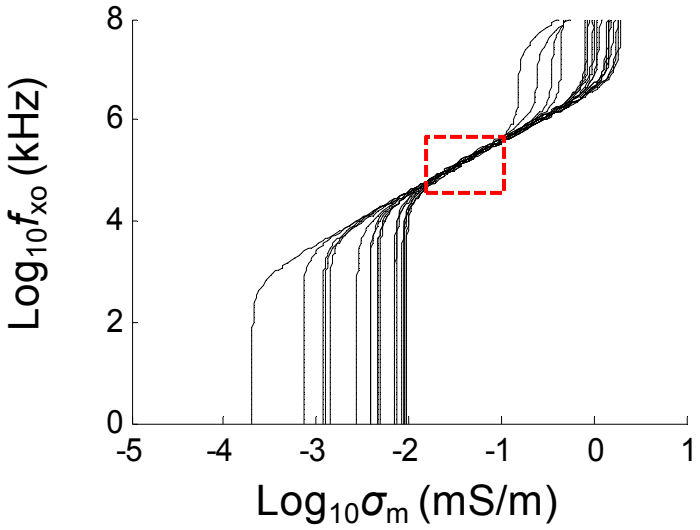

Figure 7 The extended plot of σ_m-f_{xo} lines for 20 sampled cells from Fig. 6.

Figure 8 represents the distribution of cell parameters for 1,000 cells extracted by the sampling algorithm. Figure 8A shows the histogram of G_{mem}. A uniform distribution is shown along the sampling range from 0 to 2000 S/m^2. For C_{mem}, a normal distribution is obtained with a mean value of 10.3 mF/m^2 in Fig. 8B. In Fig. 8C, σ_{cyto} shows a uniform distribution in the range over 0.1 S/m. The histogram of $\varepsilon_{cyto}/\varepsilon_0$ in Fig. 8D has the same form as that of G_{mem}, which shows a uniform distribution in the sampling range. From the distribution plot, it is expected that only C_{mem} can be properly estimated from the given experimental data in Fig. 6. In other words, the sampling algorithm provides the information about the reliability in estimation of cell parameters with the distribution plot while the 5-level approximation does not.

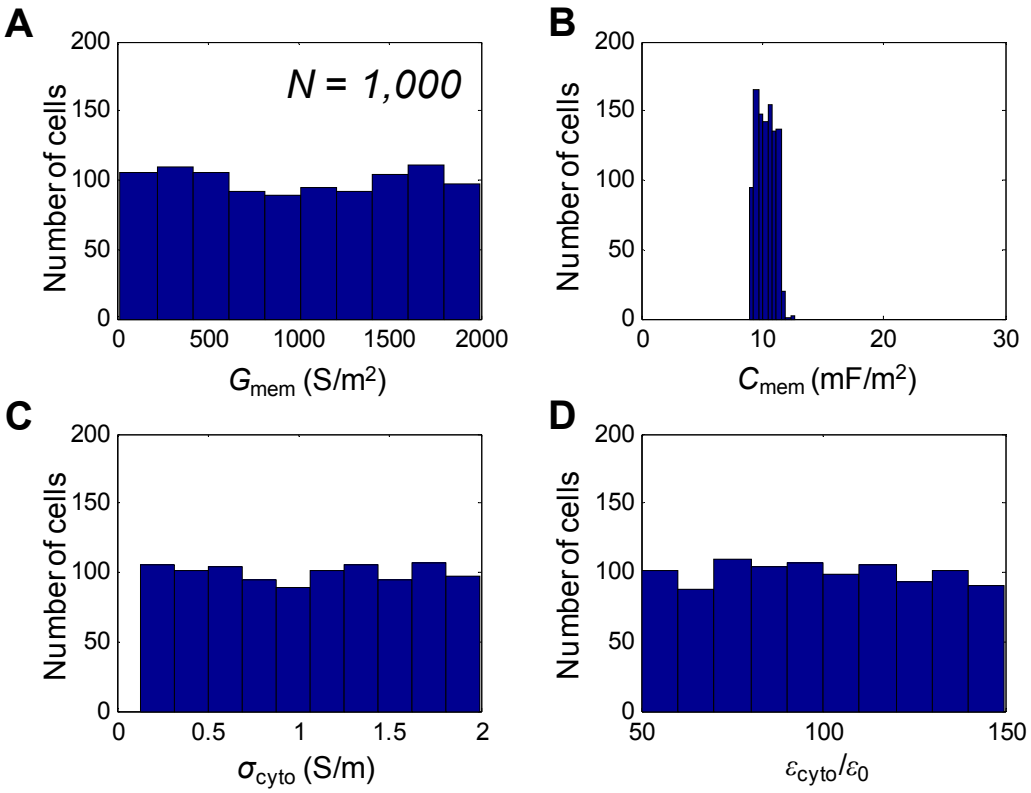

Figure 8 Histograms of G_{mem} (A), C_{mem} (B), σ_{cyto} (C), and $\varepsilon_{cyto}/\varepsilon_0$ (D) for 1,000 extracted cells by the sampling algorithm.

2.5 Summary

In summary, a sampling-based approximation was proposed to estimate cell properties in DEP experiment. The sampling-based approximation was validated its accuracy of estimation by comparing with the estimation from the previous approaches using the low frequency approximation and the 5-level approximation. In comparison to the previous approaches, the sampling-based approximation enabled rigorous estimation of cell parameters without any assumptions unlike the previous approaches. The sampling-based approximation can simplify the process for estimation of cell parameters from experimental data. Also, DEP experiment for cell characterization can be evaluated on the basis of the distribution of estimated cell parameters.

Chapter 3: Characterization of cell polarization under an AC field

3.1 Background

Dielectrophoresis (DEP) is the movement of a particle in a non-uniform electric field due to the induced dipole moment. DEP force on a particle is determined by particle characteristics such as sizes, shapes, electrical properties in combination with the electrical properties of suspending medium. Using the distinct characteristics of DEP, microscale- and nanoscale particles have been manipulated, separated and characterized [17, 52]. DEP has shown potential for testing biological particles [53]. In particular, it has been proven that DEP could differentiate target cells from non-targeted cells for cancer diagnosis[54], antibiotic resistance test[25], and toxicity test[26].

DEP spectroscopy scanning various frequencies of an AC electric field has been used to differentiate subtle variations of electric properties of cells. To analyze the DEP spectroscopy data, a cell could be modeled as a sphere or an ellipsoid having a single- or multiple shells [26, 32, 33]. In DEP experiment, cells can be attracted to or repelled from electrodes depending on the polarizability. The number of captured cells is counted, which is related with the magnitude of the polarizability. The counted number is normalized, which is compared with a polarization factor derived from the analytical model. The polarization factor is the Clausius-Mossotti factor (K_{CM}) proportional to the change of DEP force according to applied frequency, cell geometry, and the electrical properties of cells and medium. However, the cell counting method could be limited for the positive K_{CM} of cells because cells are not captured for negative K_{CM}. Also, the number of

captured cells might not represent solely the DEP effect due to the interference of frequency-dependent electrohydrodynamic effect [43, 47].

To estimate cell properties, two crossover frequencies (f_{xo1} and f_{xo2}) can also be used in coupling with a single shell model [18, 34]. f_{xo1} is the frequency at which the sign of DEP force is changed from negative to positive while f_{xo2} is the frequency at which the sign is changed from positive to negative. This approach is more reliable than the cell counting method because only the two frequencies need to be detected. In addition, electrohydrodynamic effects may not interfere with the detection unlike the cell counting method.

The main challenge to use DEP for the cell characterization is the limited information obtained from DEP experimental data. In other words, only the two crossover frequencies can be used to estimate four cell properties. To overcome this challenge, a comprehensive understanding about the polarization of cells and the relation to the cell properties is essential. To clarify the relation among the cell polarization, the cell properties, and the experimental conditions, a sensitivity analysis can be conducted. A local sensitivity analysis has been used to study a target parameter effect on K_{CM} analytically by assuming other variables as constants [34, 59]. However, the local sensitivity analysis may not give comprehensive information about the cell behavior upon DEP because numerous combinations of multiple cell properties should be investigated. To overcome the challenges, multi-dimensional analysis considering all the related variables is essential to investigate numerous combinations of multiple cell properties.

In this study, we present a novel sampling-based approach for rigorous DEP characterization of a cell. Using both methods of random- and Latin

hypercube sampling (LHS), data sets of virtual cells having various cell properties are generated within given boundaries. In various experimental conditions, the dependency of the polarization factor (K_{CM}) on cell's properties is investigated through a regression analysis for the sampled data. Then, optimal experimental conditions are suggested to detect the change of target properties in a cell. To this end, the advantage of the sampling-based approach is evaluated by predicting various combinations of the properties for a target cell.

3.2 Numerical method

A sampling-based approach was employed to conduct a multi-dimensional analysis considering all the parameters in a model system including the cell properties, the frequency, and the medium properties. According to a selected cell model, the parameters for cell characterization were determined. Then, the parameter sets for cell properties were generated in given ranges. In this study, all the numerical results were generated by MATLAB.

Without a sampling method, a huge number of cases should be analyzed. For example, if the dimensions of each parameter for a single-shell model (4 electrical properties of a cell) are divided by 100 cases each, the total number of combinations is 10^8. Using a sampling method, only 10^2 or 10^3 combinations can represent all the cases. After the sampling, the polarization factors (K_{CM}) for the sampled cells were computed using the input parameters of cell geometries and experimental conditions. Subsequently, the computed K_{CM} data was used for two kinds of analyses.

To find out optimal experimental conditions for detection of the change in cell properties, a global sensitivity analysis was conducted in terms of cell properties. The experimental parameters were the frequency (f) and the conductivity of medium (σ_m). The other analysis was to estimate the properties of a target cell with known dimensions from experimental data. The crossover frequencies of sampled cells having the same dimensions as a target cell were extracted. Based on the measured crossover frequencies in experiment, the sampled cells having the similar crossover frequencies were selected to estimate the cell properties. Each analysis step is described below.

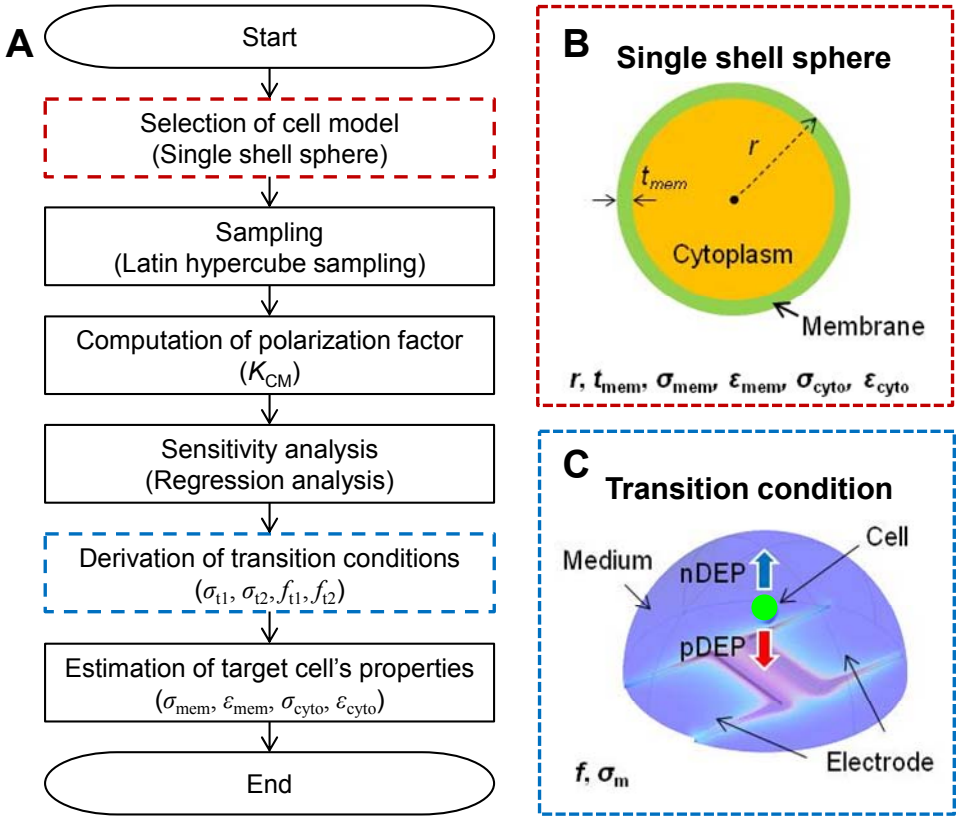

Figure 9 A: Analysis procedure. B: Single shell sphere model with cell properties. C: Schematics of DEP experiment to find transition condition of frequency (f) and medium conductivity (σ_m).

3.2.1 Model system

Figure 9A shows the model system for DEP characterization of a cell. A cell suspended in a medium can be either attracted to- (positive DEP) or repelled from (negative DEP) electrodes depending on the polarization. With varying the frequency (f) of applied voltage on the electrodes and the conductivity of medium (σ_m), the polarization of the cell is changed in experiment. Then, the cell properties are estimated from the experimental data based on a cell model.

A cell can be modeled as a spherical- or ellipsoidal particle covered with a single-shell or multi-shells [26, 32, 33]. Two kinds of cell models were considered in this study. A single-shell sphere model (Fig. 9B) was used for a sensitivity analysis. The model consisted of a conductive cytoplasm covered with a nonconductive membrane. Four parameters, the conductivities (σ) and the permittivities (ε) of membrane (mem) and cytoplasm (cyto), were used to characterize a cell with two shape parameters, the cell radius (r) and the membrane thickness (t_{mem}).

To estimate the properties of bacterial cells, a double-shell ellipsoid model (Fig. 9C) was employed to compare the sampling-based approach with the least square method. A cell wall was added onto a single shell model. The shape parameters were the length of cell for long- ($2a$) and short axes ($2b$), the wall thickness (t_{wall}), and the membrane thickness (t_{mem}).

3.2.2 Parameters for sampling

For a single-shell sphere model, there were a total of 9 parameters composed of 3 experimental conditions and 6 cell properties (Table 3). Among the 3 experimental parameters, the frequency of an applied electric field (f) and the conductivity of a medium (σ_m) were the parameters that could be controlled in experiment. The medium permittivity (ε_m) was assumed as constant due to the small variation in water-based solution [60]. f ranged from 1 to 10^9 Hz, which was typical for DEP experiment. For σ_m, the lower bound was the conductivity of deionized water (5.5 μS/m) while the upper bound was the conductivity of 1×PBS (phosphate buffered saline) of 1.6 S/m.

In this study, two cell radii of 0.1 and 10 μm were modeled in consideration of bacteria and mammalian cells [61], respectively. Although most bacteria were greater than 0.5 μm, 0.1 μm of radius was used to study the size dependency of K_{CM}. The membrane thickness of both cells was set to 10 nm. For the sampling, the 4 electric properties of a cell were the membrane conductivity (σ_{mem}), the membrane permittivity (ε_{mem}), the cytoplasm conductivity (σ_{cyto}), and the cytoplasm permittivity (ε_{cyto}). The sampling range of the cell properties was determined in consideration of the reported values in literatures [33, 62, 63]. σ_{mem} of a viable cell was smaller than 10^{-5} S/m. σ_{mem} could increase when the cell was damaged or became non-viable [33]. The lower bound of σ_{mem} was 10^{-7} S/m that was 2 orders magnitude smaller than the lower bound of σ_m of 10^{-5} S/m. σ_{mem} smaller than 10^{-7} S/m was not considered because such a large difference between σ_{mem} and σ_m might not cause the change for K_{CM}. σ_{cyto} ranged from 10^{-2} to 10^0 S/m [33, 62, 63], which could vary due to the increase of the membrane permeability or

the malfunction in cell metabolism. The relative permittivity of the membrane ranged from 1 to 20. In estimation, ε_{mem} could be changed in coupling with membrane thickness [64]. For example, with increase of the thickness, ε_{mem} could increase. In this study, ε_{mem} was used with the membrane thickness of 10 nm. The relative permittivity of cytoplasm containing DNA and protein molecules in buffer ranged from 40 to 80. The permittivity value decreased with increasing concentrations of DNA and protein [65]. Water had a relative permittivity of 80. The relative permittivities of DNA and protein molecules were in the range of 2~10 [66-68]. For the double-shell ellipsoid model, the ranges of the parameters were used as in the reference [34].

Table 3 Parameters, the values and the upper and lower bounds for sampling.

	Parameters	Values/Sampling ranges
Experimental conditions	Applied voltage frequency (f)	$10^0 \sim 10^9$ Hz
	Medium conductivity (σ_m)	$10^{-5} \sim 10^0$ S/m
	Medium permittivity (ε_m)	$80\varepsilon_0$
Cell properties 1 (single-shell sphere)	Cell radius (r)	0.1 μm & 10 μm
	Membrane thickness (t_{mem})	10 nm
	Membrane conductivity (σ_{mem})	$10^{-7} \sim 10^{-5}$ S/m
	Membrane permittivity (ε_{mem})	$1\varepsilon_0 \sim 20\varepsilon_0$
	Cytoplasm conductivity (σ_{cyto})	$10^{-2} \sim 10^0$ S/m
	Cytoplasm permittivity (ε_{cyto})	$40\varepsilon_0 \sim 80\varepsilon_0$
Cell properties 2 (double-shell ellipsoid)	Long axis ($2a$)	3.0 μm
	Short axis ($2b$)	1. 5 μm
	Wall thickness (t_{wall})	50 nm
	Membrane thickness (t_{mem})	8 nm
	Wall conductivity (σ_{wall})	$10^{-4} \sim 10^{-1}$ S/m
	Wall permittivity (ε_{wall})	$10\varepsilon_0 \sim 100\varepsilon_0$
	Membrane conductivity (σ_{mem})	$10^{-7} \sim 10^{-3}$ S/m
	Membrane permittivity (ε_{mem})	$1\varepsilon_0 \sim 20\varepsilon_0$
	Cytoplasm conductivity (σ_{cyto})	$10^{-2} \sim 10^0$ S/m
	Cytoplasm permittivity (ε_{cyto})	$40\varepsilon_0 \sim 80\varepsilon_0$

3.2.3 Sampling for sensitivity analysis

Latin hypercube sampling (LHS) was conducted to generate virtual cells having various properties in the given ranges. Compared to a random sampling method, LHS allowed for analysis of the full region with equal probability intervals for each sampling parameter [69]. Also, LHS was robust for a sensitivity analysis when the sample size was relatively small [70]. The number of sampled cells was 1,000 (i.e. N_s=1,000) for the sensitivity analysis.

3.2.4 Computation of polarization factor

For a homogeneous spherical particle, K_{CM} is determined by the particle conductivity (σ_p) and permittivity (ε_p) with 3 additional parameters, the angular frequency of applied voltage (ω), the medium conductivity (σ_m) and the medium permittivity (ε_m):

$$K_{CM} = \frac{\varepsilon_p^* - \varepsilon_m^*}{\varepsilon_p^* + 2\varepsilon_m^*} \tag{3.1}$$

where ε^* is the complex permittivity which is a combined property of the permittivity and the conductivity ($\varepsilon^*=\varepsilon-i\sigma/\omega$). If the particle model is changed to a single-shell sphere model, ε_p^* in Eq. (3.1) is replaced with the effective complex permittivity ($\varepsilon_{p\_eff}^*$) [31]:

$$\varepsilon_{p\_eff}^* = \varepsilon_{mem}^* \frac{r^3/(r-t_{mem})^3 + 2\varepsilon_i^*}{r^3/(r-t_{mem})^3 - \varepsilon_i^*} \tag{3.2}$$

ε_i^* is the combined complex permittivity of cytoplasm and membrane ($\varepsilon_i^*=(\varepsilon_{cyto}^*-\varepsilon_{mem}^*)/(\varepsilon_{cyto}^*+2\varepsilon_{mem}^*)$). ε_{cyto}^* and ε_{mem}^* are the complex permittivities of cytoplasm

and membrane, respectively. For a double-shell model, the effective complex permittivity for a particle is computed by replacing the effective complex permittivity of the single-shell model with ε_{cyto}^* and the complex permittivity of the additional layer with ε_{mem}^*. The equation for the ellipsoidal model having double shells is described as below:

$$K_{CM} = \frac{\varepsilon_2^* - \varepsilon_m^*}{\varepsilon_m^* + (\varepsilon_2^* - \varepsilon_m^*)A_3} \tag{3.3}$$

$$\varepsilon_2^* = \varepsilon_{wall}^* \frac{\varepsilon_{wall}^* + (\varepsilon_1^* - \varepsilon_{wall}^*)A_2 + \lambda_2(\varepsilon_1^* - \varepsilon_{wall}^*)(1 - A_3)}{\varepsilon_{wall}^* + (\varepsilon_1^* - \varepsilon_{wall}^*)A_2 - \lambda_2(\varepsilon_1^* - \varepsilon_{wall}^*)A_3} \tag{3.4}$$

$$\varepsilon_1^* = \varepsilon_{mem}^* \frac{\varepsilon_{mem}^* + (\varepsilon_{cyto}^* - \varepsilon_{mem}^*)A_1 + \lambda_1(\varepsilon_{cyto}^* - \varepsilon_{mem}^*)(1 - A_2)}{\varepsilon_{mem}^* + (\varepsilon_{cyto}^* - \varepsilon_{mem}^*)A_1 - \lambda_1(\varepsilon_{cyto}^* - \varepsilon_{mem}^*)A_2} \tag{3.5}$$

$$\lambda_2 = \frac{(L/2 - t_{wall})(r - t_{wall})^2}{Lr^2/2} \tag{3.6}$$

$$\lambda_1 = \frac{(L/2 - t_{wall} - t_{mem})(r - t_{wall} - t_{mem})^2}{(L/2 - t_{wall})(r - t_{wall})^2} \tag{3.7}$$

$$A_i = \frac{q_i}{\left(q_i^2 - 1\right)^{3/2}} \ln\left(q_i + \left(q_i^2 - 1\right)^{1/2}\right) - \frac{1}{q_i^2 - 1}, \quad i = 1,2,3 \tag{3.8}$$

$$q_3 = \frac{L/2}{r} \tag{3.9}$$

$$q_2 = \frac{L/2 - t_{wall}}{r - t_{wall}} \tag{3.10}$$

$$q_1 = \frac{L/2 - t_{wall} - t_{mem}}{r - t_{wall} - t_{mem}} \tag{3.11}$$

In the ellipsoidal model, K_{CM} on the short axis was neglected because of the relatively smaller value than that for the long axis.

Using above equations, $K_{CM}(i,j,k)$ of k^{th} sampled cell was computed using $\sigma_m(i)$ and $f(j)$. i, j, and k were integers from 1 to $N_{\sigma m}$, N_f, and N_s, respectively. For the sensitivity analysis, both $N_{\sigma m}$ and N_f were 100, and N_s was 1,000. Therefore, the total number of K_{CM} data was 10^7 for 1,000 cells (N_s) at 10,000 experimental conditions ($N_{\sigma m} \times N_f$).

3.2.5 Sensitivity analysis

To investigate optimal experimental conditions for detection of property variation, the dependency of K_{CM} on cell properties was studied through a regression analysis with the K_{CM} data of the sampled cells. The sensitivity of a dependent variable to the variation of an explanatory variable was represented with a regression coefficient. The coefficient was the slope of a line approximated with the scattered data by using a least square method. In this study, a multiple regression analysis was conducted to investigate the sensitivity of K_{CM} to multiple cell properties. The regression coefficients (b_0, b_1, b_2, b_3, and b_4) at 10,000 experimental conditions were obtained from the approximation equation as:

$$\hat{K}_{CM}(i,j) = b_0(i,j) + b_1(i,j)\frac{\log_{10}\sigma_{mem}}{\log_{10}10^{-5} - \log_{10}10^{-7}S/m} + b_2(i,j)\frac{\varepsilon_{mem}}{20\varepsilon_0 - \varepsilon_0} + b_3(i,j)\frac{\log_{10}\sigma_{cyto}}{\log_{10}10^{0} - \log_{10}10^{-2}S/m} + b_4(i,j)\frac{\varepsilon_{cyto}}{80\varepsilon_0 - 40\varepsilon_0} \quad (3.12)$$

A real part of K_{CM} is approximated as a linear function of cell properties (σ_{mem}, ε_{mem}, σ_{cyto}, and ε_{cyto}) at the condition of $\sigma_m(i)$ and $f(j)$. b_1, b_2, b_3, and b_4 represent the sensitivity of K_{CM} to σ_{mem}, ε_{mem}, σ_{cyto}, and ε_{cyto}, respectively. To normalize the variation of the cell properties in the sampling range, each cell property was divided by the difference between the upper- and the lower bounds of the sampling range.

3.2.6 Selection of DEP spectroscopy data

To estimate the properties of a cell, either cell counting data or crossover frequencies of a cell can be used in coupling with a cell model [18, 34]. Between the two methods, the crossover frequency-based approach is more reliable. In the cell counting-based method, the frequency spectrum of captured number of cells is used, which can be interfered by electrohydrodynamic effects [43, 47]. On the other hand, the crossover frequency-based method measures two frequencies at which the sign of DEP force on the cell reverses from negative to positive (f_{xo1}) or from positive to negative (f_{xo2}) with increasing frequency. Therefore, the crossover frequency-based method was used in this study.

3.2.7 Comparison of the crossover frequencies extracted from the sampling and analytical equations

Using the 1,000 sampled data sets and σ_m of $10^{-1.5}$ S/m, two crossover frequencies of f_{xo1} and f_{xo2} were computed through the computation of K_{CM}. Then, the computed f_{xo1} and f_{xo2} were compared with those of the analytical equations based on a single shell model as below:

$$f_{xo1} = \frac{\sigma_m}{2\pi}\sqrt{\frac{2}{(S\varepsilon_{mem} - \varepsilon_m)(S\varepsilon_{mem} + 2\varepsilon_m)}} \tag{3.13}$$

$$f_{xo2} = \frac{\sigma_{cyto}}{2\pi}\sqrt{-\frac{1}{(\varepsilon_{cyto} - \varepsilon_m)(\varepsilon_{cyto} + 2\varepsilon_m)}}$$

(3.14)

where S is the membrane dimension factor as $S=(C+2)/(C-1)$. Since equations (3.13) and (3.14) were approximated with assumption of $\sigma_{cyto} >> \sigma_m >> S\sigma_{mem}$, the difference

of the crossover frequencies between the sampling method and the analytical equations was studied.

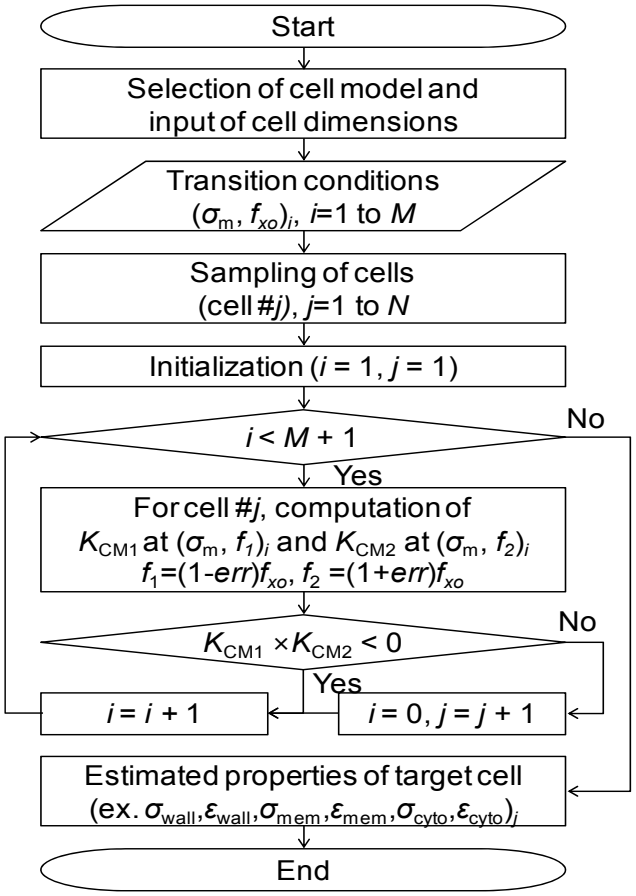

Figure 10 Algorithm for sampling-based estimation from DEP experimental data.

3.2.8 Estimation of cell properties with sampling method

The properties of a target cell were estimated by using the sampling method and compared with those from the least square method in reference[34]. For the estimation, f_{xo1} and f_{xo2} in the reference [34] were used. The target cell was modeled as a double-shell ellipsoid (Fig. 9C). The long- and short axes were 3 and 1.5 μm in lengths, respectively. Two shells were composed of a 50 nm-thick wall and an 8 nm-thick membrane.

In the sampling method, when 1,000 cells were sampled, two problems occurred. The sampling number of 1,000 was not sufficient to generate cells having the similar properties of the target cell. Without a large enough sampling number, the estimated properties could be case-sensitive without reliability. To generate an enough number of cells, the sampling was repeated until 100 cells of the properties with 10% tolerance to f_{xo1} and f_{xo2} were generated. The iteration algorithm is illustrated in Fig. 10. It was found that 100 cells were enough to represent a property. The other problem was that the LHS algorithm was not efficient to generate 1,000 cells with the iteration algorithm. To improve the computation efficiency, RS was used in the iteration algorithm.

To propose new experimental conditions for estimation of cell properties, a 4 transition condition method was proposed. The 4 transition condition method used f_{xo1} and f_{xo2} and two transition medium conductivities (σ_{t1} and σ_{t2}). The estimation results for the crossover frequency method and the 4 transition condition method were compared.

3.3 Result and Discussion

Figures 11A and 11B show K_{CM} of 1,000 sampled cells for the case 1 of σ_m = 1 mS/m and f = 10 kHz, and the case 2 of σ_m = 10 mS/m and f = 10 MHz, respectively. In both graphs, the sampled cells are numbered from 1 to 1,000. Fig. 11C and 11D show the dependency of K_{CM} on σ_{cyto} for the cases 1 and 2, respectively. K_{CM} of the 1,000 sampled cells is randomly distributed in the case 1 while a clear correlation between K_{CM} and σ_{cyto} is shown for the case 2. As the data are more scattered, the correlation between K_{CM} and the cytoplasm conductivity decreases. Thus the dependency between the cell properties and DEP characteristic is graphically shown by using the sampling method.

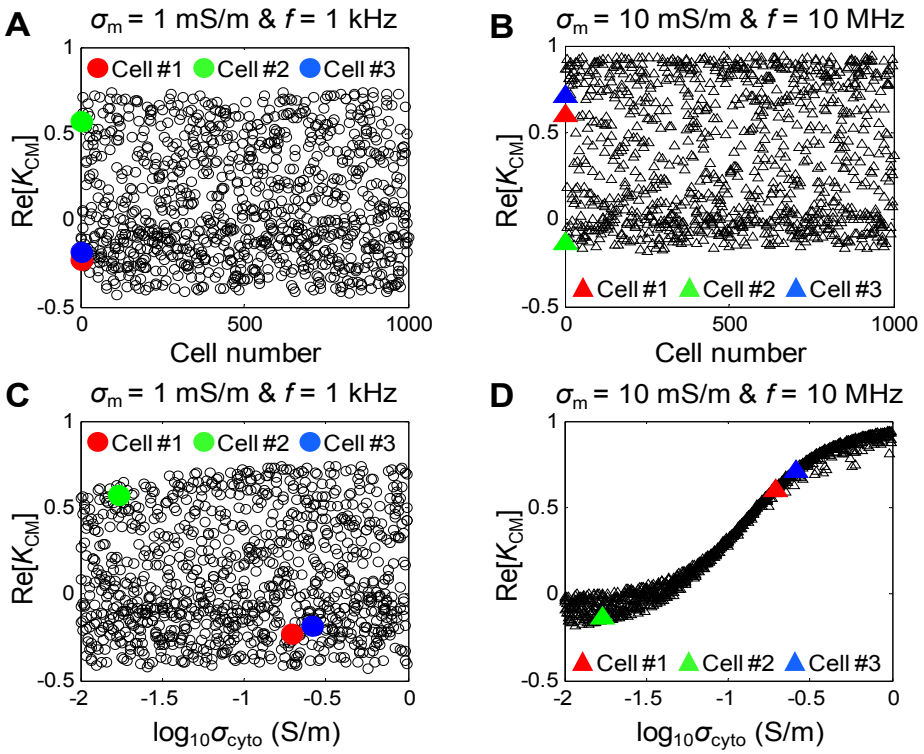

Figure 11 A, B: Scatter plots of K_{CM} for 1,000 sampled cells at two conditions, case 1: σ_m =1 mS/m and f=10 kHz; case 2: σ_m =10 mS/m and f=10 MHz. C, D: Rearranged K_{CM} data of Fig. 11A (C) and Fig. 11B (D) with respect to the conductivity of cytoplasm.

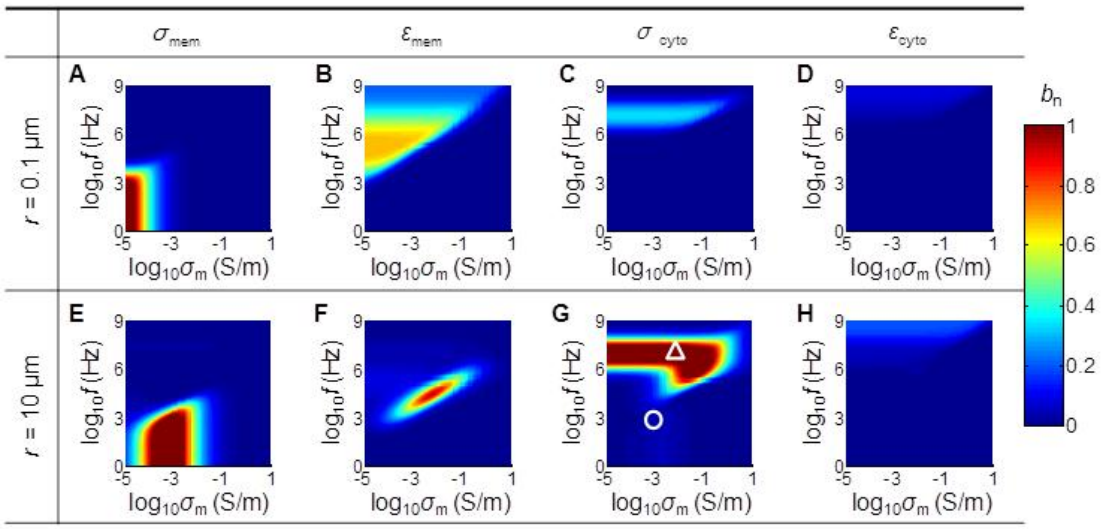

Figure 12 Mapping of regression coefficients (b_1, b_2, b_3 and b_4) for cell properties (σ_{mem}, ε_{mem}, σ_{cyto}, and ε_{cyto}) of different sized cells (r=0.1 μm and r=10 μm) with the membrane thickness of 10 nm. The color represents the value of the regression coefficient.

To quantify the correlation between the cell properties and K_{CM}, a sensitivity analysis was conducted for the 1,000 sampled cells. In Figure 12, the regression coefficients (b_n) for K_{CM} in equation (3.12) are mapped in the domain of σ_m and f. Figures 12A~D show the mapping of b_1, b_2, b_3, and b_4 for σ_{mem}, ε_{mem}, σ_{cyto}, and ε_{cyto} for the sampled cells having 0.1 μm radius. The magnitude of b_n is represented with the color bar in the graphs. When b_n is 0, K_{CM} is not sensitive to a property. As the absolute value of b_n increases, the sensitivity increases. In terms of DEP experiment, as b_n is greater, the variation of the measured parameters should be larger. In Fig. 12A, the sensitive region for σ_{mem} is located at σ_m of 10^{-5}~10^{-4} S/m and f of 10^0~10^4 Hz. When σ_m is 10^{-5} S/m, the sensitivity for ε_{mem} is greater than 0.5 at f of 10^3~10^7 Hz (Fig. 12B). With the increase of σ_m, the sensitive region for f decreases. When σ_m is smaller than 10^0 S/m, b_3 for σ_{cyto}, is around 0.3 at f of 10^6~10^8 Hz (Fig. 12C). When f is greater than 10^7 Hz, b_4 for ε_{cyto} is smaller than 0.1

at σ_m of 10^{-5}~10^{-1} S/m (Fig. 12D).

Figures 12E~H shows b_n for the cell having 10 μm in radius. Since the cell radius increases with a constant membrane thickness of 10 nm, the sensitive region could be shifted, reduced or expanded. The b_n values were also changed upon the increase of the radius from 0.1 to 10 μm. When the scatter plots in Fig. 11C and 11D were compared with the sensitivity mapping in Fig. 12G, the correlations of K_{CM} and σ_{cyto} in Fig. 11C and 11D were quantified as b_3 = 0.04 (circle) and 1.28 (triangle) in Fig. 12G, respectively. Thus the mapping of the sensitivity could quantify the graphical correlation of the sample cells.

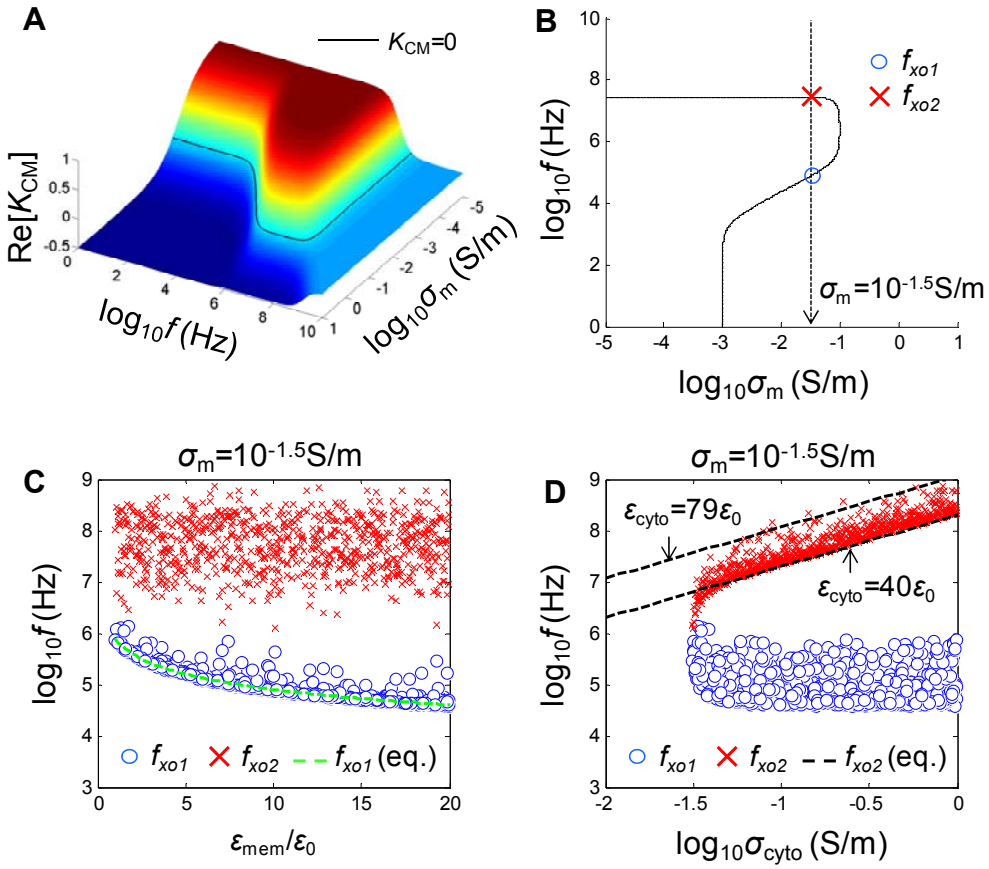

Figure 13 A: Mapping of K_{CM} for a cell (r = 10 μm, t_{mem} = 10 nm, σ_{mem} = 10^{-6} S/m, ε_{mem} = $10\varepsilon_0$, σ_{cyto} = 0.1 S/m, and ε_{cyto} = $60\varepsilon_0$) with a condition line of K_{CM}=0. The color represents the value of K_{CM} and a black solid line is the condition line. B: The condition line extracted from Fig. 13A. O indicates f_{xo1} and × indicates f_{xo2} when σ_m = $10^{-1.5}$ S/m. C, D: f_{xo1} and f_{xo2} for 1,000 sampled cells when σ_m = $10^{-1.5}$ S/m. Estimated f_{xo1} and f_{xo2} are indicated as dashed lines. Different values of ε_{cyto} are used for the two estimation lines (D).

In Fig. 13, f_{xo1} and f_{xo2} for the 1,000 sampled cells of a single-shell model are compared with those from equations (3.13) and (3.14). In Fig. 13A, the K_{CM} is shown for a specific cell (r = 10 μm, t_{mem} = 10 nm, $\sigma_{mem} = 10^{-6}$ S/m, $\varepsilon_{mem} = 10\varepsilon_0$, σ_{cyto} = 0.1 S/m, and $\varepsilon_{cyto} = 60\varepsilon_0$). The black solid line in Fig. 13A shows the transition conditions where the sign of K_{CM} is reversed. From the transition line, f_{xo1} and f_{xo2} of the cell are extracted when a medium conductivity is $10^{-1.5}$ S/m (Fig. 13B). In the same medium conductivity, f_{xo1} and f_{xo2} for the 1,000 sampled cells are plotted according to ε_{mem} and σ_{cyto} in Fig. 13C and 13D, respectively. The lines in the figures are f_{xo1} and f_{xo2} computed from equations (3.13) and (3.15). Most f_{xo1} and f_{xo2} using the sampling-based method agrees with those from the analytical values. The deviation of the sampling data from the equations is caused by the assumption of $\sigma_{cyto} \gg \sigma_m$ ($=10^{-1.5}$ S/m) in the equations. In addition, when a crossover frequency is not sensitive to ε_{mem} or σ_{cyto}, a line from the analytical equation does not exist. Using the sampling method, the crossover frequencies could be more precisely presented in comparison to the approximated equations because an assumption was not necessary.

Table 4 Estimated cell properties from the reference and the sampling-based method.

	σ_{wall} (S/m)	$\varepsilon_{wall}/\varepsilon_0$	σ_{mem} (S/m)	$\varepsilon_{mem}/\varepsilon_0$	σ_{cyto} (S/m)	$\varepsilon_{cyto}/\varepsilon_0$
Mietchenet al.	7×10^{-3}	77	1×10^{-6}	8	0.5	50
Castellarnau et al.	5.8×10^{-2}	78	2.6×10^{-4}	9.8	0.48	49.8
Sampling	1.3×10^{-3} ~7.5×10^{-3}	20 ~98	0.1×10^{-6} ~9.9×10^{-4}	5.7 ~20	0.22 ~0.62	41 ~79

For estimation of the properties of a target cell using the sampled cells, the DEP experimental data from the crossover frequency method were used. The estimated properties of the target cell were compared with those of the reference [34] using a least square method in Table 4. The properties from the sampling-based estimation are described as the minimum- and maximum values among the 100 cells in the iteration algorithm in Fig. 10. The sampling-based estimation predicted multiple combinations of cell properties while the two references presented single combination. When the least square method in the reference was used, the initial values for cell properties could dominate the estimated values. In the sampling-based approach, the cells satisfying an experimental result could be chosen among the sampled cells. In comparison to the reference result using a least square method, the sampling-based estimation could give all the possible combinations for the cell properties.

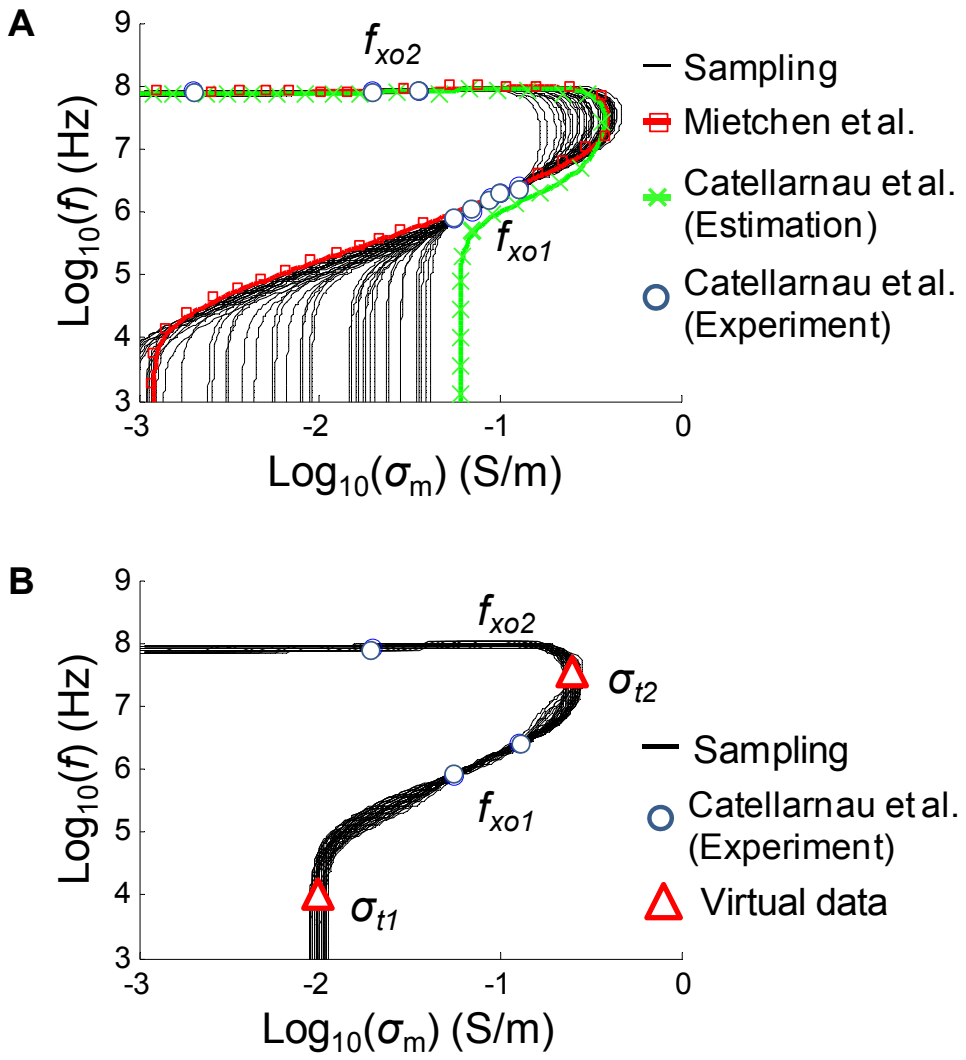

Figure 14 A: Estimated transition lines for the cells which passing the crossover frequencies measured from the experiment (blue circles) in the reference. Black solid lines are from the sampling-based estimation and red line with square and green line with × are from the references. B: Suggested experimental design for DEP characterization using additional two transition conditions of medium conductivity. Transition conductivity of medium indicated as red triangle is arbitrary selected.

Fig. 14A shows the transition lines for the cells estimated according to the target cell from the sampling-based estimation and the reference [34]. In the graph, the experimental data from the reference are represented as blue circles. The lines with cross- and square symbols represent transition lines from the reference [34]. The solid lines show the 100 transition lines estimated by the iteration algorithm in Fig. 10. The multiple lines were generated because the experimental data about f_{xo1} and f_{xo2} could not confine the cell properties. In other words, when the geometry of the cell components was known, the properties of ε_{mem}, ε_{wall}, σ_{cyto} and ε_{cyto} could be found but not the properties of σ_{mem} and σ_{wall}.

For more accurate estimation of the cell properties, the proposed 4-transition condition method measuring f_{xo1}, f_{xo2}, σ_{t1} and σ_{t2} was evaluated (Fig. 14B). In comparison to Fig. 14A, the 4 transition condition method could effectively confine the variation of the properties because all the properties of σ_{mem}, ε_{mem}, σ_{wall}, ε_{wall}, σ_{cyto} and ε_{cyto} were more accurately estimated by using the 4 transition condition method.

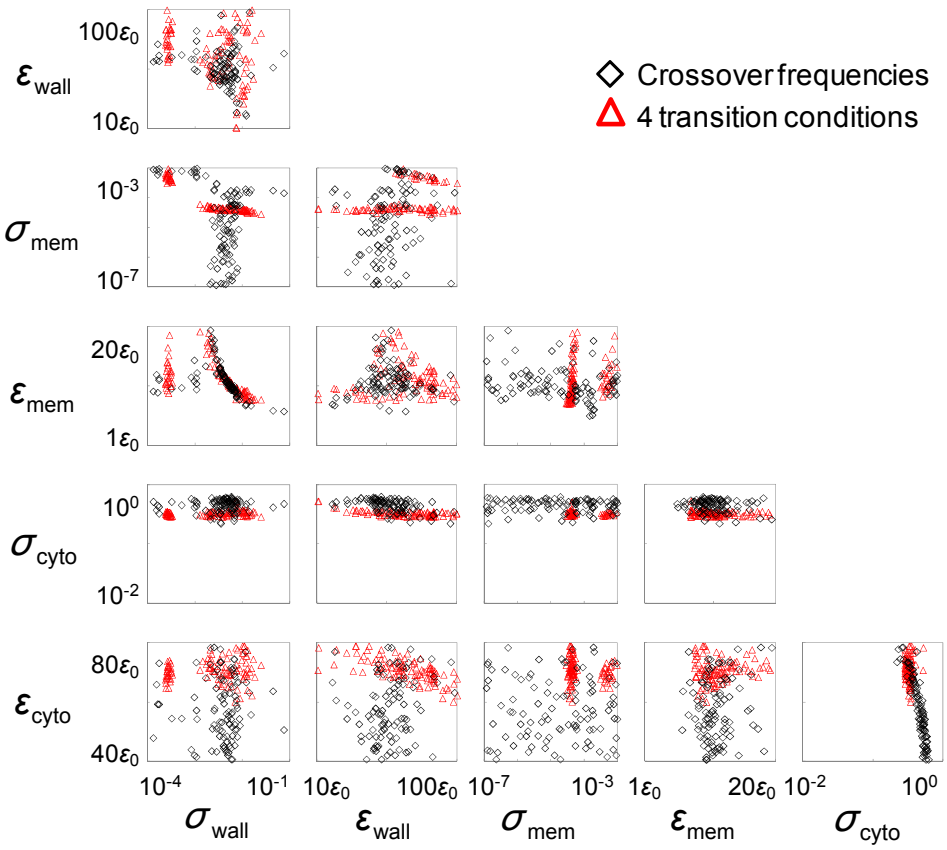

Figure 15 Scatter plots showing correlation between cell properties estimated from crossover frequencies and 4 transition conditions. Plot data for the crossover frequencies (black diamond) and the 4 transition conditions (red triangle) are related with Fig. 14A and Fig. 14B, respectively.

For estimation of cell properties, the 4 transition condition method was superior to the crossover frequency method. Fig. 15 shows the correlations among the properties of the 100 cells having the similar properties of the target cell. The properties estimated using the crossover frequency methods are shown as black diamond while those using the 4 transition condition method are as red triangles. Using the 4 transition condition method, the scattering of the properties was significantly reduced while the correlations among the properties were more clearly observed.

The sampling method was efficient to estimate cell properties from DEP spectroscopy data, in particular, when a complex model of a cell was employed. For a simple model, such as a single-shell sphere, it was straightforward to predict the change of ε_{mem} and σ_{cyto} from the analytical equation in Fig. 13. However, if a cell had ellipsoidal shape or multiple shells, the prediction became complicated due to the multiple dimensions of the cell properties. When the experimental data of f_{xo1} and f_{xo2} were given, ε_{mem}, ε_{wall}, σ_{cyto} and ε_{cyto} could be estimated for a double shell model in Fig. 14A. To estimate σ_{mem} and σ_{wall}, the 4 transition condition method was proposed. In combination with the sampling method, the properties of σ_{mem}, ε_{mem}, σ_{wall}, ε_{wall}, σ_{cyto} and ε_{cyto} could be rigorously estimated. Therefore, the sampling method was beneficial to estimate multiple parameters for a complex cell model.

3.4 Summary

In summary, a sampling-based method using both random sampling and Latin Hypercube sampling was used to estimate cell properties in DEP experiment. Using the sampling method, the polarization factor (K_{CM}) was graphically presented in contexts of cell properties. To quantify the relationship between K_{CM} and the cell properties, a sensitivity analysis in multi-dimensions was efficiently conducted. In comparison to the previous approach using a least square method, the sampling method enabled multi-dimensional analysis of the cell properties through the algorithm iterating the sampling method. The 4 transition condition method using σ_{t1}, σ_{t2}, f_{xo1} and f_{xo2} was newly proposed for rigorous estimation of cell properties according to the sensitivity mapping. The sampling-based analysis for DEP behavior of cells can offer an insight and rigorous analysis to characterize cells before- and after DEP experiment.

Chapter 4: DEP separation of viable and nonviable cells with a statistical modeling

4.1 Background

The alarming increase of multi-drug resistant tuberculosis (MDR-TB) has become a serious issue, especially with TB claiming over one million lives each year [71]. Drug resistance is associated with gene mutations, which frequently results from improper treatment of drug-susceptible patients. For drug-susceptibility tests, either phenotypic or genotypic methods can be used [72]. Genotypic methods can be very rapid with high sensitivity and specificity, but require skilled personnel with a relatively high cost. Also, for many antibiotics the genetic bases of resistance are highly complex or poorly understood. Phenotypic drug-susceptibility tests are based on detection of bacterial growth in the presence of antibiotics. Although very reliable and relatively cheap, standard methods require trained personnel and relatively slow, taking weeks for results.

As a phenotypic approach, dielectrophoresis (DEP) based on electrical polarization in a medium has been proposed as a means to rapidly determine cell viability [73-75]. Heat-killed cells were used as a model system to study DEP response in most cases [22, 26, 42, 76]. Since extensive heat could change the electric properties of cell wall and cytoplasm, the DEP behavior of cell could differ greatly between heat- and antibiotic-inactivated bacterial cells. DEP has shown promise as a rapid tool to test antibiotic susceptibility for various types of drugs and cells, such as human

myelogenous leukemia cells [26], *Staphylococcus epidermidis* [42], and *Escherichia coli* [76]. Drugs that altered the structure of the cell wall or membrane were observed to affect the DEP response. Hawkins *et al.* found similar results when characterizing *Mycobacterium smegmatis*, a fast growing, non-pathogenic species of *Mycobacterium*, with treatment of ethambutol [77]. Ethambutol is a drug that inhibits the production of arabinogalactan and thus affects cell wall structure. The reduction of arabinogalactan, which is a major component of the cell wall, by ethambutol caused a significant decrease in the effective permittivity of the cell, which resulted in detectable changes by DEP. Therefore, DEP may be a useful way to differentiate antibiotic-susceptible cells from antibiotic-resistant cells according to antibiotic-induced changes of the cell envelope and/or cytoplasm.

For the slow-growing pathogen *Mycobacterium tuberculosis* (MTB), first line drugs used to treat infected patients are rifampin (RIF) and isoniazid (INH). Treatment failure often results from resistance to one or both of these drugs [78, 79]. The action mechanism of RIF is the inhibition of mycobacterial transcription by targeting DNA-dependent β-subunit of RNA polymerase [80, 81]. RIF permeates through the cell structure to bind with the RNA polymerase and kill the cell. INH is a prodrug that enters the cell through passive diffusion [82]. The drug is activated by mycobacterial enzyme *katG* [83]. The activated form of the drug is a potent inhibitor of synthesis of mycolic acid for cell wall [84, 85], resulting in cell death. It has been reported that INH induces morphological changes in mycobacteria,

such as loss of structure or appearance of surface wrinkles and bulging [86, 87]. To date, the effects of RIF and INH on DEP behavior of MTB complex cells have not been investigated.

This study presents the study of DEP behavior of MTB complex cells treated with RIF and INH. RIF and INH are chosen for their significance in treatment of TB and also for their distinct mechanisms for cell death. RIF inhibits RNA synthesis without direct interaction with the cell envelope [88] while INH affects cell wall structure by inhibiting the synthesis of mycolic acid. As a surrogate marker of MTB, the TB vaccine strain *Mycobacterium bovis* (Bacillus Calmette-Guérin, BCG) is used in this study. BCG cells exposed to heat, RIF and INH are tested on planar electrodes with application of AC voltage. The experimental parameters are designed on the basis of our DEP analysis in conjunction with the drug mechanism. The parameters of the electrophysiology of BCG cells are estimated and related to the action mechanism using heat, RIF and INH. Through the numerical and experimental results, we evaluate whether the DEP approach can measure the effects of RIF and INH on *M. tuberculosis* complex cells.

It should be noted that the experiment in this chapter was conducted by Dr. Shin Inoue.

4.2 Theoretical approach

For characterization of BCG cells using DEP, the experimental setup is illustrated in Fig. 16A. When a liquid drop containing stained BCG cells is placed on the electrodes, DEP force is exerted on the cells upon application of an electric field with a function generator. In this experimental configuration, f_{xo} can be measured by observing the movement of cells with a fluorescence microscope. For modeling of a BCG cell, a double-shell ellipsoidal model (Fig. 16B) is applied to wall, membrane (mem), and cytoplasm (cyto) of a cell. Each part in a cell has two electrical properties, the conductivity (σ) and the permittivity (ε).

In this numerical study, the shift of a σ_m-f_{xo} line according to change of cell properties was analyzed by a sampling-based sensitivity analysis. As an example, Figure 16C shows the sensitive regions for each cell property near a σ_m-f_{xo} line. The sensitive regions are highlighted with the corresponding properties. The σ_m-f_{xo} line in the graph was computed based on the cell properties of $\sigma_{wall}=1.6\times10^{-3}$ S/m, $\varepsilon_{wall}=43\varepsilon_0$, $\sigma_{mem}=8.9\times10^{-6}$ S/m, $\varepsilon_{mem}=12\varepsilon_0$, $\sigma_{cyto}=0.55$ S/m, and $\varepsilon_{cyto}=58\varepsilon_0$. The values for cell properties were chosen by our preliminary results. The borders of positive- (pDEP) and negative DEP (nDEP) regions are the σ_m-f_{xo} line. When σ_m is smaller than $10^{-3.0}$ S/m, the shift of f_{xo} in the range of 10^7~10^8 Hz is dominated by the values of both σ_{cyto} and ε_{cyto} (yellow region). For σ_m of $10^{-3.0}$~$10^{-0.5}$ S/m, two f_{xo} are present. The lower- (green) and higher f_{xo} (red and blue) are affected by ε_{wall} & ε_{mem} and σ_{cyto} & ε_{cyto}, respectively. The lower f_{xo} (f_{xo1}) increases with the increase of σ_m while the higher f_{xo} (f_{xo2}) exists in the range of 10^7~10^8 Hz regardless of σ_m. The DEP approach can use both f_{xo1} and f_{xo2}. f_{xo2} is not commonly generated by a function generator due to the high frequency of 10^8 Hz.

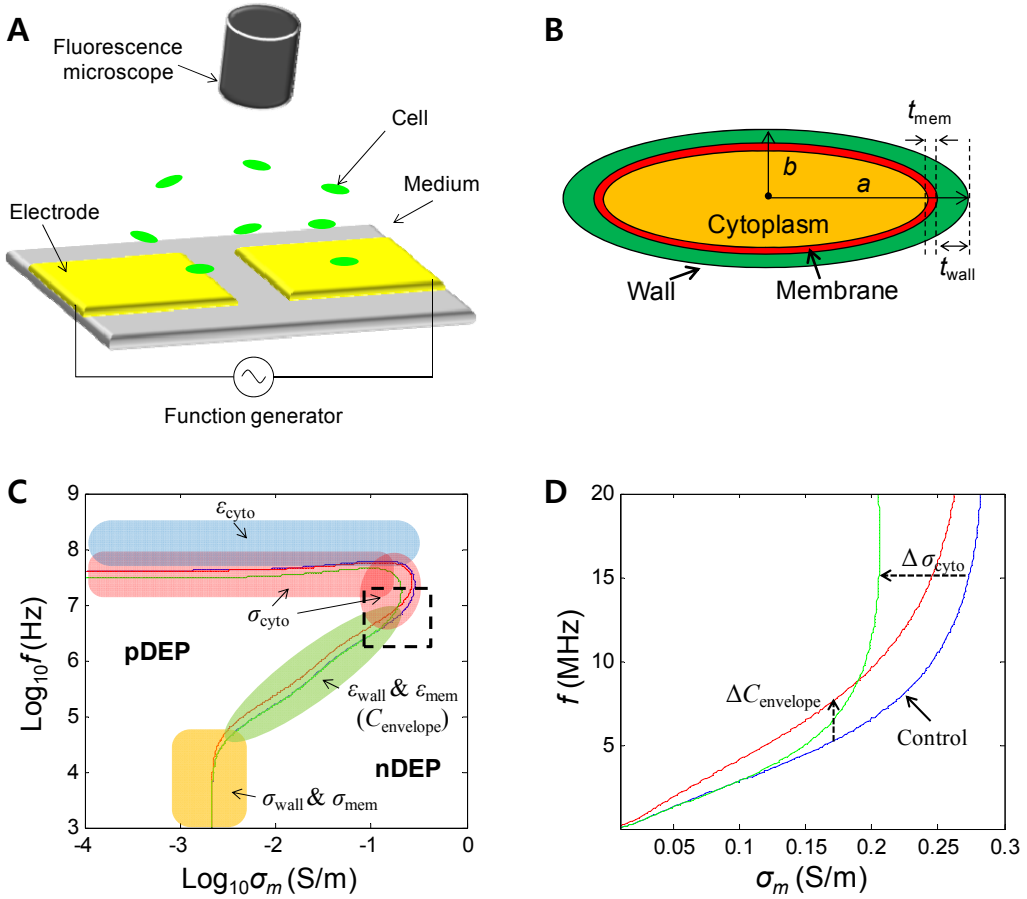

Figure 16 A: Schematic of an experimental setup. B: Double-shell ellipsoidal model of a BCG cell. C: Sensitive region of K_{CM} to the cell property change near the crossover frequency lines. The lines can be changed in the colored region due to cell properties. The dominant properties determining the location of the lines are described in the graph. DEP is separated into positive- (pDEP) and negative (nDEP) according to the crossover frequency lines. D: Non-log graph of the box with dashed lines in Fig. 16C. Three lines indicate three kinds of cells having different cell properties. Blue (Control): $\sigma_{wall}=1.59\times10^{-3}$ S/m, $\sigma_{mem}=8.87\times10^{-6}$ S/m, $C_{envelope} = 4.47\times10^{-3}$ F/m^2 ($\varepsilon_{wall}=43.0\varepsilon_0$ and $\varepsilon_{mem}=12.2\varepsilon_0$), $\sigma_{cyto}=0.55$ S/m and $\varepsilon_{cyto}=57.8\varepsilon_0$; Red: $\Delta C_{envelope} = -1.43\times10^{-3}$ F/m^2 ($\varepsilon_{wall}=30.0\varepsilon_0$ and $\varepsilon_{mem}=8.0\varepsilon_0$); Green: $\Delta\sigma_{cyto}= -0.15$ S/m.

To simplify the parameters of a cell's envelope (wall + membrane), a specific capacitance ($C_{envelope}$) of a cell is employed to combine the electric permittivities of ε_{wall} and ε_{mem} [89].

$$C_{envelope} = \frac{\varepsilon_{wall}\varepsilon_{mem}}{\varepsilon_{wall}t_{mem} + \varepsilon_{mem}t_{wall}} \tag{4.1}$$

where t_{wall} and t_{mem} are the thicknesses of a wall and a membrane of a cell. The thicknesses are combined with ε_{wall} and ε_{mem} to make a unit of specific capacitance (F/m^2).

To investigate the change of both envelope and cytoplasm of BCG cell, we propose a DEP experiment method to use f_{xo1} in combination with σ_m. Upon heat- or drug treatments, $C_{envelope}$ and σ_{cyto} are expected to decrease, which can be observed in the inset of Fig. 16C. The ranges of applied f and σ_m are 1~20 MHz and of 0.05~0.3 S/m, respectively.

In the proposed ranges of f and σ_m, two parameters of $C_{envelope}$ and σ_{cyto} are estimated to examine drug effects. Fig. 16D shows the shift of σ_m-f_{xo} line in the graph, which is also the inset in Fig. 16C. The blue line is the σ_m-f_{xo1} line for a control cell. A nonlinear increase of f_{xo1} with respect to σ_m indicates the transition of sensitive cell property from $C_{envelope}$ to σ_{cyto}. When either σ_{cyto} or $C_{envelope}$ decreased, the line of σ_m-f_{xo1} was changed to the green- or red lines, respectively. In the experiment, we measure the change of σ_m-f_{xo1} for the control and drug-treated cells. Using the measured data of σ_m-f_{xo1}, the changes of $C_{envelope}$ and σ_{cyto} are estimated for quantification.

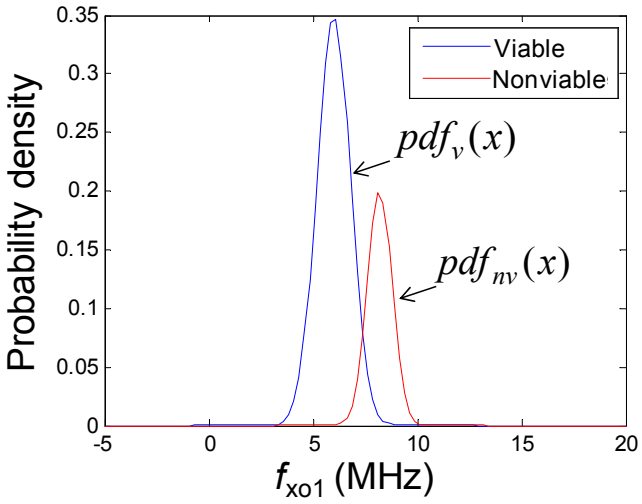

Figure 17 Probability density function (PDF) of f_{xo1} for the approximation model.

Since discrete values of f_{xo1} at various σ_m are measured in experiment, a statistical modeling is used to estimate the distribution of f_{xo1}. In the modeling, it is assumed that a batch of cells is divided into viable- and nonviable groups in the contexts of DEP. According to the two-group assumption, two average values of f_{xo1} with variation are present. The normal distribution for both cell groups is approximated with an average (M_i) and a standard deviation (SD_i) by using a probability density function (PDF):

$$pdf_i(x) = \phi_i \times \frac{1}{(SD_i)\sqrt{2\pi}} e^{-\frac{(x-M_i)^2}{2(SD_i)^2}}, \quad i = v, nv \tag{4.2}$$

where ϕ_v and ϕ_{nv} indicate the fractions of viable- and nonviable cells in a batch ($\phi_v+\phi_{nv}=1$). Figure 17 shows an example of two PDFs for viable- and nonviable cells that coexist in a batch.

Figure 18 shows the analysis procedure of this study. Firstly, cells are captured on electrodes. By discrete decreases of the frequency from 20 to 1MHz, the frequency repelling the captured cells is identified. Since the captured cells are

repelled at the frequency by nDEP, f_{xo1} exists between the frequency and the previous frequency. The number of the repelled cells is normalized by dividing the number of cells at each frequency by the total number of cells. A PDF model is used to estimate a continuous distribution of f_{xo1} from the discrete data of experiment. The parameters of PDF model, ϕ_i, M_i, and SD_i, are extracted by using a least square method. Using the parameters, the f_{xo1} distribution of viable- and nonviable cells is extracted as shown in Fig. 17. With the f_{xo1}, the properties of $C_{enevelope}$ and σ_{cyto} for control, heat-killed, RIF-treated, and INH-treated cells are estimated by using a sampling algorithm. In the algorithm, various cells having different properties are sampled. Among the sampled cells, the cells having f_{xo1} in the ranges of the distribution estimated from the PDF model are selected. Then, the change of BCG cell due to a treatment is estimated in terms of property distribution of $C_{enevelope}$ and σ_{cyto}.

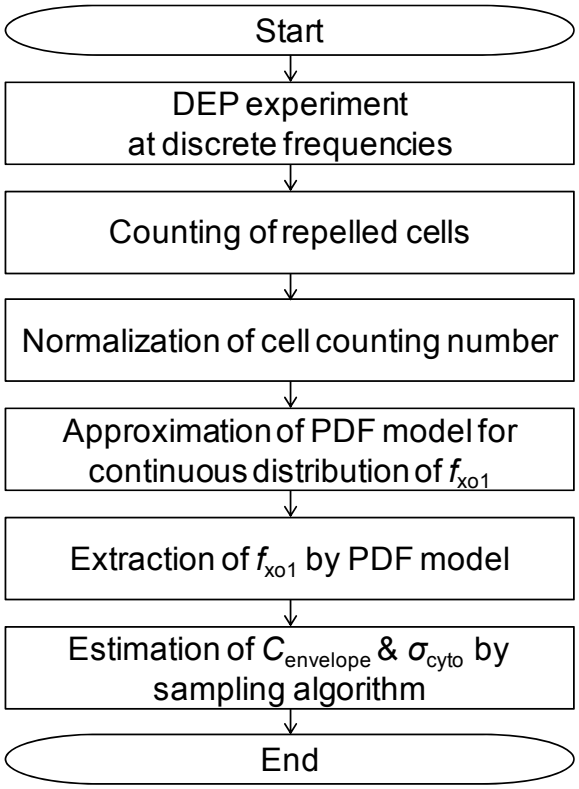

Figure 18 Flow chart for DEP characterization of antibiotic-treated BCG cells.

4.3 Experimental method

4.3.1 Planar electrode fabrication

Electrodes were fabricated in the Washington Nanofabrication Facility, University of Washington. Thermal oxidation was conducted to grow a 300 nm-thick oxide layer on a silicon wafer. A 30nm-thick gold film was then evaporated onto the surface using electron beam evaporator. Subsequently, rectangular electrodes with the gap size of 10 μm and the width of 50 μm were patterned by using photolithography and metal etching.

4.3.2 Cell culture and preparation

A stock solution of log-phase BCG cell suspension of 10^8 CFU/mL was aliquoted into three 10 mL cultures in Difco Middlebrook 7H9 Broth (BD Diagnostics, Sparks, MD) supplemented with 10% (v/v) ADC enrichment and 0.05% Tween 20. The three cultures were designated for control, RIF-treated, and INH-treated samples. Antibiotics (RIF or INH at 1 μg/mL) were added as appropriate. The cells were cultivated on a shaker at 37°C for 4 days after addition of the drug. Heat-killed BCG cells were prepared by submerging 500 μL of control cells in a heat bath at a lethal temperature of 85°C for 30 minutes immediately prior to DEP experiment. To confirm and quantify inactivation, cells suspended in 500 μL samples were stained with Live/Dead *Bac*light dye (Invitrogen, Carlsgad, CA). The stained samples were incubated at room temperature for 15 minutes prior to microscopic examination.

4.3.2 DEP experiment

The electrodes were connected to a function generator (Agilent 33220A, Santa Clara, CA) with an applied voltage of 20 V_{pp}. Upon placement of 5μL sample on the electrodes, the applied frequency was slowly increased to 1, 2, 4, 5, 6, 8, 10, and 20 MHz in 10 second intervals. As the frequencies increased, the cells in a solution drop were attracted to and collected on the electrodes. Subsequently, the applied frequency was decreased in the reverse order to determine when the attracted cells detached from the electrode edge. The number of the repelled cells was counted at each frequency. In a batch, cells were repelled at multiple frequencies due to the physiological heterogeneity of the cells. The frequency test was repeated for various medium conductivities including σ_m=0.07, 0.11, 0.16, 0.21, and 0.26 S/m. The conductivity was measured using a conductivity meter (Thermo Scientific, MA). The various media were prepared by diluting the cultured stock with deionized (DI) water (10%, 20%, 30%, 40%, and 50% 7H9, respectively). All experiments were repeated three times. For observation of cell movement, a fluorescence microscope (Nikon Eclipse 55i) was used as shown in Fig. 16A.

4.4 Results and Discussion

The variation of f_{xo1} for a BCG cell batch was observed through fluorescence microscopy. The transition from pDEP to nDEP was detected by observing the repelling motion of cells from an electrode. Figure 19 shows the change of the cell motion according to the frequency sweep. When the frequency increased from 1 to 20 MHz, the non-treated BCG cells were initially concentrated at the electrode gap by pDEP in the medium of 10% 7H9 broth (σ_m=0.07 S/m). To find f_{xo1}, the frequency of the input voltage was decreased from 20 to 10, 8, 6, 5, 4, 2, and 1 MHz. The control cells at the electrode edge remained until 4 MHz (Fig. 19A). At 2 MHz, a group of cells (in red circles) were repelled from the gap by nDEP (Fig. 19B). The number of cells repelled at this frequency was 23. By further reducing the frequency to 1 MHz, the second group of 30 cells (in green circles) was repelled from the electrode (Fig. 19C). These procedures were repeated for control, heat-killed, INH-treated and RIF treated BCG cells for the various medium conductivities, σ_m=0.07, 0.11, 0.16, and 0.21 S/m.

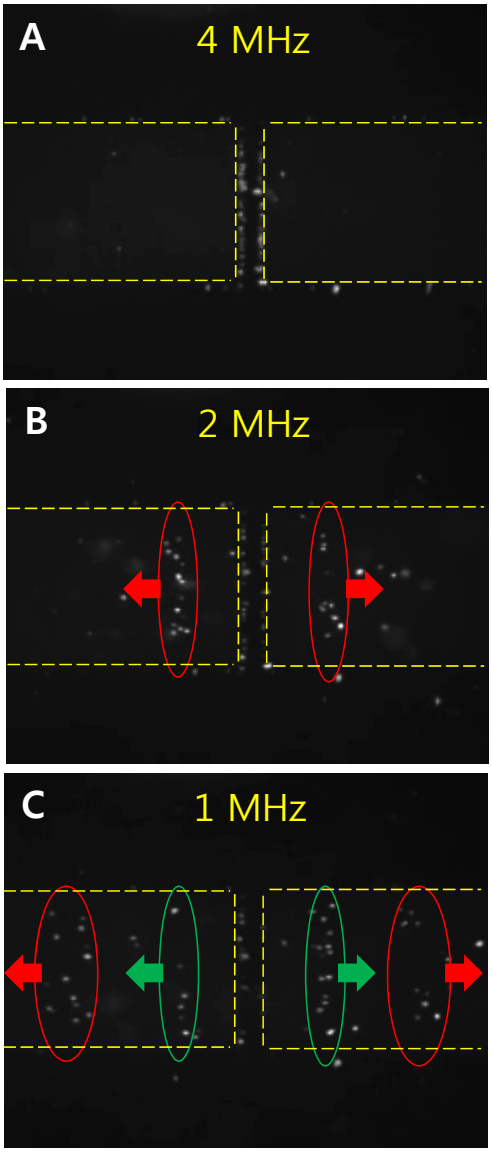

Figure 19 Movement of control BCG cells on planar electrodes at 4, 2 and 1 MHz (σ_m=0.07 S/m). Electrode edges are indicated by the yellow dashed lines. A: Cells are concentrated on the electrode edge by pDEP. B, C: Cells are repelled from the electrodes due to the transition of pDEP to nDEP at 2 and 1 MHz, respectively. Experiment was done by *S. Inoue*.

In Fig. 20, the normalized number of the repelled cells at each frequency is indicated as red circles according to various σ_m. In each graph, the PDFs of f_{xo1} are shown by blue- and red colors, corresponding to viable- and nonviable groups. The PDF parameters of ϕ_i, M_i and SD_i were estimated for the f_{xo1} distributions of viable- and nonviable cells, $(f_{xo1})_v$ and $(f_{xo1})_{nv}$. For the cells treated with heat, INH, and RIF, only $(f_{xo1})_{nv}$ was estimated while $(f_{xo1})_v$ was set as the same values of the control at each σ_m. To validate the statistical model, the normalized numbers of cells computed from the model (*) were compared to experimental results (o), which agreed well.

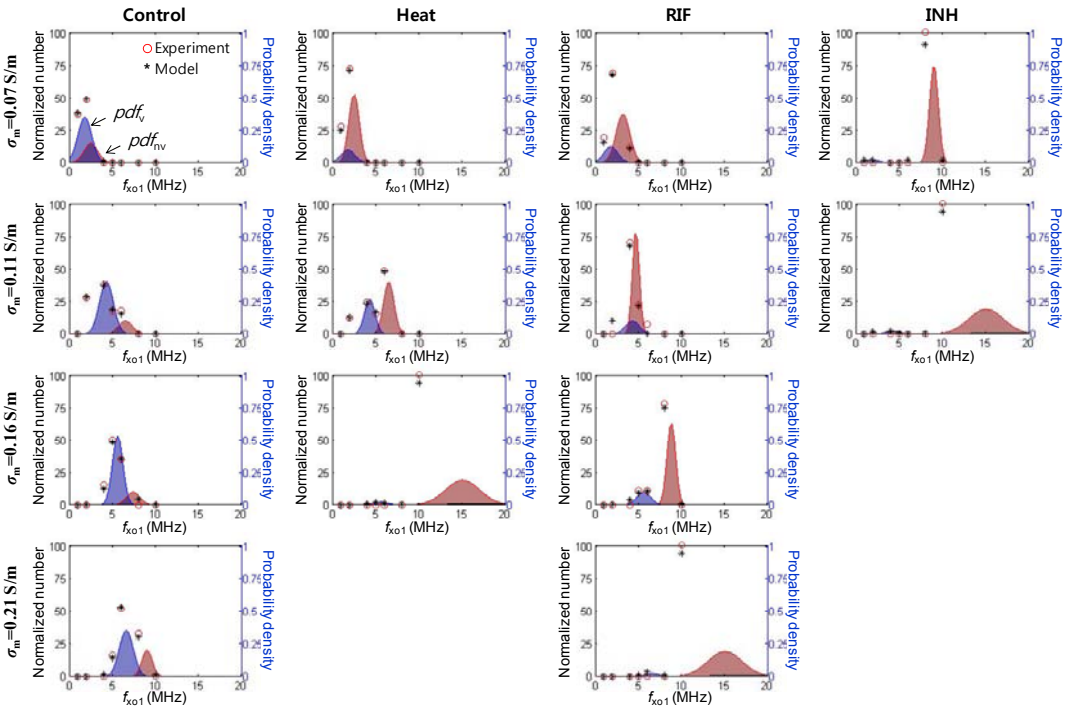

Figure 20 Normalized number of cells at different frequencies measured from the experiment (o) and computed from the model (*) (y-axis on left). Probability density functions of f_{xo1} for viable (blue) and nonviable cells (red) for non-treated (Control), heat-killed (Heat), RIF-treated (RIF), and INH-treated (INH) cells in the medium conductivity of 0.07, 0.11, 0.16, and 0.21 S/m (y-axis on right).

For the control at σ_m of 0.07 S/m, $(f_{xo1})_v$ and $(f_{xo1})_{nv}$ for viable- and nonviable cells were 2.0 and 1.0 MHz, respectively. As the conductivity increases, both $(f_{xo1})_v$ and $(f_{xo1})_{nv}$ increase. Heat-killed cells show a noticeable difference between $(f_{xo1})_v$ and $(f_{xo1})_{nv}$ as σ_m increases. Regarding σ_m of 0.21 S/m, a graph does not exist for heat-treated cells because of nDEP in the given frequencies. RIF-treated cells show a clear distinction for $\sigma_m \geq 0.16$ S/m. For INH-treated cells, only a few cells were observed in experiment for the given σ_m. In case of σ_m=0.16 and 0.21 S/m, cells were not attracted due to absence of pDEP in the experimental ranges of f and σ_m.

In Fig. 21A, the $(f_{xo1})_v$ of the control cell and the $(f_{xo1})_{nv}$ of the cells treated with heat, INH and RIF are shown according to σ_m. In the graph, the symbols and the error bars indicate M_i and SD_i from the PDF model. Both $(f_{xo1})_v$ and $(f_{xo1})_{nv}$ are clearly differentiated for each cell. Using $(f_{xo1})_v$ and $(f_{xo1})_{nv}$ at the conductivities, the parameters of $C_{envelope}$ and σ_{cyto} were estimated by the sampling algorithm (Fig. 21B). For the control group, $C_{envelope}$ and σ_{cyto} were in the range of 3.7~4.5 F/m^2 (Mean: 4.07; Stdev: 0.20) and 0.6~1.0 S/m (Mean: 0.85; Stdev: 0.10), respectively. Heat-killed cells showed about 50% decrease in both $C_{envelope}$ and σ_{cyto} in terms of a mean value. RIF-treated cell showed a smaller decrease on both $C_{envelope}$ (45%) and σ_{cyto} (27%) in comparison to the heat-killed cells. The decrease could result from the cell ceasing to function, reducing the amount of ions and charged particles produced in the cytoplasm. The $C_{envelope}$ of INH-treated cell was greatly reduced by 78% in comparison to that of the control cells. The result was consistent with the assumption that INH affects the $C_{envelope}$ through inhibition of

mycolic acid synthesis, producing a very noticeable effect on DEP. The average values of $C_{envelope}$ and σ_{cyto} are summarized in Table 5.

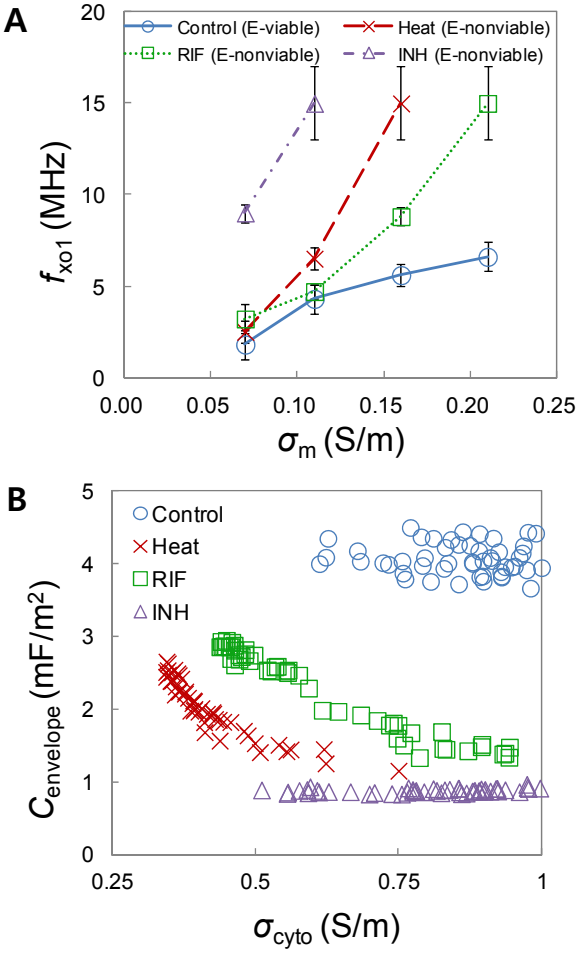

Figure 21 A: Extracted f_{xo1} from the model for control (E-viable), heat-killed (E-nonviable), RIF-treated (E-nonviable), and INH-treated (E-nonviable) BCG cells. B: Estimated $C_{envelope}$ and σ_{cyto} for BCG cells having f_{xo1} indicated in Fig. 21A

Table 5 Estimation of cell properties. The values in the parenthesis shows the percent decrease of the cell parameters in comparison to the control cells.

Sample	Control	Heat-killed	RIF	INH
$C_{\text{envelope}}\,(\text{mF/m}^2)$	4.07	2.03 (50.1%)	2.25 (44.7%)	0.88 (78.4%)
$\sigma_{\text{cyto}}\,(\text{S/m})$	0.85	0.42 (50.6%)	0.62 (27.1%)	0.80 (5.9%)

Fig. 22 shows the SEM images of the control, heat-killed, RIF-treated, and INH-treated cells. In comparison to the control in Fig. 22A, the heat-killed cell in Fig. 22B appeared flat because the ruptured cells were left without a cytoplasm. Other cells were swollen with a depreciated ring around the cell. The depreciated ring showed that cell envelope could lose the structural integrity at the lethal temperatures and could not retain the shape in the vacuum chamber of SEM. The width of the ring was 60 nm, which was consistent with the cryo-electron images of *Mycobacterium* consisting of a 50 nm thick cell wall and 10 nm-thick membrane [90]. The SEM image showed that heat-treatment could greatly change the wall and membrane structure of a cell, and thus, the specific capacitance of the outer shell structure. The morphological change was consistent with the experimental results showing the reduction of $C_{envelope}$ and σ_{cyto}.

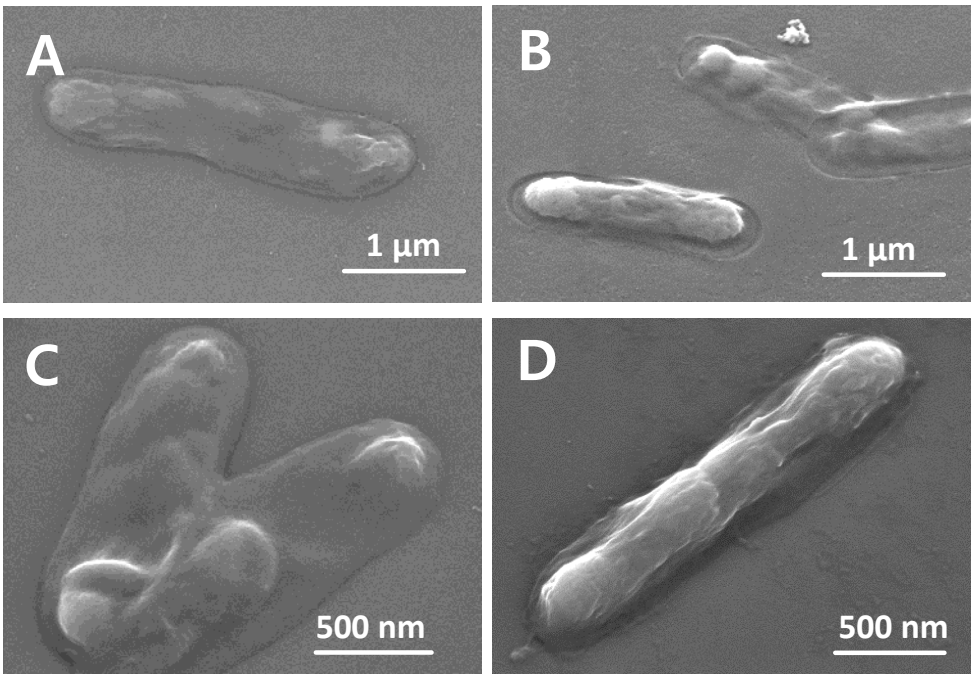

Figure 22 SEM images of *M. bovis* BCG cells after 4 days of culture. A: Un-treated control BCG cell. B: control BCG cells after being heat-killed at 85°C for 30 minutes. C: RIF-treated BCG cells. D: INH-treated BCG cell. Experiment was done by *S. Inoue*.

The SEM images of RIF-treated BCG cells showed very smooth surface with some blebbing-like structure (Fig. 22C). The INH-treated cells were very swollen with surface deformations (Fig. 22D). The rings around the INH-treated cell were consistent with the results from heat-killed cells, where the distance matched the thickness of cell wall and membrane [90]. The additional images are given in the supplementary material.

Previous research has shown that heat-treatment could have similar effects on INH, where heat-treatment of *M. smegmatis* inactivated the temperature-sensitive *inhA* gene [91]. The morphological changes were consistent with the DEP results. The conductivity of a cell's interior was high due to the ions and charged particles stored in the cytoplasm. Once the envelope became more permeable, water might have flowed into the cell, which would reduce the conductivity. The speculation was consistent with the SEM image showing bloated BCG cells. The cells could have lysed, which would result in the cytoplasm escaping the cells. In the SEM images, the BCG cells were nearly empty.

4.5 Summary

In summary, we studied dielectrophoretic behavior of *Mycobacterium bovis* in response to heat-killing and drug treatment of rifampin and isoniazid, which was the first case of DEP study for *Mycobacterium tuberculosis* complex cells. The experimental conditions using frequencies below 20 MHz with the mid-range σ_m of 0.05~0.3 S/m were proposed to detect the drug effect in conjunction with the numerical method. DEP measurements showed that both heat-killing and isoniazid significantly changed the capacitance of the cell envelope. The result was consistent with the drug mechanism of isoniazid inhibiting synthesis of the cell wall structure and temperature affecting the cell envelope. Also, rifampin could be differentiated by DEP that detected the property change in the interior of a cell. Using a statistical model, the decreases of capacitance of the cell wall and the cytoplasm conductivity were estimated for heat-, RIF- and INH treatments. The drug mechanism was compared with the decreases of both parameters. With further development, DEP can be exploited to evaluate for drug-susceptibility of *Mycobacterium tuberculosis* complex cells.

Chapter 5: Electrokinetic separation of heat-treated *Mycobacterium* BCG cells

5.1 Background

The separation of bioparticles is essential for developing bioassays and point-of-care diagnostic devices. Centrifugation in combination with microfiltration can be used for separation of bioparticles depending on the relative mass [92]. Magnetic particles decorated with probe molecules are used to separate target particles in sample matrix [93]. Microfluidic devices are often employed for bioparticle separation for rapid biosensors [94-97]. Dielectrophoretic (DEP) techniques, in particular, have been popular for microfluidic devices [22, 76, 77, 98].

One of the great advantages of DEP is the capability to separate particles depending on the physical- and electrical properties. DEP has been utilized to characterize and separate various biological particles such as bacterial populations [62, 99], mammalian cells [100, 101], DNA [102, 103], and proteins [104]. DEP force is proportional to the cube of particle radius ($F_{DEP} \sim r^3$). As the radius of a cell decreases from 10 μm to 1 μm, DEP force is significantly reduced and becomes comparable to electrohydrodynamic forces that are proportional to the particle radius ($F_{EHD} \sim r$). Therefore, the separation of bacterial cells using DEP is challenging without consideration of electrohydrodynmics.

Electroosmosis (EO) is an electrohydrodynamic phenomenon caused by the charge interaction in electrical double layer under an electric field, resulting in a fluid flow over the electrode surface. Electroosmosis from AC electric field (ACEO) has been used for mixing in microchannels [105, 106] and transport [107-

109] of submicron particles. ACEO is effective within a medium of high ionic concentration with high medium conductivity (σ_m > 1 S/m). To reduce the interference of ACEO to DEP separation, σ_m needs to be decreased. However, the use of low conductive medium ($\sigma_m < 10^{-3}$ S/m) can affect the integrity of cells and the sample preparation. To obtain the low conductivity, biosamples need to be diluted or replaced with deionized (DI) water. The process is cumbersome and may not be compatible with fragile bioparticles.

A semi-conductive medium can take advantages of both low- and high conductivity buffers. It can be easily prepared while bacterial cells can be effectively separated by DEP. However, the system is still complex because DEP is augmented with ACEO. To achieve an efficient separation of bacterial cells, the combined effect of DEP and ACEO should be understood.

In this study, a numerical and experimental study is conducted to investigate the combined effects of DEP and ACEO using a medium of 0.07 S/m. *Mycobacterium bovis* BCG cells are used as a target model. As a surrogate marker for *Mycobacterium tuberculosis* (MTB) cells, the understanding of the electrokinetic behavior of viable- and nonviable BCG cells can potentially envision the application of DEP for drug-resistance tests. In our study, *Mycobacterium bovis* BCG cells with heat-treatment are used to study the electrokinetic behavior. An optimized condition for electrokinetic separation is suggested to differentiate control- and heat-treated BCG cells. The parameters of control- and heat-killed BCG cells are estimated. The study can be potentially applied to discover a simple and inexpensive method for testing drug susceptibility. It should be noted that the experiment in this chapter was conducted by Dr. Shin Inoue.

5.2 Theory

An electrohydrodynamic force can be induced by two different mechanisms. One is electroosmosis that is caused by ion movement in liquid. If an electric potential is applied to electrodes, an electrical double layer (EDL) is formed onto the electrode surface. The first layer of EDL, Stern layer, consists of opposite charged ions to electrode charge, and the ions in this layer are fixed on the surface of the electrode. The ions in the second layer, called as diffuse layer, are loosely anchored to the surface due to the screening effect of the first layer. In the diffuse layer, ions can move in a tangential direction of the electrode surface by Coulomb force. The ion movement can induce fluid flow called as electroosmosis (EO). The speeds of electroosmotic flow for a DC field (DCEO) and an AC field (ACEO) can be computed by:

$$U_{DCEO} = -\frac{\varepsilon_m \zeta E_t}{\mu} \tag{5.1}$$

$$U_{ACEO} = \Lambda \frac{\pi \varepsilon_m V_o^{\,2}}{8\mu x} \frac{\Omega^2}{\left(1+\Omega^2\right)^2} \tag{5.2}$$

where μ is the viscosity of solution, E_t is the tangential directional electric field on the surface of electrode, Λ is the relative capacitance of the stern layer with respect to overall double layer ($\Lambda = C_S/(C_S+C_D)$, C_S: the capacitance of Stern layer, C_D: the capacitance of Diffuse layer), V_0 is the input voltage, x is the characteristic length (i.e. a half length of electrode gap), and Ω is the non-dimensional frequency that is defined as:

$$\Omega = \frac{\pi \varepsilon_m \omega x}{2\sigma_m \lambda_D} \tag{5.3}$$

where ω is the angular frequency of input voltage, and σ_m is the conductivity of the medium.

Electrothermal flow (ETF) is caused by Joule heating that changes the electric properties of medium. Subsequently, the body force is generated on the fluid. This body force is used as an external force term in the Navier-Stokes equation to compute ETF. The ETF force can be computed by:

$$\mathbf{F}_{ETF} = \frac{1}{2}\mathrm{Re}\left[\frac{\sigma_m \varepsilon_m (\alpha - \beta)}{\sigma_m + i\omega\varepsilon_m}(\nabla T \cdot \mathbf{E})\mathbf{E}^* - \frac{1}{2}\varepsilon_m \alpha |\mathbf{E}|\nabla T\right] \tag{5.4}$$

where T is the temperature α and β are defined as $\alpha=(1/\varepsilon_m)(\partial\varepsilon_m/\partial T)$ and $\beta=(1/\sigma_m)(\partial\sigma_m/\partial T)$, respectively. The first term in the right hand side of Eq. (5.4) is the Coulomb force that is dominant at low frequencies, and the second term is the dielectric force that is dominant at high frequencies.

In this study, electrosomosis is only considered as an electrohydrodynmic effect. Since the speed of electroosmosis (10~1,000 μm/s) is orders of magnitude higher than that of electrothermal flow (~10 μm/s), the effect of electrothermal flow is neglected.

Brownian motion should be considered for small size particle to understand the movement of particle in a solution. Brownian force is computed as follow:

$$\mathbf{F}_B = \zeta\sqrt{\frac{12\pi\mu r k_B T}{\Delta t}} \tag{5.5}$$

where k_B is the Boltzmann constant, t is the time, and ζ is the normally distributed random variable with the mean of 0 and the variance of 1.

When only drag force and Brownian force are present, the Brownian motion of particle in a solution can be derived as:

$$\mathbf{F}_N = \mathbf{F}_D + \mathbf{F}_B \tag{5.6}$$

$$0 = -6\pi\mu r\left(\frac{\Delta \mathbf{x}}{\Delta t} - \mathbf{u}\right) + \mathbf{F}_B$$

(5.7)

$$\left|\Delta \mathbf{x}\right| = \zeta\sqrt{\frac{2k_B T}{6\pi\mu r}\Delta t} \tag{5.8}$$

where $\mathbf{F}_N$ is the net force, $\mathbf{F}_D$ is the drag force that is from the relative motion of particle to fluid flow. In Eq. (5.6), the net force assumed as zero because the inertia of particle can be neglected. The fluid velocity set to zero to compute Brownian motion of particle in Eq. (5.7).

In this study, the Brownian motion is not considered due to its small displacement. For a cell with 1-μm radius, the displacement by Brownian motion is 6.5 μm for 100 seconds (0.065 μm/s), which is negligible in comparison to the displacements by dielectrophoresis or electroosmosis near an electrode. In the vicinity of electrode edge, 1-μm radius cell can move with a speed of ~1 mm/s by dielectrophoresis or electroosmosis. Since our interest is to investigate the cell behavior near electrode, Brownian motion can be neglected.

5.3 Numerical approach

To analyze electrokinetic behavior of BCG cells in experiment, a numerical simulation was conducted to analyze the electrokinetic forces on a cell under DEP and ACEO. To solve the electrokinetics of a cell, the electric- and flow fields are computed by using COMSOL multiphysics®. Subsequently, the electrokinetic motion of a cell in three dimensions is analyzed by a post--processing program written in C.

Fig. 23A shows the analysis domains with boundary conditions. In the whole domain illustrated by the solid lines, the electric- and flow fields were computed by solving Poisson- and Stokes equations, respectively. For an electric field, the electric potentials of V (7.07 V) and ground (0 V) were applied on the electrodes. After solving the electric field, the flow field was solved to simulate ACEO flow. Since the ACEO flow was a function of frequency, the problem was simplified by an analytical equation of DC electroosmosis (DCEO) multiplied with a scaling factor of S_{ACEO} [110]:

$$\mathbf{u}_{ACEO}=S_{ACEO}\mathbf{u}_{DCEO} \tag{5.9}$$

$$\mathbf{u}_{DCEO}=\frac{\varepsilon_m \zeta}{\mu}\mathbf{E}_t \tag{5.10}$$

where ε_m is the permittivity of the medium, ζ is the zeta potential, μ is the viscosity of the medium, and $\mathbf{E}_t$ is the tangential electric field. Then, the magnitude of the flow velocity was calibrated by S_{ACEO} according to our experimental measurement. The flow speed computed by the analytical equation has shown a discrepancy in comparison to experimental measurement [111]. Therefore calibration is needed to simulate the electrokinetic motion of cells by ACEO.

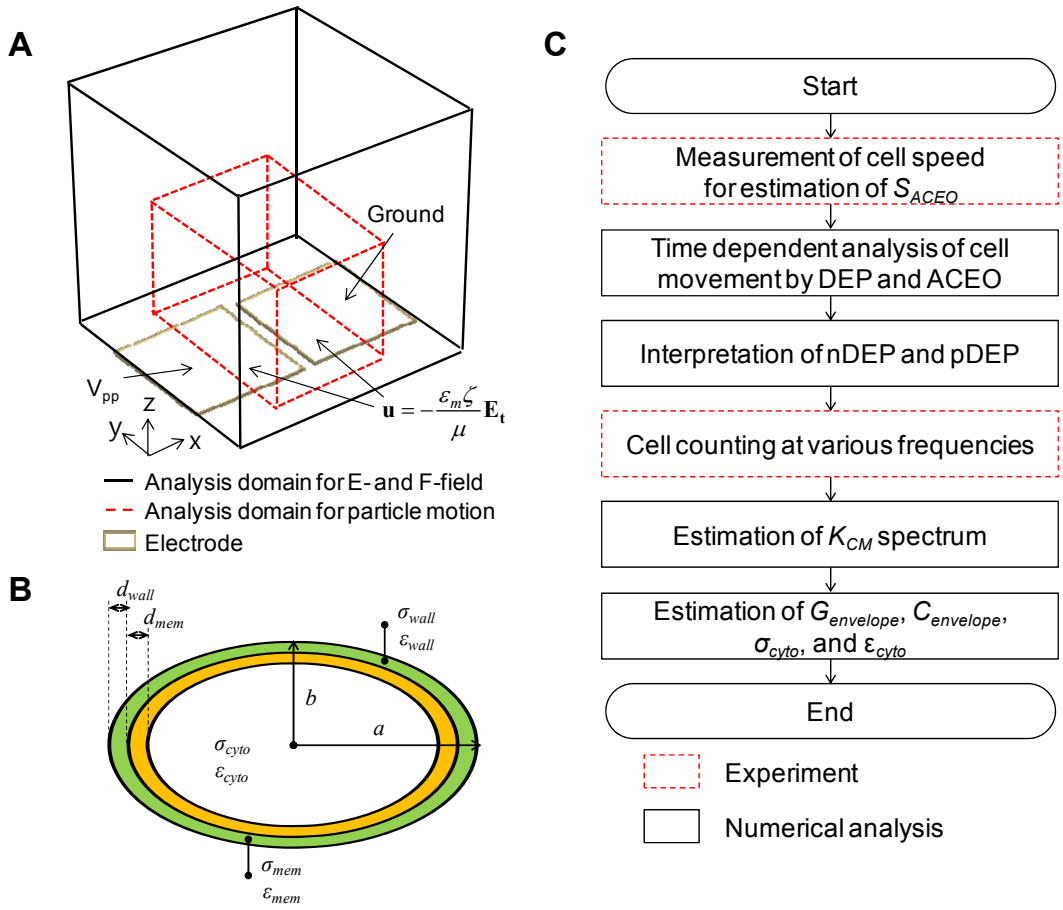

Figure 23 A: Analysis domain with boundary conditions. The analysis domain for electric- and fluid field is indicated with black solid lines. The analysis domain for particle motion is the box with red dashed lines. The electrodes are colored by orange pads. B: Double-shell ellipsoidal model of a cell with a membrane (mem) and wall. The parameters are the thickness of d, the conductivity of σ, and the permittivity of ε. C: Analysis procedure to study the electrokinetic behavior of cells and the parameters.

The cell motion by DEP and ACEO was solved in the analysis domain indicated by the red dashed line in Fig. 23A. To reduce the computational cost in three-dimensional space, the domain was reduced to the region near the gap of two electrodes. The dimensions of the domain were 80, 160, and 50 μm in *x*-, *y*-, and *z*-axes, respectively. The net force for a non-charged particle in a medium under an electric field is represented by the following equation:

$$\mathbf{F}_{net} = \mathbf{F}_{drag} + \mathbf{F}_{DEP} \tag{5.11}$$

where $\mathbf{F}_{drag}$ and $\mathbf{F}_{DEP}$ are the drag force and the DEP force, respectively. Brownian motion-induced force is not considered because of the negligible force for micronsize cells [112].

The drag force is from the relative motion of an ellipsoidal particle under the flow:

$$\mathbf{F}_{drag} = -6\pi\mu\, r_{eff} \left(\mathbf{v}_p - \mathbf{u}_{ACEO}\right)K \tag{5.12}$$

where μ is the viscosity, r_{eff} is the effective radius of particle ($r^3=ab^2$, a: the half length of a long axis; b: the half length of a short axis), $\mathbf{v}_p$ is the particle velocity and K is the resistance coefficient for ellipsoidal particle [113]:

$$K = \frac{8}{3a}\frac{a^2-b^2}{(2a^2-b^2)S-2a} \tag{5.13}$$

where

$$S = \frac{2}{\sqrt{a^2-b^2}}\ln\frac{a+\sqrt{a^2-b^2}}{b} \tag{5.14}$$

The DEP force for an ellipsoidal particle is computed by [114]:

$$\mathbf{F}_{DEP} = 4\pi ab^2\varepsilon_m \,\mathrm{Re}\left[K_{CM}\right]\nabla\left|\mathbf{E}\right|^2 \tag{5.15}$$

The polarizability factor of K_{CM} is the Clausius-Mossotti (CM) factor, which depends on the applied frequency of an electric field and the relative difference of the electric properties between a medium and a suspended particle.

Equations (5.9) ~ (5.15) were combined to analyze the electrokinetic motion of a bacterial cell with $\mathbf{F}_{net} = 0$:

$$\Delta x = \left(\mathbf{u}_{ACEO} + \frac{2b^2\varepsilon_m}{3\mu K}\mathrm{Re}\left[K_{CM}\right]\nabla\left|\mathbf{E}\right|^2\right)\Delta t \tag{5.16}$$

where Δx is the particle displacement, and Δt is the time step. Acceleration is not considered because the time to reach a terminal velocity is smaller than Δt of the simulation by several orders of magnitude. Assuming that a particle has the radius of 1 μm with a density of 1,000 kg/m^3, and the velocity linearly increases from 0 to 100 μm/s upon the force of 1 pN, the required time to the terminal velocity is 0.4 μ-seconds. In comparison to Δt of 5 m-seconds, the required time is higher by 4 orders of magnitude, which shows that the acceleration can be 0 m/sec^2.

In the numerical computation, the electrokinetic motion of 100 cells was simulated. Initially, the cells were randomly positioned in the analysis domain. Then, the cell position was updated by solving equation (5.16) for 10,000 iterations. To investigate the combined effects of DEP and ACEO, K_{CM} for DEP and S_{ACEO} for ACEO were manipulated in the range of -0.5 ~ 0.5, and 0 ~ 1 (S_{ACEO} =1 for 500 um/s), respectively.

To estimate the change of cell properties upon heat treatment, a double-shell ellipsoidal model [115] was used for a BCG cell composed of cell membrane, wall and cytoplasm (Fig. 23B). The medium, the cytoplasm, and the membrane are denoted by *m*, *cyto*, and *mem*, respectively. d_{wall} and d_{mem} are the wall- and the membrane thicknesses, respectively. Based on our SEM study, *a* and *b* were 1 μm and 0.25 μm, respectively. According to the reference [91], d_{wall} was 40 nm and d_{mem} was 10 nm. Note that the thickness of 50 nm was measured for the cell envelope (wall + membrane) using the cryo-electron microscopy.

For the wall, membrane and cytoplasm of a cell, two properties of the conductivity (σ) and the permittivity (ε) are used as σ_{wall}-ε_{wall}, σ_{mem}-ε_{mem}, and σ_{cyto}-ε_{cyto}, respectively. To simplify the analysis, the properties for the cell wall and the

membrane were combined into two parameters of conductance ($G_{envelope}$) and capacitance ($C_{envelope}$) of the envelope:

$$G_{envelope} = \frac{\sigma_{wall}\sigma_{mem}}{\sigma_{mem}d_{wall} + \sigma_{wall}d_{mem}} \tag{5.17}$$

$$C_{envelope} = \frac{\varepsilon_{wall}\sigma_{mem}}{\varepsilon_{mem}d_{wall} + \varepsilon_{wall}d_{mem}} \tag{5.18}$$

The analysis procedure is summarized in Fig. 23C. The particle speed of BCG cell was initially measured in experiment to estimate S_{ACEO} for modeling of ACEO. To understand the behavior of a cell, time-dependent analysis of cell movement was conducted by considering DEP and ACEO. In the complex motion of cells, we would evaluate if the cell motion was resulted from a positive- (pDEP) or negative DEP (nDEP). Subsequently, the cells captured on the electrode edge were counted at various frequencies from 1 kHz to 10 MHz. The K_{CM} spectra of control and heat-killed BCG cells were estimated. Finally, the heat effect on viability of BCG cells was analyzed in terms of the cell parameters of $G_{envelope}$, $C_{envelope}$, σ_{cyto}, and ε_{cyto} with the aid of the numerical analysis.

5.4 Materials and Methods

5.4.1 Planar electrode fabrication

Planar electrodes (Fig. 24A) were fabricated in microfabrication laboratory (Washington Nanofabrication Facility, University of Washington). Thermal oxidation was used to grow a 300 nm-thick oxide layer on the silicon wafer. Gold layers (30 nm) were then evaporated onto the surface using an electron beam evaporator. Electrodes with gap size of 10 μm were patterned onto the silicon wafer using conventional photolithography and etching.

5.4.2 BCG culture

BCG used in this study was cultivated in a shaker at 37°C. BCG cells were cultured in Difco Middlebrook 7H9 Broth (BD Diagnostics, Sparks, MD) supplemented with 10% (v/v) ADC enrichment and 0.05% Tween 20.

5.4.3 Cell preparation

BCG cell suspension of 100 μL (concentration: 10^8 CFU/mL) in 7H9 culture broth was diluted 1:10 in deionized water (DI) to obtain 1 mL of 10^7 CFU/mL. The medium conductivity (σ_m) was 0.07 S/m. Heat-treatment of cells was conducted by submerging the vials in a heated water bath for 10 minutes. To study the temperature effect on BCG, the temperature of water bath was controlled from 50 ºC to 80 ºC by 10 ºC increments. To obtain heat-killed cells, 500 μL of control cells were exposed to a higher temperature of 85 ºC for 30 minutes. The cells were stained with Live/Dead *Bac*light kit (Invitrogen, Carlsgad, CA) for staining and left at room temperature for 15 minutes prior to experiment.

5.4.4 Experimental setup for electrokinetic measurement

A planar gold electrode with a gap length of 10 μm was used to characterize the electrokinetic responses of BCG cells. The electrodes were connected to a function generator (Agilent 33220A, Santa Clara, CA) with frequencies of 1 kHz, 10 kHz, 100 kHz, 1 MHz, 5 MHz, and 10 MHz. for 1 minute. The peak-to-peak voltage (V_{pp}) of 20 V was applied, when the frequency was greater than 10 kHz. When the frequencies were 1 kHz and 10 kHz, 6 V_{pp} and 12 V_{pp} were applied, respectively. At both frequencies, the voltages were reduced to prevent electrolysis in the solution. The cell behavior was imaged for 1 minute using a fluorescent microscope (Nikon Eclipse 55i). The setup is illustrated in Fig. 24B.

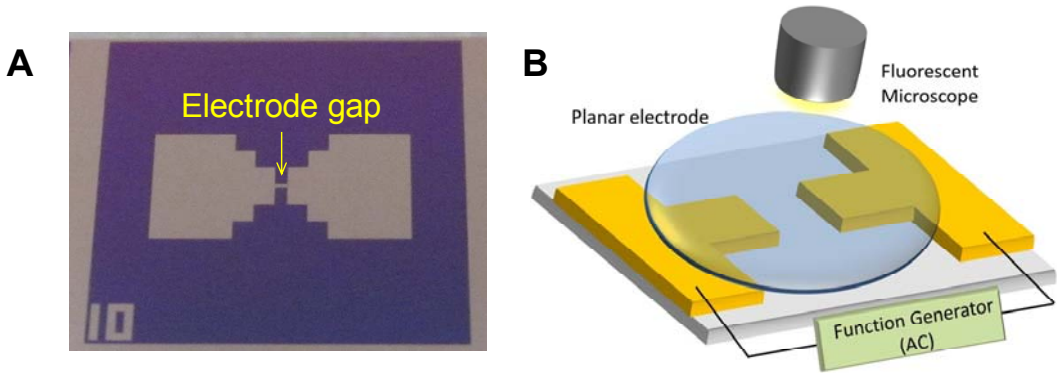

Figure 24 A: Fabricated planar electrode with a gap size of 10 μm. B: Illustration of experimental setup.

5.5 Results and Discussion

Electrokinetic responses of stained BCG cells were investigated for various frequencies. Both cell suspensions of control- and heat-killed cells were exposed to the frequencies of 1 kHz ~ 10 MHz on a planar electrode for a period of 1 minute (Fig. 25). Frequencies below 1 kHz were not evaluated because the electrodes were damaged. The frequencies greater than 10 MHz were not evaluated because ACEO flow disappeared. Without ACEO, the BCG cells were hardly attracted to the electrodes, which made the system impractical as a sensor.

Frequency of 1, 10, and 100 kHz showed a noticeable trend for both control and heat-killed cells. As the frequency increased from 1 to 100 kHz, the speed of the cells gradually increased and was the highest near the electrode edge. At the attraction between electrodes by ACEO, the cells were circulated around the edge and progressively moving toward the center of the electrode. The blurred image of cells was resulted from the out-of-focus of the cells from the electrode surface.

Beginning from 1 MHz, the rotation of cells was no longer visible because the cells glided across the electrode surface and did not return into the suspension. With decrease in velocity, cells began to be immobilized between the electrode gaps. However, the attracted cells were back and forth in the gap without complete immobilization. In particular, this effect was more noticeable for heat killed cells. At 5 MHz, the largest number of cells were captured at the edges of the electrodes for both control and heat-killed BCG cells. At 10 MHz, with negligible fluid flow, only the BCG cells in the vicinity of the edge were captured.

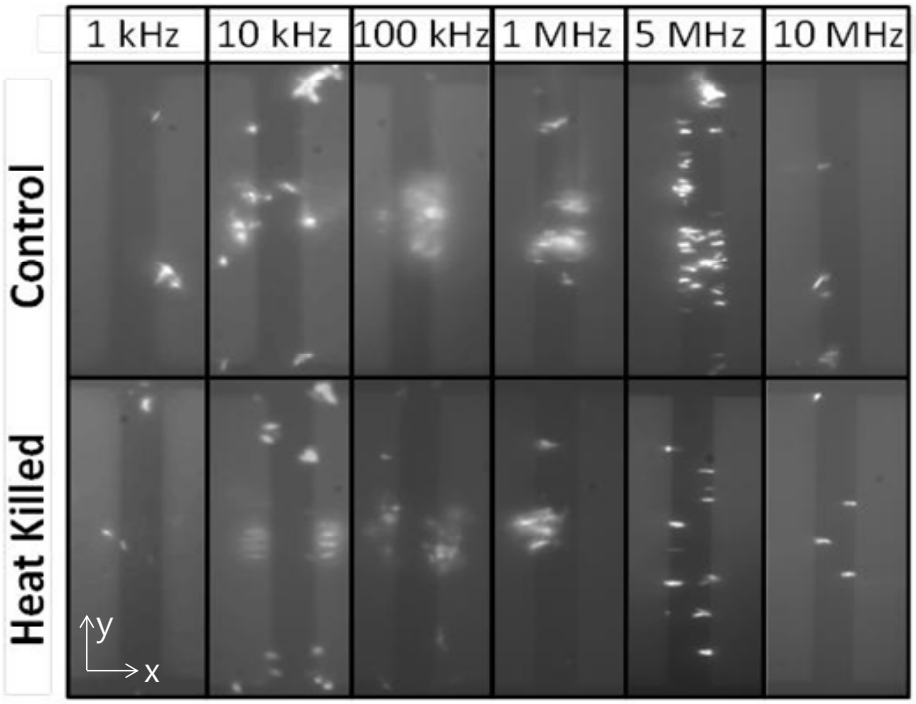

Figure 25 Control- and heat-killed BCG cells attracted to the planar electrodes after 1 minute at frequencies of 1 kHz ~ 10 MHz. Experiment was done by *S. Inoue*.

To study the electrokinetic motion of cells, time-dependent analysis was conducted near the electrode gap. The cell positions were changed with the increase of time by DEP and ACEO. Figure 26a and 27b shows the cell distribution when the time was 50 seconds (t = 50 s). Negative- (nDEP) and positive DEP (pDEP) cases were considered by varying maximum flow speed (v_{max}) with a same flow pattern. To study the effects of nDEP and pDEP, K_{CM} was set to -0.5 and 0.5, respectively. S_{ACEO} was 0.4, 0.2, and 0 for v_{max} of 200, 100, and 0 μm/s, respectively.

For the nDEP case (Fig. 26A), the cells were rotated above the electrode edge and concentrated to the center of the edge, which were consistent with the experimental results at 1, 10, and 100 kHz. With the decrease of ACEO flow, the cells were dispersed along the electrode edge. Without ACEO flow, cells were not aligned above the edge. For the pDEP case (Fig. 26B), the number of captured cells

at the electrode edge was changed with the flow speed. The cells were repelled from the electrode edge if the flow speed was too high (v_{max} = 200 μm/s). The result corresponded to the experiment result of 1 MHz. In the experiment, due to the high flow speed of 180 μm/s, the fewer cells were captured by pDEP. The capturing efficiency was optimal when v_{max} was 100 μm/s. The results for both v_{max} = 100 μm/s and v_{max} = 0 μm/s agreed with the experimental results of 5 MHz and 10 MHz, respectively.

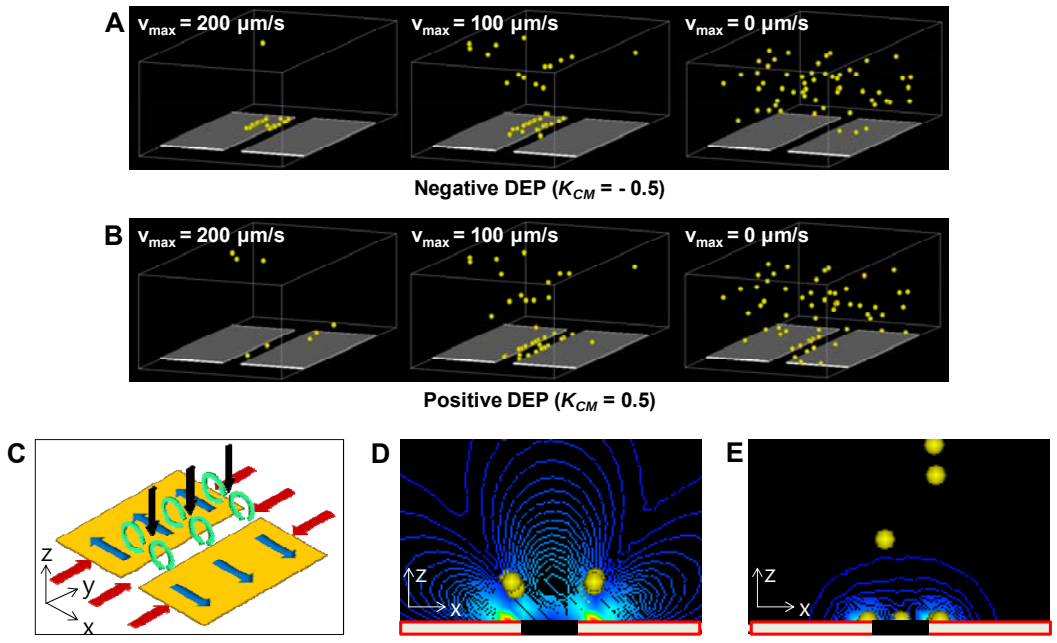

Figure 26 A, B: Time-dependent simulation result of cell movement by DEP and ACEO. Cell distribution at t = 50 s is shown for the cases of nDEP (A) and pDEP (B) with varying flow speed. C: Illustration of flow pattern by ACEO. D, E: Contour plot of flow field and DEP field in x-z plane. The cell distributions of v_{max} = 100 μm/s in Fig. 26a and 26b are overlapped to the contour plot for the case of nDEP (D) and pDEP (E), respectively.

To understand the interaction of DEP and ACEO for electrokinetic behavior of BCG cells, the flow pattern and the force field of DEP and ACEO were investigated (Fig. 26C-E). Figure 26C shows the flow directions by ACEO for the

planar electrodes. In the figure, there are inward- and outward flows toward the electrode gap. The flows along *y*- (red) and *z*-axes (black) are the inward flows that transport cells to the electrode gap. The *x*-directional flow (blue) is outward flow that removes cells from the electrode gap. Also, vortex flows (green) are generated above the two electrode edges in the gap.

The force field of ACEO in *x*-*z* plane is shown in Fig. 26D. The cell distribution of the nDEP case at v_{max} = 100 μm/s of Fig. 26A is plotted together in the figure. The cells were aligned above the electrode edges where the magnitude of force field is the lowest. The alignment position was matched with the center of vortex flow. The flow speed was the highest at the electrode edges. Figure 26E shows the DEP field with the particle distribution of pDEP case of v_{max} = 100 μm/s of Fig. 26B. The particles were captured at the electrode edge of the highest DEP field region.

The equilibrium position of cells for pDEP- and nDEP cases can be explained from the cell transport by ACEO. Initially, cells are transported to the electrode gap by the inward flows. Then, the cells are attracted to or repelled from the electrode edges in the gap depending on the polarity of DEP. For nDEP case, the cells are repelled with the outward flow on the electrode surface. The cells are trapped in the vortex flow instead of flowing out by the outward flow. Therefore, the levitation of cells could be generated for nDEP. For pDEP cases, the cells are attracted to the electrode edges where DEP force is the highest. The capturing is determined by the force difference between DEP and ACEO because both forces of DEP and ACEO are the highest at the electrode edges. When DEP is stronger than ACEO, the cells are captured or removed from the electrode edges.

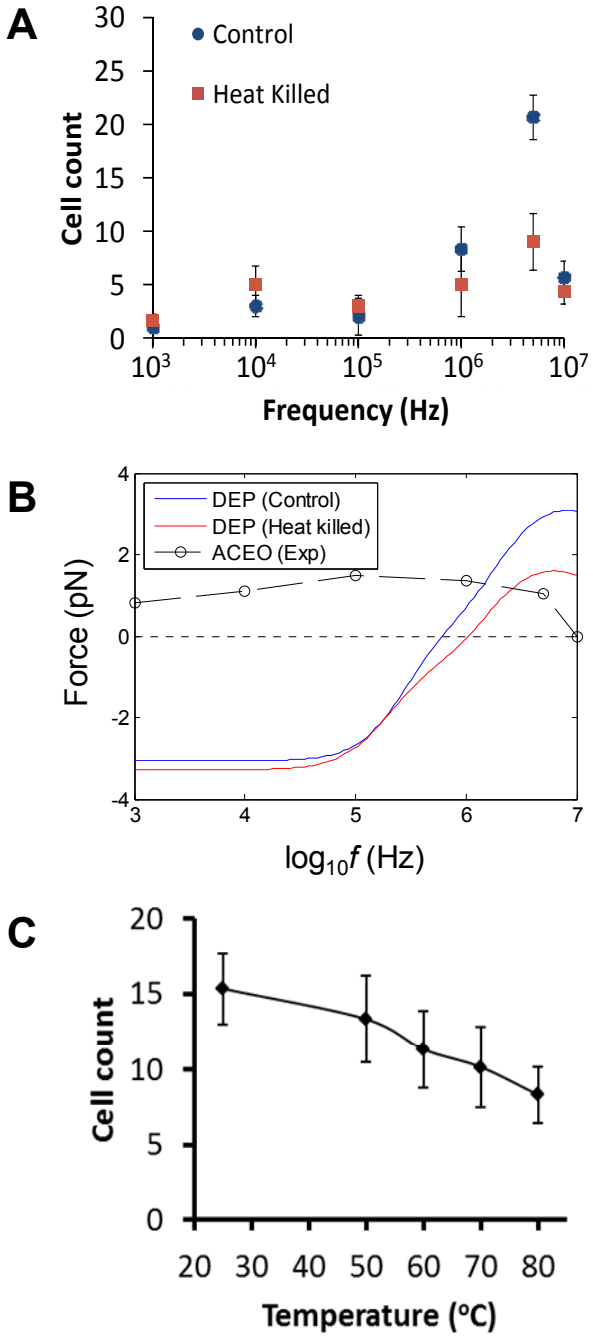

Figure 27 A: Cell count of control- and heat-killed BCG cells under the frequency ranging from 1 kHz to 10 MHz. B: Frequency dependency of DEP forces and drag forces. C: Cell count of BCG cells at 5 MHz after heat treatment at 50, 60, 70 and 80 °C for 10 minutes.

To find an optimal frequency to separate viable- and nonviable BCG cells, the number of captured cells was measured for control- and heat-killed cells by varying the frequency from 1 kHz to 10 MHz. When the cells were counted, the cell clump (or colony) was regarded as one cell. In Fig. 27A, the counting result is compared for the cases of control and heat-killing. At 5 MHz, the cell counting showed the highest difference between control- and heat-killed cells.

To explain the optimal electrokinetic separation of control- and heat-killed BCG cells at 5 MHz, the effect of DEP and ACEO was quantified in terms of force. Fig. 27B shows the forces by DEP and ACEO with respect to frequencies. DEP force was obtained from the K_{CM} spectrum by using cell parameters estimated from the cell counting measurement. The figure shows why 5 MHz is better than 1 or 10 MHz in the contexts of cell capture. At 1 MHz, the ACEO force was higher than the DEP force, which resulted in the removal of cells from the electrode edges. The ACEO force at 10 MHz was significantly lower than that at 5 MHz so the amount of cells transported to the electrode edge was significantly reduced. Therefore the optimal separation was obtained at 5 MHz where ACEO was present and DEP force of control cells was higher than that of heat-killed cells.

The BCG cell's viability upon heat-treatment was investigated at the optimal frequency of 5 MHz in terms of a cell counting number. Figure 27C shows the cell counting result by varying the temperature for the heat treatment. When temperature for treating the BCG cells increased from 25ºC to 80ºC, the number of the attracted cells was reduced as the temperature increased. Over 60ºC, the number of the attracted cells was greatly reduced. The temperature results correlated with the previous assumption of a phase-shift of the cell wall at 60ºC

[116]. Prior to the phase-shift temperature, the *Mycobacterium* cell wall and membrane remained intact and retained its low conductivity. Once the temperature became higher than the phase-shift temperature of 60ºC, the permeability of the cell wall could increase and the leak of ions in the cytoplasm could be induced as well.

The estimated cell parameters of control- and heat-killed BCG cells are summarized in Table 6. The cell parameters of $C_{envelope}$ and σ_{cyto} were extracted from the DEP force spectra in Fig. 27B. Due to heat-killing of BCG cells, the decreases of $C_{envelope}$ and σ_{cyto} were estimated. The decrease of the two parameters was consistent with the mechanism of heat-treatment, which affected the permeability of the cell wall and induced the decrease of ion concentration in the cytoplasm. The change in cell wall permeability was also confirmed through the *I-V* measurement of BCG cells. The value of $G_{envelope}$ in Table 6 was estimated by modeling the *I-V* measurement.

Table 6 Estimated cell parameters of control- and heat-killed BCG cells.

Treatment	$G_{envelope}$ (kS/m^2)	$C_{envelope}$ (mF/m^2)	σ_{cyto} (S/m)
Control	0.43	6.38	0.50
Heat-killed	0.09	5.90	0.25

5.6 Summary

The electrokinetic behavior of *Mycobacterium bovis* BCG was analyzed through numerical analysis and experiment. The cell motion under dielectrophoresis and AC electroosmosis was investigated. The cases of negative and positive DEP were clearly distinguished by analyzing the mechanism for cell capture, trapping and levitation. For the case of nDEP, the cells were trapped in the vortex center where the flow field has low amplitude. Cells were not trapped without ACEO flow. Also, the optimal frequency of 5 MHz for separation of viable- and nonviable BCG cells was suggested by comparing DEP- and ACEO-induced forces. At 5MHz, the change in the cell viability due to heat-treatment was measured in terms of the captured cell number. Finally, the properties of control- and heat-killed BCG cells were estimated. The estimated changes of $C_{envelope}$ and σ_{cyto} were matched with the mechanism of heat-killing, which increased the permeability of cell wall followed by the change of the composition in cytoplasm.

Chapter 6: Summary and Future Study

The sampling-based approach was developed to study the dielectrophoretic behavior of a cell for antimicrobial susceptibility test.

In chapter 2, the sampling-based algorithm for extraction of cell properties from DEP experimental data of σ_m-f_{xo} was proposed for reliable approximation. By comparing the property estimation with that of the low frequency approximation and the 5-level approximation, the sampling-based method was successfully validated. Using the sampling process, various combinations of cell properties were efficiently considered, which resulted in reliable estimation of cell properties without the limited condition caused by any assumptions in property ranges.

In chapter 3, the cell polarization under AC electric field was characterized through a sensitivity analysis using the Latin hypercube sampling. From the study in chapter 2, it was found that σ_m-f_{xo} data cannot represent a single cell having specific combination of cell properties. To understand the relation between cell property and σ_m-f_{xo} data, a global sensitivity analysis was conducted. In the analysis, Latin hypercube sampling method was employed to reduce a computational cost for multi-dimensional analysis. The specific σ_m-f region having a high sensitivity to a specific cell property was identified. As a result, 4-transition conditions for effective estimation of cell properties were proposed.

In chapter 4, dielectrophoretic behavior of *Mycobacterium bovis* bacillus Calmette-Guérin (BCG) cells was studied in response to heat-killing and drug treatment of rifampin (RIF) and isoniazid (INH). The experimental parameters were designed on the basis of the sensitivity analysis. The medium conductivity (σ_m) and the frequency (f) for a crossover frequency (f_{xo1}) test were chosen to detect

the change of σ_m-f_{xo1} in conjunction with the drug mechanism. Statistical modeling was conducted to estimate the distribution of viable- and nonviable cells from the discrete measurement of f_{xo1}. Finally, the parameters of the electrophysiology of BCG cells, $C_{envelope}$ and σ_{cyto}, were extracted through the sampling algorithm. The estimated change of the electrophysiological parameters due to heat- and drug treatment was supported by the SEM images of BCG cells.

Finally, the electrokinetic separation of viable- and nonviable *Mycobacterium bovis* BCG cells was studied. To model a nonviable cell, heat-treatment was used. Dielectrophoresis (DEP) and AC electroosmosis (ACEO) were considered to analyze the electrokinetic behavior of cell. The mechanisms of trapping and capturing of cells were investigated through a numerical analysis and an experimental observation. The optimal frequency of 5 MHz for separation of viable- and nonviable BCG cells was suggested by quantifying the DEP- and ACEO forces. At the optimal frequency, the change in the viability of BCG cell due to heat-treatment was measured in terms of cell counting number. Finally, the parameters of control- and heat-killed BCG cells were estimated. The estimated changes of cell parameters were discussed in connection with the mechanism of heat-killing.

Due to the complex nature of cell polarization, cell characterization using DEP has been limited. In addition, the conventional approaches using the assumptions could derive a deviated approximation of cell property. The sampling-based approach is expected to improve the DEP characterization of a cell. By further developing the approach, DEP approach can be implemented in drug discovery as well as drug-susceptibility test.

Future research will focus on the investigation of a total DEP analysis of AST for application to real samples. To do this, DEP concentration and functionalization will be studied for the purification of real sample containing various non-target particles. Then, the captured target bacteria can be characterized by using sampling-based approach. To this end, the proposed approach will offer a framework for DEP-based AST analysis of bacterial cells.

References

[1] C. report, "Antibiotic Resistance Threats in the United States," Centers for Disease Control and Prevention2013.

[2] J. H. Jorgensen and M. J. Ferraro, "Antimicrobial Susceptibility Testing: A Review of General Principles and Contemporary Practices," *Clinical Infectious Diseases,* vol. 49, pp. 1749-1755, Dec 1 2009.

[3] "Performance standards for antimicrobial disk susceptibility tests; Approved standard," Clinical and Laboratory Standards Institute2009.

[4] W. P. Report, "Towards universal access to diagnosis and treatment of multidrug-resistant and extensively drug-resistant tuberculosis by 2015," World Health Organization2011.

[5] S. H. Gillespie, "Evolution of drug resistance in Mycobacterium tuberculosis: Clinical and molecular perspective," *Antimicrobial Agents and Chemotherapy,* vol. 46, pp. 267-274, Feb 2002.

[6] D. A. J. Moore and N. S. Shah, "Alternative Methods of Diagnosing Drug Resistance-What Can They Do for Me?," *Journal of Infectious Diseases,* vol. 204, pp. S1110-S1119, Nov 15 2011.

[7] H. A. Pohl, "The Motion and Precipitation of Suspensoids in Divergent Electric Fields," *Journal of Applied Physics,* vol. 22, pp. 869-871, 1951.

[8] P. A. Smith, C. D. Nordquist, T. N. Jackson, T. S. Mayer, B. R. Martin, J. Mbindyo*, et al.*, "Electric-field assisted assembly and alignment of metallic nanowires," *Applied Physics Letters,* vol. 77, pp. 1399-1401, Aug 28 2000.

[9] D. A. Brown, J. H. Kim, H. B. Lee, G. Fotouhi, K. H. Lee, W. K. Liu*, et al.*, "Electric Field Guided Assembly of One-Dimensional Nanostructures for High Performance Sensors," *Sensors,* vol. 12, pp. 5725-5751, May 2012.

[10] E. M. Freer, O. Grachev, X. F. Duan, S. Martin, and D. P. Stumbo, "High-yield self-limiting single-nanowire assembly with dielectrophoresis," *Nature Nanotechnology,* vol. 5, pp. 525-530, Jul 2010.

[11] J. Suehiro, G. B. Zhou, and M. Hara, "Fabrication of a carbon nanotube-based gas sensor using dielectrophoresis and its application for ammonia detection by impedance spectroscopy," *Journal of Physics D-Applied Physics,* vol. 36, pp. L109-L114, Nov 7 2003.

[12] N. G. Green and H. Morgan, "Separation of submicrometre particles using a combination of dielectrophoretic and electrohydrodynamic forces," *Journal of Physics D-Applied Physics,* vol. 31, pp. L25-L30, Apr 7 1998.

[13] R. Krupke, S. Linden, M. Rapp, and F. Hennrich, "Thin films of metallic carbon nanotubes prepared by dielectrophoresis," *Advanced Materials,* vol. 18, pp. 1468-+, Jun 6 2006.

[14] J. J. Boote and S. D. Evans, "Dielectrophoretic manipulation and electrical characterization of gold nanowires," *Nanotechnology,* vol. 16, pp. 1500-1505, Sep 2005.

[15] O. D. Velev and K. H. Bhatt, "On-chip micromanipulation and assembly of colloidal particles by electric fields," *Soft Matter,* vol. 2, pp. 738-750, 2006.

[16] R. Pethig, "Review Article-Dielectrophoresis: Status of the theory, technology, and applications," *Biomicrofluidics,* vol. 4, Jun 2010.

[17] K. Khoshmanesh, S. Nahavandi, S. Baratchi, A. Mitchell, and K. Kalantar-zadeh, "Dielectrophoretic platforms for bio-microfluidic systems," *Biosensors & Bioelectronics,* vol. 26, pp. 1800-1814, Jan 15 2011.

[18] P. R. C. Gascoyne and J. V. Vykoukal, "Dielectrophoresis-based sample handling in general-purpose programmable diagnostic instruments," *Proc IEEE Inst Electr Electron Eng.,* vol. 92, pp. 22-42, Jan 2004.

[19] P. Yager, T. Edwards, E. Fu, K. Helton, K. Nelson, M. R. Tam*, et al.*, "Microfluidic diagnostic technologies for global public health," *Nature,* vol. 442, pp. 412-418, Jul 27 2006.

[20] L. J. Yang, P. P. Banada, M. R. Chatni, K. S. Lim, A. K. Bhunia, M. Ladisch*, et al.*, "A multifunctional micro-fluidic system for dielectrophoretic concentration coupled with immuno-capture of low numbers of Listeria monocytogenes," *Lab on a Chip,* vol. 6, pp. 896-905, 2006.

[21] J. H. Kim, W. H. Yeo, Z. Q. Shu, S. D. Soelberg, S. Inoue, D. Kalyanasundaram*, et al.*, "Immunosensor towards low-cost, rapid diagnosis of tuberculosis," *Lab on a Chip,* vol. 12, pp. 1437-1440, 2012.

[22] C. C. Chung, I. F. Cheng, H. M. Chen, H. C. Kan, W. H. Yang, and H. C. Chang, "Screening of Antibiotic Susceptibility to beta-Lactam-Induced Elongation of Gram-Negative Bacteria Based on Dielectrophoresis," *Analytical Chemistry,* vol. 84, pp. 3347-3354, Apr 3 2012.

[23] H. M. Coley, F. H. Labeed, H. Thomas, and M. P. Hughes, "Biophysical characterization of MDR breast cancer cell lines reveals the cytoplasm is critical in determining drug sensitivity," *Biochimica Et Biophysica Acta-General Subjects,* vol. 1770, pp. 601-608, Apr 2007.

[24] F. H. Labeed, H. M. Coley, and M. P. Hughes, "Differences in the biophysical properties of membrane and cytoplasm of apoptotic cells revealed using dielectrophoresis," *Biochimica Et Biophysica Acta-General Subjects,* vol. 1760, pp. 922-929, Jun 2006.

[25] F. H. Labeed, H. M. Coley, H. Thomas, and M. P. Hughes, "Assessment of multidrug resistance reversal using dielectrophoresis and flow cytometry," *Biophysical Journal,* vol. 85, pp. 2028-2034, Sep 2003.

[26] K. Ratanachoo, P. R. C. Gascoyne, and M. Ruchirawat, "Detection of cellular responses to toxicants by dielectrophoresis," *Biochimica Et Biophysica Acta-Biomembranes,* vol. 1564, pp. 449-458, Aug 31 2002.

[27] H. Shafiee, M. B. Sano, E. A. Henslee, J. L. Caldwell, and R. V. Davalos, "Selective isolation of live/dead cells using contactless dielectrophoresis (cDEP)," *Lab on a Chip,* vol. 10, pp. 438-445, 2010.

[28] Y. Huang, X. B. Wang, F. F. Becker, and P. R. C. Gascoyne, "Membrane changes associated with the temperature-sensitive P85(gag-mos)-dependent transformation of rat kidney cells as determined by dielectrophoresis and electrorotation," *Biochimica Et Biophysica Acta-Biomembranes,* vol. 1282, pp. 76-84, Jun 13 1996.

[29] P. Gascoyne, C. Mahidol, M. Ruchirawat, J. Satayavivad, P. Watcharasit, and F. F. Becker, "Microsample preparation by dielectrophoresis: isolation of malaria," *Lab on a Chip,* vol. 2, pp. 70-75, 2002.

[30] Z. Gagnon, J. Mazur, and H. C. Chang, "Integrated AC electrokinetic cell separation in a closed-loop device," *Lab on a Chip,* vol. 10, pp. 718-726, 2010.

[31] M. P. Hughes, *Nanoelectromechanics in engineering and biology*. Boca Raton: CRC Press, 2003.

[32] S. Park, Y. Zhang, T. H. Wang, and S. Yang, "Continuous dielectrophoretic bacterial separation and concentration from physiological media of high conductivity," *Lab on a Chip,* vol. 11, pp. 2893-2900, 2011.

[33] F. Gielen, A. J. Demello, and J. B. Edel, "Dielectric Cell Response in Highly Conductive Buffers," *Analytical Chemistry,* vol. 84, pp. 1849-1853, Feb 21 2012.

[34] M. Castellarnau, A. Errachid, C. Madrid, A. Juarez, and J. Samitier, "Dielectrophoresis as a tool to characterize and differentiate isogenic mutants of Escherichia coli," *Biophysical Journal,* vol. 91, pp. 3937-3945, Nov 2006.

[35] T. B. Jones, *Electromechanics of particles*. Cambridge ; New York: Cambridge University Press, 1995.

[36] Y. Huang, S. Joo, M. Duhon, M. Heller, B. Wallace, and X. Xu, "Dielectrophoretic cell separation and gene expression profiling on microelectronic chip arrays," *Analytical Chemistry,* vol. 74, pp. 3362-3371, Jul 15 2002.

[37] H. O. Fatoyinbo, K. F. Hoeftges, and M. P. Hughes, "Rapid-on-chip determination of dielectric properties of biological cells using imaging techniques in a dielectrophoresis dot microsystem," *Electrophoresis,* vol. 29, pp. 3-10, Jan 2008.

[38] A. Valero, T. Braschler, and P. Renaud, "A unified approach to dielectric single cell analysis: Impedance and dielectrophoretic force spectroscopy," *Lab on a Chip,* vol. 10, pp. 2216-2225, 2010.

[39] J. S. Sun, Y. D. Gao, R. J. Isaacs, K. C. Boelte, P. C. Lin, E. M. Boczko*, et al.*, "Simultaneous On-Chip DC Dielectrophoretic Cell Separation and Quantitative Separation Performance Characterization," *Analytical Chemistry,* vol. 84, pp. 2017-2024, Feb 21 2012.

[40] J. Kadaksham, P. Singh, and N. Aubry, "Dielectrophoresis induced clustering regimes of viable yeast cells," *Electrophoresis,* vol. 26, pp. 3738-3744, Oct 2005.

[41] I. Doh and Y. H. Cho, "A continuous cell separation chip using hydrodynamic dielectrophoresis (DEP) process," *Sensors and Actuators a-Physical,* vol. 121, pp. 59-65, May 31 2005.

[42] J. Johari, Y. Hubner, J. C. Hull, J. W. Dale, and M. P. Hughes, "Dielectrophoretic assay of bacterial resistance to antibiotics," *Physics in Medicine and Biology,* vol. 48, pp. N193-N198, Jul 21 2003.

[43] N. G. Green, A. Ramos, A. Gonzalez, H. Morgan, and A. Castellanos, "Fluid flow induced by nonuniform ac electric fields in electrolytes on microelectrodes. III. Observation of streamlines and numerical simulation," *Physical Review E,* vol. 66, Aug 2002.

[44] J. Wu, Y. X. Ben, D. Battigelli, and H. C. Chang, "Long-range AC electroosmotic trapping and detection of bioparticles," *Industrial & Engineering Chemistry Research,* vol. 44, pp. 2815-2822, Apr 13 2005.

[45] Z. R. Gagnon and H. C. Chang, "Electrothermal ac electro-osmosis," *Applied Physics Letters,* vol. 94, Jan 12 2009.

[46] W. Y. Ng, S. Goh, Y. C. Lam, C. Yang, and I. Rodriguez, "DC-biased AC-electroosmotic and AC-electrothermal flow mixing in microchannels," *Lab on a Chip,* vol. 9, pp. 802-809, 2009.

[47] S. Park and A. Beskok, "Alternating current electrokinetic motion of colloidal particles on interdigitated microelectrodes," *Analytical Chemistry,* vol. 80, pp. 2832-2841, Apr 15 2008.

[48] A. Castellanos, A. Ramos, A. Gonzalez, N. G. Green, and H. Morgan, "Electrohydrodynamics and dielectrophoresis in microsystems: scaling laws," *Journal of Physics D-Applied Physics,* vol. 36, pp. 2584-2597, Oct 21 2003.

[49] J. Gao, M. L. Y. Sin, T. T. Liu, V. Gau, J. C. Liao, and P. K. Wong, "Hybrid electrokinetic manipulation in high-conductivity media," *Lab on a Chip,* vol. 11, pp. 1770-1775, 2011.

[50] B. R. Burg, V. Bianco, J. Schneider, and D. Poulikakos, "Electrokinetic framework of dielectrophoretic deposition devices," *Journal of Applied Physics,* vol. 107, Jun 15 2010.

[51] P. Bahukudumbi, W. N. Everett, A. Beskok, M. A. Bevan, G. H. Huff, D. Lagoudas*, et al.*, "Colloidal microstructures, transport, and impedance properties within interfacial microelectrodes," *Applied Physics Letters,* vol. 90, May 28 2007.

[52] Z. R. Gagnon, "Cellular dielectrophoresis: Applications to the characterization, manipulation, separation and patterning of cells," *Electrophoresis,* vol. 32, pp. 2466-2487, Sep 2011.

[53] K. Asami, "Characterization of biological cells by dielectric spectroscopy," *Journal of Non-Crystalline Solids,* vol. 305, pp. 268-277, Jul 1 2002.

[54] L. M. Broche, N. Bhadal, M. P. Lewis, S. Porter, M. P. Hughes, and F. H. Labeed, "Early detection of oral cancer - Is dielectrophoresis the answer?," *Oral Oncology,* vol. 43, pp. 199-203, Feb 2007.

[55] V. Gupta, I. Jafferji, M. Garza, V. O. Melnikova, D. K. Hasegawa, R. Pethig*, et al.*, "ApoStream (TM), a new dielectrophoretic device for antibody independent isolation and recovery of viable cancer cells from blood," *Biomicrofluidics,* vol. 6, Jun 2012.

[56] S. Shim, K. Stemke-Hale, J. Noshari, F. F. Becker, and P. R. C. Gascoyne, "Dielectrophoresis has broad applicability to marker-free isolation of tumor cells from blood by microfluidic systems," *Biomicrofluidics,* vol. 7, Jan 2013.

[57] R. Pethig, L. M. Jakubek, R. H. Sanger, E. Heart, E. D. Corson, and P. J. Smith, "Electrokinetic measurements of membrane capacitance and conductance for pancreatic beta-cells," *IEE Proc Nanobiotechnol,* vol. 152, pp. 189-93, Dec 2005.

[58] U. Lei, P. H. Sun, and R. Pethig, "Refinement of the theory for extracting cell dielectric properties from dielectrophoresis and electrorotation experiments," *Biomicrofluidics,* vol. 5, pp. 44109-4410916, Dec 2011.

[59] P. R. C. Gascoyne, F. F. Becker, and X. B. Wang, "Numerical-Analysis of the Influence of Experimental Conditions on the Accuracy of Dielectric

Parameters Derived from Electrorotation Measurements," *Bioelectrochemistry and Bioenergetics,* vol. 36, pp. 115-125, Mar 1995.

[60] J. B. Hasted, D. M. Ritson, and C. H. Collie, "Dielectric Properties of Aqueous Ionic Solutions. Parts I and II," *Journal of Chemical Physics,* vol. 16, pp. 1-21, 1948.

[61] B. Alberts, *Molecular biology of the cell*, 4th ed. New York: Garland Science, 2002.

[62] A. Sanchis, A. P. Brown, M. Sancho, G. Martinez, J. L. Sebastian, S. Munoz*, et al.*, "Dielectric characterization of bacterial cells using dielectrophoresis," *Bioelectromagnetics,* vol. 28, pp. 393-401, Jul 2007.

[63] H. Morgan, T. Sun, D. Holmes, S. Gawad, and N. G. Green, "Single cell dielectric spectroscopy," *Journal of Physics D-Applied Physics,* vol. 40, pp. 61-70, Jan 7 2007.

[64] L. Fumagalli, D. Esteban-Ferrer, A. Cuervo, J. L. Carrascosa, and G. Gomila, "Label-free identification of single dielectric nanoparticles and viruses with ultraweak polarization forces," *Nature Materials,* vol. 11, pp. 808-816, Sep 2012.

[65] J. Wyman, "Studies on the dielectric constant of protein solutions I. Zein," *Journal of Biological Chemistry,* vol. 90, pp. 443-476, Feb 1931.

[66] J. R. van der Maarel, "Effect of spatial inhomogeneity in dielectric permittivity on DNA double layer formation," *Biophys J,* vol. 76, pp. 2673-8, May 1999.

[67] P. Kukic, D. Farrell, L. P. McIntosh, E. B. Garcia-Moreno, K. S. Jensen, Z. Toleikis*, et al.*, "Protein dielectric constants determined from NMR chemical shift perturbations," *J Am Chem Soc,* vol. 135, pp. 16968-76, Nov 13 2013.

[68] L. Li, C. Li, Z. Zhang, and E. Alexov, "On the 'Dielectric "Constant" of Proteins: Smooth Dielectric Function for Macromolecular Modeling and Its Implementation in DelPhi," *Journal of Chemical Theory and Computation,* vol. 9, pp. 2126-2136, Apr 2013.

[69] J. C. Helton, J. D. Johnson, C. J. Sallaberry, and C. B. Storlie, "Survey of sampling-based methods for uncertainty and sensitivity analysis," *Reliability Engineering & System Safety,* vol. 91, pp. 1175-1209, Oct-Nov 2006.

[70] A. Saltelli, K. Chan, and E. M. Scott, *Sensitivity analysis*. Chichester ; New York: Wiley, 2000.

[71] W. H. Organization, "Global tuberculosis report 2013," http://www.who.int/tb/publications/global_report/en/2014.

[72] L. B. Heifets and G. A. Cangelosi, "Drug susceptibility testing of Mycobacterium tuberculosis: a neglected problem at the turn of the century," *Int J Tuberc Lung Dis,* vol. 3, pp. 564-81, Jul 1999.

[73] J. Suehiro, R. Hamada, D. Noutomi, M. Shutou, and M. Hara, "Selective detection of viable bacteria using dielectrophoretic impedance measurement method," *Journal of Electrostatics,* vol. 57, pp. 157-168, Feb 2003.

[74] Y. Huang, R. Holzel, R. Pethig, and X. B. Wang, "Differences in the AC electrodynamics of viable and non-viable yeast cells determined through combined dielectrophoresis and electrorotation studies," *Phys Med Biol,* vol. 37, pp. 1499-517, Jul 1992.

[75] G. H. Markx, M. S. Talary, and R. Pethig, "Separation of Viable and Nonviable Yeast Using Dielectrophoresis," *Journal of Biotechnology,* vol. 32, pp. 29-37, Jan 15 1994.

[76] C. C. Chung, I. F. Cheng, W. H. Yang, and H. C. Chang, "Antibiotic susceptibility test based on the dielectrophoretic behavior of elongated Escherichia coli with cephalexin treatment," *Biomicrofluidics,* vol. 5, Jun 2011.

[77] B. G. Hawkins, C. Huang, S. Arasanipalai, and B. J. Kirby, "Automated Dielectrophoretic Characterization of Mycobacterium smegmatis," *Analytical Chemistry,* vol. 83, pp. 3507-3515, May 1 2011.

[78] D. A. Mitchison and A. J. Nunn, "Influence of initial drug resistance on the response to short-course chemotherapy of pulmonary tuberculosis," *Am Rev Respir Dis,* vol. 133, pp. 423-30, Mar 1986.

[79] A. Somoskovi, L. M. Parsons, and M. Salfinger, "The molecular basis of resistance to isoniazid, rifampin, and pyrazinamide in Mycobacterium tuberculosis," *Respir Res,* vol. 2, pp. 164-8, 2001.

[80] A. Telenti, P. Imboden, F. Marchesi, T. Schmidheini, and T. Bodmer, "Direct, automated detection of rifampin-resistant Mycobacterium tuberculosis by polymerase chain reaction and single-strand conformation polymorphism analysis," *Antimicrob Agents Chemother,* vol. 37, pp. 2054-8, Oct 1993.

[81] W. R. McClure and C. L. Cech, "On the mechanism of rifampicin inhibition of RNA synthesis," *J Biol Chem,* vol. 253, pp. 8949-56, Dec 25 1978.

[82] F. Bardou, C. Raynaud, C. Ramos, M. A. Laneelle, and G. Laneelle, "Mechanism of isoniazid uptake in Mycobacterium tuberculosis," *Microbiology,* vol. 144 (Pt 9), pp. 2539-44, Sep 1998.

[83] Y. Zhang, B. Heym, B. Allen, D. Young, and S. Cole, "The Catalase Peroxidase Gene and Isoniazid Resistance of Mycobacterium-Tuberculosis," *Nature,* vol. 358, pp. 591-593, Aug 13 1992.

[84] F. G. Winder and P. B. Collins, "Inhibition by isoniazid of synthesis of mycolic acids in Mycobacterium tuberculosis," *J Gen Microbiol,* vol. 63, pp. 41-8, Sep 1970.

[85] K. Takayama, L. Wang, and H. L. David, "Effect of isoniazid on the in vivo mycolic acid synthesis, cell growth, and viability of Mycobacterium tuberculosis," *Antimicrob Agents Chemother,* vol. 2, pp. 29-35, Jul 1972.

[86] K. Takayama, L. Wang, and R. S. Merkal, "Scanning electron microscopy of the H37Ra strain of Mycobacterium tuberculosis exposed to isoniazid," *Antimicrob Agents Chemother,* vol. 4, pp. 62-5, Jul 1973.

[87] F. Bardou, A. Quemard, M. A. Dupont, C. Horn, G. Marchal, and M. Daffe, "Effects of isoniazid on ultrastructure of Mycobacterium aurum and Mycobacterium tuberculosis and on production of secreted proteins," *Antimicrobial Agents and Chemotherapy,* vol. 40, pp. 2459-2467, Nov 1996.

[88] G. A. Cangelosi and J. S. Meschke, "Dead or alive: molecular assessment of microbial viability," *Appl Environ Microbiol,* vol. 80, pp. 5884-91, Oct 2014.

[89] R. Pethig, A. Menachery, S. Pells, and P. De Sousa, "Dielectrophoresis: A Review of Applications for Stem Cell Research," *Journal of Biomedicine and Biotechnology,* 2010.

[90] C. Hoffmann, A. Leis, M. Niederweis, J. M. Plitzko, and H. Engelhardt, "Disclosure of the mycobacterial outer membrane: Cryo-electron tomography and vitreous sections reveal the lipid bilayer structure," *Proceedings of the National Academy of Sciences of the United States of America,* vol. 105, pp. 3963-3967, Mar 11 2008.

[91] C. Vilcheze, H. R. Morbidoni, T. R. Weisbrod, H. Iwamoto, M. Kuo, J. C. Sacchettini*, et al.*, "Inactivation of the inhA-encoded fatty acid synthase II (FASII) enoyl-acyl carrier protein reductase induces accumulation of the FASI end products and cell lysis of Mycobacterium smegmatis," *Journal of Bacteriology,* vol. 182, pp. 4059-4067, Jul 2000.

[92] W. R. Bowen and F. Jenner, "Theoretical Descriptions of Membrane Filtration of Colloids and Fine Particles - an Assessment and Review," *Advances in Colloid and Interface Science,* vol. 56, pp. 141-200, Mar 29 1995.

[93] I. Safarik and M. Safarikova, "Use of magnetic techniques for the isolation of cells," *Journal of Chromatography B,* vol. 722, pp. 33-53, Feb 5 1999.

[94] L. R. Huang, E. C. Cox, R. H. Austin, and J. C. Sturm, "Continuous particle separation through deterministic lateral displacement," *Science,* vol. 304, pp. 987-990, May 14 2004.

[95] S. S. Kuntaegowdanahalli, A. A. S. Bhagat, G. Kumar, and I. Papautsky, "Inertial microfluidics for continuous particle separation in spiral microchannels," *Lab on a Chip,* vol. 9, pp. 2973-2980, 2009.

[96] J. J. Shi, H. Huang, Z. Stratton, Y. P. Huang, and T. J. Huang, "Continuous particle separation in a microfluidic channel via standing surface acoustic waves (SSAW)," *Lab on a Chip,* vol. 9, pp. 3354-3359, 2009.

[97] D. W. Inglis, "Efficient microfluidic particle separation arrays," *Applied Physics Letters,* vol. 94, Jan 5 2009.

[98] G. M. Whitesides, "The origins and the future of microfluidics," *Nature,* vol. 442, pp. 368-73, Jul 27 2006.

[99] Y. K. Cho, S. Kim, K. Lee, C. Park, J. G. Lee, and C. Ko, "Bacteria concentration using a membrane type insulator-based dielectrophoresis in a plastic chip," *Electrophoresis,* vol. 30, pp. 3153-3159, Sep 2009.

[100] C. M. Das, F. Becker, S. Vernon, J. Noshari, C. Joyce, and P. R. C. Gascoyne, "Dielectrophoretic segregation of different human cell types on microscope slides," *Analytical Chemistry,* vol. 77, pp. 2708-2719, May 1 2005.

[101] J. Yang, Y. Huang, X. B. Wang, F. F. Becker, and P. R. C. Gascoyne, "Differential analysis of human leukocytes by dielectrophoretic field-flow-fractionation," *Biophysical Journal,* vol. 78, pp. 2680-2689, May 2000.

[102] C. F. Chou, J. O. Tegenfeldt, O. Bakajin, S. S. Chan, E. C. Cox, N. Darnton*, et al.*, "Electrodeless dielectrophoresis of single- and double-stranded DNA," *Biophysical Journal,* vol. 83, pp. 2170-2179, Oct 2002.

[103] R. Holzel, "Dielectric and dielectrophoretic properties of DNA," *Iet Nanobiotechnology,* vol. 3, pp. 28-45, Jun 2009.

[104] A. Nakano and A. Ros, "Protein dielectrophoresis: Advances, challenges, and applications," *Electrophoresis,* vol. 34, pp. 1085-1096, Apr 2013.

[105] N. Sasaki, T. Kitamori, and H. B. Kim, "AC electroosmotic micromixer for chemical processing in a microchannel," *Lab on a Chip,* vol. 6, pp. 550-554, 2006.

[106] S. H. Huang, S. K. Wang, H. S. Khoo, and F. G. Tseng, "AC electroosmotic generated in-plane microvortices for stationary or continuous fluid mixing," *Sensors and Actuators B-Chemical,* vol. 125, pp. 326-336, Jul 16 2007.

[107] V. Studer, A. Pepin, Y. Chen, and A. Ajdari, "An integrated AC electrokinetic pump in a microfluidic loop for fast and tunable flow control," *Analyst,* vol. 129, pp. 944-9, Oct 2004.

[108] S. Debesset, C. J. Hayden, C. Dalton, J. C. T. Eijkel, and A. Manz, "An AC electroosmotic micropump for circular chromatographic applications," *Lab on a Chip,* vol. 4, pp. 396-400, 2004.

[109] M. Mpholo, C. G. Smith, and A. B. D. Brown, "Low voltage plug flow pumping using anisotropic electrode arrays," *Sensors and Actuators B-Chemical,* vol. 92, pp. 262-268, Jul 15 2003.

[110] Y. Liu, W. K. Liu, T. Belytschko, N. Patankar, A. C. To, A. Kopacz*, et al.*, "Immersed electrokinetic finite element method," *International Journal for Numerical Methods in Engineering,* vol. 71, pp. 379-405, Jul 23 2007.

[111] M. R. Bown and C. D. Meinhart, "AC electroosmotic flow in a DNA concentrator," *Microfluidics and Nanofluidics,* vol. 2, pp. 513-523, Nov 2006.

[112] W. H. Yeo, H. B. Lee, J. H. Kim, K. H. Lee, and J. H. Chung, "Nanotip analysis for dielectrophoretic concentration of nanosized viral particles," *Nanotechnology,* vol. 24, May 2013.

[113] R. F. Probstein, *Physicochemical hydrodynamics : an introduction*, 2nd ed. New York: Wiley, 1994.

[114] T. B. Jones, *Electromechanics of particles*, Digitally printed 1st pbk. ed. Cambridge ; New York: Cambridge University Press, 2005.

[115] K. Asami, T. Hanai, and N. Koizumi, "Dielectric Analysis of Escherichia-Coli Suspensions in the Light of the Theory of Interfacial Polarization," *Biophysical Journal,* vol. 31, pp. 215-228, 1980.

[116] J. Liu, C. E. Barry, G. S. Besra, and H. Nikaido, "Mycolic acid structure determines the fluidity of the mycobacterial cell wall," *Journal of Biological Chemistry,* vol. 271, pp. 29545-29551, Nov 22 1996.

[117] T. B. Jones, "Basic theory of dielectrophoresis and electrorotation," *Ieee Engineering in Medicine and Biology Magazine,* vol. 22, pp. 33-42, Nov-Dec 2003.

[118] P. R. C. Gascoyne and J. Vykoukal, "Particle separation by dielectrophoresis," *Electrophoresis,* vol. 23, pp. 1973-1983, Jul 2002.

[119] S. Tuukkanen, J. J. Toppari, A. Kuzyk, L. Hirviniemi, V. P. Hytonen, T. Ihalainen*, et al.*, "Carbon nanotubes as electrodes for dielectrophoresis of DNA," *Nano Letters,* vol. 6, pp. 1339-1343, Jul 12 2006.

[120] A. M. Kopacz, W. H. Yeo, J. H. Chung, and W. K. Liu, "Nanoscale sensor analysis using the immersed molecular electrokinetic finite element method," *Nanoscale,* vol. 4, pp. 5189-5194, 2012.

Appendix A: Computation of DEP force

DEP force on a particle is induced by the difference in polarizabilities of a particle and medium under a non-uniform electric field. The polarization of particle is associated with particle characteristics such as shape and electrical properties combined with external parameters including frequency of applied voltage and medium properties [16, 117, 118].

To compute DEP force on a particle, two methods have been proposed, namely the effective dipole moment- (EDM) and the Maxwell stress tensor (MST) theories. The EDM method is used for analytical calculation of a DEP force while the MST method is for numerical computation.

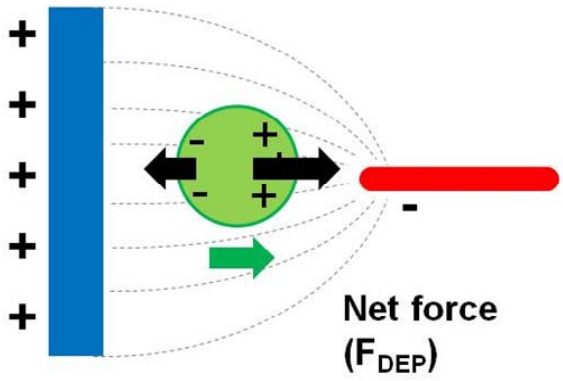

Figure 28 Schematic of DEP on particle. Two electrodes of planar- (blue) and finger (red) shapes are used to generate non-uniform electric field (dashed lines). Due to the difference in electric field on each pole, net force is applied to high e-field direction while a same amount of charges is distributed on each pole on a particle.

A.1 Effective dipole moment (EDM) theory

In the EDM theory, DEP force is generated due to non-uniform electric field, and the induced dipole moment in a particle as shown in Fig. 28. Two

coulomb forces in opposite direction are applied in two poles, and the net force is generated due to the difference on electric field strengths between the two poles:

$$\mathbf{F} = q\mathbf{E}(\mathbf{r} + \mathbf{d}) - q\mathbf{E}(\mathbf{r}) \tag{A.1}$$

where **r** is the position vector to the pole of negatively charge ($-q$), **E**(**r**) indicates the electric field on the pole at the position (**r**), and |**d**| is the distance between the two poles. Eq. (A.1) is reduced to the following form by neglecting the higher order terms with Taylor series expansion under the assumption that the magnitude of **d** is much smaller than the characteristic length of an electric field:

$$\mathbf{F} = \mathbf{p} \cdot \nabla \mathbf{E}(\mathbf{r}) \tag{A.2}$$

Dipole moment (**p**) is defined as:

$$\mathbf{p} = q\mathbf{d} \tag{A.3}$$

Under an alternating current (AC) field, it can be computed by:

$$\mathbf{p} = (Vol)(\alpha)e^{i\omega t}\mathbf{E} \tag{A.4}$$

where Vol is the particle volume, α is the polarization factor, ω is the angular frequency of an applied voltage, and t is the time. Time averaged DEP force on a particle can be derived by using eqs. (A.2) and (A.4):

$$\langle \mathbf{F}_{DEP} \rangle = \frac{1}{2}(Vol)\,\mathrm{Re}[\alpha]\nabla|\mathbf{E}|^2 \tag{A.5}$$

The magnitude of DEP force can vary with the gradient of an electric field. Also, α can affect the magnitude and direction of the force. α depends on the electrical properties of a particle and medium (conductivity and permittivity), the geometry of particle and the input frequency of an electric field. Due to the geometry and property dependency, DEP can be used for the characterization of a particle and the differentiation of a target particle from non-target particles.

DEP is effective for particles with the length scale from a few nanometers to millimeters due to the proportionality to the gradient of electric field square and particle volume [16, 117, 118]. In a submicrometer scale, thermal energy dominates the particle motion (Brownian motion), while the gravity effect is greater than DEP force with a larger scale [35, 48, 112]. The lower limit of DEP-effective size of a particle is determined by the size of electrodes which is strongly related with a micro/nano fabrication technique [119, 120]. Although DEP has a same proportionality to the particle volume same as the gravity force [35], a DEP effect becomes much less than to gravitational force over a millimeter scale. The reason is resulted from the limitation of the applied voltage in liquid to avoid electrolysis. In other words, the electric field strength in nano- or microscale cannot be achieved in millimeter scale.

A.2 Maxwell stress tensor (MST) theory

Maxwell stress tensor (MST) theory is employed to compute DEP force on a particle. In the MST theory, DEP force is computed by the surface integral of Maxwell stress tensor on particle surface:

$$\left\langle \boldsymbol{\sigma}_{MST} \right\rangle = \frac{1}{4}\varepsilon_m \left(\mathbf{E} \otimes \mathbf{E}^* + \mathbf{E}^* \otimes \mathbf{E} - |\mathbf{E}|^2 \mathbf{I} \right) \tag{A.6}$$

$$\left\langle \mathbf{F}_{DEP} \right\rangle = \oint \left\langle \boldsymbol{\sigma}_{MST} \right\rangle \cdot \mathbf{n} dS \tag{A.7}$$

where $\boldsymbol{\sigma}_{MST}$ is the Maxwell stress tensor, ε_m is the permittivity of medium, $\mathbf{E}^*$ is the complex conjugate of an electric field $\mathbf{E}$, and $\otimes$ is the dyadic product.

A.3 Comparison between EDM and MST

EDM is applicable when the particle size is small in comparison to the characteristic length of an electric field. For example, a radius should be 10 times smaller than the gap size between electrodes in order to apply EDM. The reason is because EDM assumes the formation of dipole in the particle while MST can consider the case of multi-pole formation. When the particle size is comparable to the size of the electrode gap, the multiple poles can be induced in the particle, which increases the inaccuracy in the use of assumption of dipole formation. The characteristics of EDM and MST methods are summarized in Table 7.

In this study, EDM is mainly used because the characteristic length of electrodes is much greater than the cell dimension. The complexity for interpretation of DEP experimental result is significantly reduced by using EDM. In addition, the EDM for DEP calculation enables running of a large number of parametric sets because the computational cost is significantly lower than MST.

Table 7 Comparison between EDM and MST.

Method	**EDM**	**MST**
Electric field	$\nabla \cdot \left(\sigma_m \nabla V\right) = 0, \quad in\ \Omega$ $\mathbf{E} = -\nabla V$	$\nabla \cdot \left(\sigma_m^{*} \nabla V\right) = 0 \quad in\ \Omega_m$ $\nabla \cdot \left(\sigma_s^{*} \nabla V\right) = 0 \quad in\ \Omega_s$ $\mathbf{E} = -\nabla V$
DEP calculation	$\left\langle \mathbf{F}_{DEP} \right\rangle = \frac{1}{2}(Vol)\,\mathrm{Re}[\alpha]\nabla\left\|\mathbf{E}\right\|^2$	$\left\langle \boldsymbol{\sigma}_{MST} \right\rangle = \frac{1}{4}\varepsilon_m \left(\mathbf{E} \otimes \mathbf{E}^{*} + \mathbf{E}^{*} \otimes \mathbf{E} - \left\|\mathbf{E}\right\|^2 \mathbf{I}\right)$ $\left\langle \mathbf{F}_{DEP} \right\rangle = \oint \left\langle \boldsymbol{\sigma}_{MST} \right\rangle \cdot \mathbf{n} dS$
Shape dependency	Spherical, oblate, and prolate geometries	Arbitrary shape

Appendix B: Comparison of sampling method

Random- (RS) and Latin hypercube sampling (LHS) were compared for the use in sensitivity analysis and the estimation algorithm. In the sensitivity analysis, the regression coefficient for the membrane permittivity (b_3) was computed for the sampling number of 100 with RS and LHS, respectively. The computations with both RS and LHS were repeated 10 times and the average and the standard deviations for both samplings were compared. As shown in Figure 29, RS shows higher standard variations compared to LHS. This represents the robustness of LHS for the sensitivity analysis with a small number of samples.

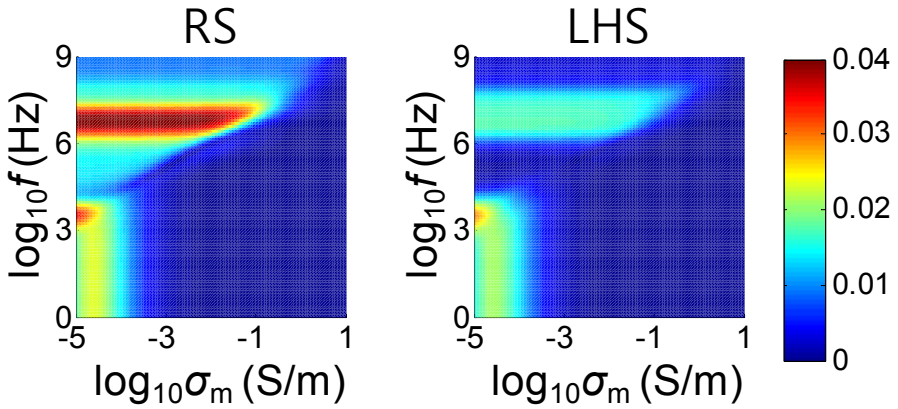

Figure 29 Standard deviations for b_2 from the sensitivity analysis with random- (left) and Latin hypercube (right) sampling. Analysis with the sampling number of 100 was repeated 10 times to compute the standard deviations.

Also, RS and LHS were compared for the use in the estimation algorithm. For the comparison, the two sampling methods were used in the estimation algorithm, respectively. Computation time to find 100 samples which having similar properties with a target cell was compared with the increase of sampling number. Figure 30 shows average computation time with RS and LHS from10 repetitions. RS shows consistency regardless of the sampling number while LHS

shows the increase of computation time with the increase of sampling number. This explains the inefficiency of LHS for the algorithm of the sampling-based estimation which spends most of the computation time in the sampling process.

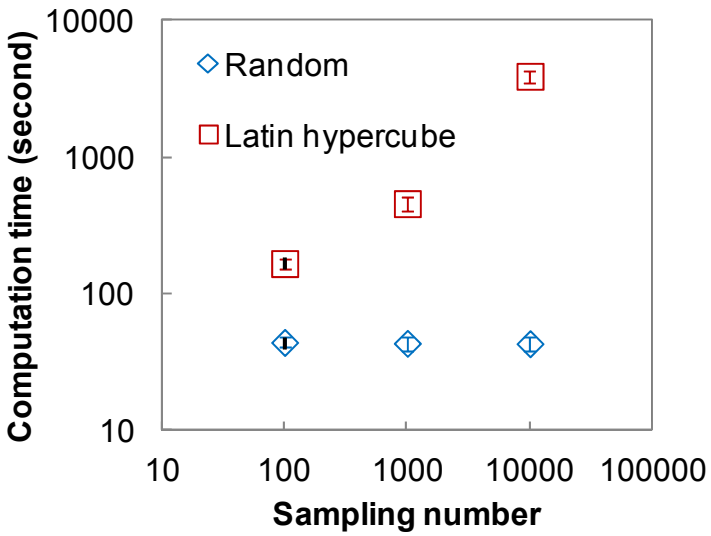

Figure 30 Computation time for sampling-based estimation with the random- and the Latin-hypercube sampling method.